Comparison of two Friction Models

Magnus Gäfvert

June 1996

Abstract

Friction modelling is a delicate problem which poses several challenges to control engineers. This work focuses on two recent models which describe friction with nonlinear dynamical systems: The Lugre model, and the model of Bliman & Sorine.

Comparisons are made concerning friction phenomena captured, computational issues, identification of model parameters and behaviour at zero-crossings of the velocity. Properties are illustrated by simulations. New results on stability and passivity for the Lugre model are presented. Experiments are carried out to validate the models. Limit cycles are investigated by describing function analysis. The impact of a dynamic friction model on friction induced limit cycles is discussed.

Both models give reasonable results in describing function analysis, and it is concluded that dynamic models are superiour to static models when it comes to reproducing limit cycles. The Lugre model exhibits a richer behaviour in terms of friction phenomena. The Bliman & Sorine model could be problematic to use because of poor damping properties. The damping problems for the Bliman & Sorine model turns out to affect overall model behaviour in a complex way.

This work was in part carried out at Laboratoire d'Automatique de Grenoble, CNRS-INPG-UJF, France.

Contents

Acknowledgments

This report is the result of a Masters Thesis project at the Department of Automatic Control, Lund Institute of Technology. A major part of the work was carried out at Laboratoire d'Automatique de Grenoble, CNRS-INPG-UJF. The work has given me a lot of insight into friction modelling, and also very useful experience and contacts concerning international research cooperation.

I want to express my gratitude to those who made it possible for me to do my Masters Thesis project in this interesting and pleasant form. My supervisor Karl Johan Åström, who proposed the subject and arranged with the stay in Grenoble, has with his enthousiasm and vast knowledge in the area been an unvaluable source of inspiration and ideas. Carlos Canudas de Wit, my local supervisor in Grenoble, has with his expertness in the subject and engagement in my work been an outstanding guide through the project. He made my stay with his team at LAG as fruitful and pleasant as could be. I am grateful for the time I was given with the state of the art experimental facilities of the laboratory. I want to thank the Robotics Team, within which I worked, for offering such a friendly and ceative athmosphere. (I owe you a lot of coffee.) Especially I want to thank Pablo Lischinsky for being helpful with suggestions and practical issues concerning my work. Thanks also to those other at LAG that took part in making my stay there so agreeable. Finally I want to thank Henrik Olsson for sharing his ideas and results with me.

This research was supported in part by the Swedish Research Council for Engineering Sciences and the HCM network Nonlinear and Adaptive Control: Towards a Design Methodology for Physical Systems.

1. Introduction

With increasing performance requirements in controlled mechanical systems it becomes more and more important to have good friction models. Well known classical static friction models tend to be replaced by modern dynamical friction models. Two of these modern models are investigated in this work: the model of Bliman & Sorine, and the Lugre model.

In this chapter a short introduction to friction modelling in general is given. Friction terminology used in this report is explained. First the physical mechanisms behind friction are presented. Then some of the phenomena that friction give rise to are described, followed by some of the difficulties introduced by friction for the control engineer, and possible solutions to these. Finally some common simple friction models are presented, and reasons for using more complex models are given.

The second chapter presents the Bliman & Sorine friction model. Formulations of the model are given. Some interesting properties of the model are described. Linearization of the model is carried out. A parameter identification scheme is presented and discussed. Simulations are then carried out followed by a discussion on the model.

The third chapter presents the Lugre model. The formulation of the model is given together with physical interpretations. Linearized equations are given. Some mathematical properties are investigated, such as passivity aspects and stability of a mass system with Lugre friction. Parameter identification is discussed. Simulations are presented, and a discussion on the model follows.

The fourth chapter presents the results of experiments carried out on a DC-servo with friction. Parameter identification is carried out for both models. Some qualitative behaviours of the real system are compared to those of the friction models. Comparisons are done between dry friction and wet friction.

In the fifth chapter friction induced limit cycles are discussed. The ability of the friction models to reproduce limit cycles from the experiments are investigated. Describing functions for the friction models are computed and compared. Finally some ideas on limit cycle prediction are discussed.

In Appendix A some definitions concerning passivity are presented for quick reference, together with a short discussion of physical interpretations of passivity.

Appendix B gives some definitions and theorems on stability for quick reference.

Appendix C describes the experimental setup in detail.

1.1 Friction physics

This section is included to give some background knowledge that might help doing interpretations of the friction phenomena and friction models presented later on in this report. What we usually call friction between bodies in contact is in fact a complex phenomenon composed of several different physical phenomena in combination. The relative influence of these components are depending on contact geometry, the properties of the bulk materials of the bodies, the presence of contaminations (lubrication) on the junction surfaces and also on the properties of the relative motion of the bodies.

Since the purpose of this report is to compare two friction models with respect to their applications in automatic control of mechanical systems, this chapter will focus on friction between metal surfaces with or without presence of a lubricating agent.

Contact topography

[1], [13] The contact topography has to be considered both macroscopically and microscopically. Macroscopically contacts are classified into conformal contacts and nonconformal (Hertzian) contacts as shown in figure 1.1. Conformal contacts are contacts between bodies with matching radiis of curvature. In these

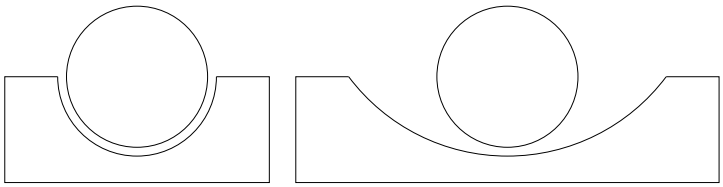

Figure 1.1 The macroscopical topography of contacts. Left: conformal contact. Right: nonconformal contact

contacts the area of the contact surface is determined by the size of the parts, they are therefore also called area contacts. Nonconformal contacts do not fulfill the condition of matching radii of curvature. Therefore they ideally exhibit line- or point contacts. In reality though the parts deform to create an apparent area of contact. The deformation, and therefore also the area of contact, is proportional to the load. Both kind of contacts appear frequently in machines. The stresses found in conformal contacts seldom exceed 7 MPa, whereas in nonconformal contacts the stresses can be 100 times greater.

Further one has to consider that a macroscopically flat surface is far from flat when examined in a microscopic scale. The surface is built up of small asperities, see figure 1.2. The true contact occurs between these asperities, in

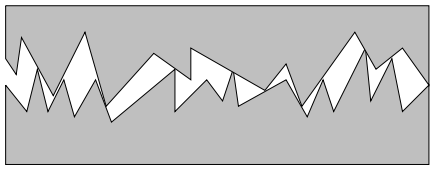

Figure 1.2 Microscopical asperity junctions of an interface between two bodies in contact.

what are called asperity junctions. In engineering materials the slopes of the asperities are typically 5 to 10 degrees, whereas the junction widths typically are $1 \cdot 10^{-5}$ m (in steel). The true area of contact is therefore much smaller than the apparent area of contact and is determined by

$$\text{true area of contact} = \frac{\text{load}}{\text{yield pressure}}$$

where yield pressure is a material property. The asperities deform to generate the contact area necessary to take up the total load. A rule of thumb says that

the contact area, A, is approximately given by

$$A = \frac{W}{3Y},$$

where W is the load, and Y is the yield strength of the material. I.e.contact stress is taken to be three times the yield strength of the material. This is is possible because the asperities are under compression.

Dry friction

[1, 15, 16] Dry friction is friction between two bodies in absence of contaminations of the contact surfaces. This is an ideal situation which is not possible to acheive in a real mechanical system due to the fact that chemical reactions will occur at the surfaces and create oxide films. However, in this ideal case the friction characteristics are expected to be determined entirely by models of solid mechanics. In this context we can define friction as the shear strength of the asperity junction areas. Friction is then proportional to the true area of contact as

$$\text{Friction force} = \text{true area of contact} \cdot \text{shear force per unit area}$$

where the shear force is a material property. As a result friction is proportional to the load, and independent of the surface area. A well known property from basic physics courses. More precisely friction is the force required for the elastic and plastic deformation of the asperities which follows from a relative motion of the bodies in contact. This process is described by the stress-strain characteristics of the materials, se figure 1.3

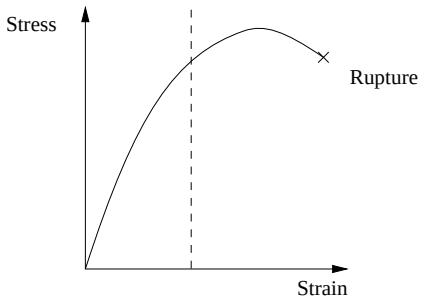

Figure 1.3 Stress–strain characteristics of solid materials. The transition from elastic to plastic region is marked out.

Small applied forces result in elastic reversible "spring like" deformations of the asperities. The tangential force can in this regime be approximated by

$$F_t(\boldsymbol{x}) = -\boldsymbol{k}_t\boldsymbol{x} \tag{1.1}$$

where $\boldsymbol{k}_t$ is the stiffness of the contact and depends on asperity geometry, material elasticity and applied normal force, and $\boldsymbol{x}$ is the relative displacement away from the equilibrium position. Larger forces induce plastic irreversible deformation, and even larger forces cause rupture of the asperities. The stress-strain curve indicates that there is a maximum stress that the material can bear. When an applied force exceeds this stress, the junctions will break and

sliding occur. This force is called the *break-away force*, F_b. To first approximation it is the *break-away displacement*, x_b, that is constant, and the stiffness is then given by

$$k_t = \frac{F_b}{x_b}.$$

The break away displacement in steel junctions is typically 2–5 microns. Small motions before rupture are refered to as pre-sliding displacement. One should note that the stress–strain characteristics of a material are obtained by standardized tests, where the rate of the applicated force is fixed to certain signal forms, often very slow.

When break-away has not yet occured we say that the system is in *stick*. The friction force in stick is called *static friction*, or in short *stiction*. When break-away has occured the system is in *slip*, and the friction is then called *dynamic friction*.

Once sliding has started the friction properties are very much dependent on the properties of the present contaminations, or the lubrication, in the interface. The situation where sliding occurs between two clean surfaces will not be treated here, since it is very unlikely to be found in a mechanical system to be controlled.

Some sources [15] refer to interatomic forces in the junctions causing adhesion between the surfaces as a significant mechanism behind friction in some cases. Friction is then the force necessary to break the adhesion.

In [1] it is argued that static friction is not truly a force of friction since it is neither dissipative, nor a consequence of sliding. Instead the term "tangential force" is suggested. The arguments are questionable, however. It is true that elastic motion is not dissipative, but the plastic deformation of the asperities give rise to power dissipation. Moreover, historically friction has not been defined as a consequence of sliding only. E.g. the idea of a force for going from zero velocity to a small steady state sliding velocity, that is higher than the force required to maintain the sliding velocity is not new, and has always been refered to as a friction phenomenon.

It would be interesting to find articles that physically treats rate dependency of the break-away process.

Lubrication

[16, 1] Presence of lubrication between the surfaces influences the sliding characteristics. The lubrication agent creates thin films on the surfaces. The film thickness increases with velocity according to hydrodynamic lubrication theory, from a sometimes monomolecular layer for zero velocity to a thickness that exceeds the asperity size for high velocities.

It is common to treat four different regimes separately [1]. The regimes are defined by steady state sliding velocity and can be seen in figure 1.4.

The first regime: stiction and pre-sliding displacement This regime corresponds to the dry friction phenomena before break-away described in the previous section. Contact is taking place in asperity junctions with only a very thin film in the junctions. Elastic and plastic deformation of the films are superimposed on the asperity deformations. For sufficiently large displacements rupture of the asperity junctions takes place and the system goes into sliding and the second regime.

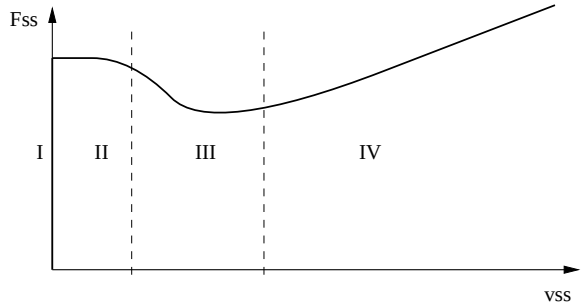

Figure 1.4 The *generalized Stribeck curve* describes the steady state friction, F_{ss} as a function of steady state velocity, v_{ss}, for lubricated surfaces in contact.

The second regime: boundary lubrication For very low velocities no fluid film is present between the surfaces, and the forces acting in the interface is shear forces in the solid boundary films.

The third regime: partial fluid lubrication In this regime lubricant is drawn into the junction interfaces, and due to the viscousity some of the lubricant creates a fluid film between the surfaces. However the film thickness is thinner that the size of the asperities, and therefore some of the load is carried by the lubrication film, and some by elastic and plastic deformation of the asperities. As the velocity increases, the film thickness increases, and the resulting tangential force decreases since the shear forces of the lubrificant film are smaller than the shear forces of the asperities. This is denoted *the Stribeck effect.*

The fourth regime: full fluid lubrication In this regime a lubricant film thickness that is thicker than the size of the asperities is maintained. The friction characteristics are now determined by hydrodynamic (conformal contacts) or elasto-hydrodynamic (non-conformal contacts) theory. In the hydrodynamic case there is only viscous friction. The viscous friction increases with velocity since the shear rates and the shear strenghts of the fluid film are proportional to sliding velocity.

1.2 Friction related phenomena in mechanical systems

Several friction phenomena have been observed long before they have been explained physically. For most applications it is not necessary to know the true mechanism behind a phenomenon, but it is enough to have a good model of the phenomenon. This is the engineering approach to friction.

Pre-sliding displacement

Small motions in the elastic region in stick are refered to as *pre-sliding displacement* or *the Dahl effect.* The region in which the motion is elastic is normally displacements less than 2 micron for steel. The physical process behind this phenomenon is the stress-strain characteristics of the asperity junctions as described earlier.

In all mechanical systems there is a mechanism stiffness present. This stiffness often gives rise to larger displacements than that of the asperity stiffness. It is not possible to separate these phenomena normally.

Wether or not the pre-sliding displacement is due to frictional stiffness or mechanism stiffness this effect is important in high precision control and should be captured by a model.

Stribeck effect

For low velocities the friction decreases with increasing velocity. This is destabilizing in control systems. The physical explanation is given in the section on partial fluid lubrication. See figure 1.4.

Stick-slip motion

Stick-slip motion means motion that alters between stick and slip, and is found in frictional systems with stiffness and integrators, generally spoken. The phenonmenon can be illustrated by drawing a rubber along a table. This is also the effect that induces vibrations in the string of a violin when you play it.

The explanation to this phenomenon is a break-away force that is higher than the sliding force. Starting in stick, the spring force is integrated until the break-away force is reached, when suddenly the friction force drops and the system accelerates by means of the energy stored in the spring. When this energy is consumed by acceleration the system retardates, and goes back to stick. Then the cycle starts all over again.

The explanation is intendedly held very general. The phenomenon can be found in many systems such as in uncontrolled mechanical systems with stiffness and integration (as the rubber on the table above), in velocity control with a P-regulator or in position control with a PI-regulator.

Frictional lag

In [17] experiments were carried out where the velocity were varied periodically in time around a bias in unidirectional motion. The experiments were designed such that all lubrication regimes were covered. It turned out that the friction force was lower for decreasing velocities than for increasing. The difference became larger when the variations were faster. See figure 1.5.

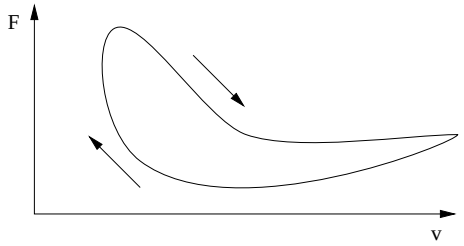

Figure 1.5 Frictional lag, F is friction force and v is velocity.

The phenomenon was explained by a pure time delay, but it is also reproduced by some dynamic friction models.

Varying break-away force

Experimental results earlier gave the idea that the break-away force increase with the time in stick, the so called welding time. Later experiments however

showed that it is not the time in stick that affects the break-away force, but the rate of change of the externally applied force. Larger rates give smaller break-away force, and vice versa.

1.3 The implications of friction on control

The obvious problem that is introduced by friction in control systems is the non-linear dynamics. It is by far more easy to design regulators for linear systems. Small non-linearities can often be neglected, or approximated by linearizations. This is not possible with friction, however, when the working region of the system involves sign changes of velocity or low velocities. For control systems with working regions at high velocities friction can be modeled as a pure damping.

Often the best way to minimize the problem of friction is to simply minimize the actual friction. This can be done by choosing lubricant properly. Often lubricants are chosen to minimize frictional wear rather that to minimize frictional forces. Another way is to introduce vibrations in the system. If there still is significant friction in the system this has to be concidered by the control engineer.

If a linear design is carried out in spite of the presence of friction some unwanted phenomena can occur. If integral action is used limit cycles can occur in position control. One way to avoid this is to use PD-control with the result of steady-state errors. In velocity control even PD-control may give limit cycles. This can be avoided by using high gain. Today it is not well understood exactly when limit cycles occur in these systems, just that they do in some cases. Therefore the control strategy is often choosen as a method that can be proved not to give limit cycles, but that give poorer system performance than other controllers might give. It would be useful to have tools that help determine when limit cycles occur in these systems, so that for example normal gain controllers with integral actions could be used with theoretical support. See [22].

A better way to cope with friction is to introduce it explicitally in the system model. If it is possible to model friction accurately, one can estimate friction from the model and add the friction term to the control signal. How easy this is depends on where the friction enters the system. If friction enters at the same place as the control signal the friction is cancelled and the remaining system can be regarded as linear. If there is dynamics between the control signal and the friction this has to be invertible.

1.4 Friction modeling

This chapter is included to introduce some concepts used in friction modeling in general. The contents is more or less a condensed form of [22, chapter 2].

Static friction models

There is a long tradition in static friction modeling reaching back to the days of Leonardo da Vinci. The terminology used in friction topics is to a great extent inherited from static friction models. A short overview will here be given to introduce the most important terminology. The terminology is not

entirely clear however, in articles the terms are sometimes used with slightly different meaning, and the use of the terms here shall be regarded as the authors conception.

Models based on early ideas are often refered to as *classical friction models.* Static friction models are classicaly introduced as static maps from velocity and externally applied force to friction force.

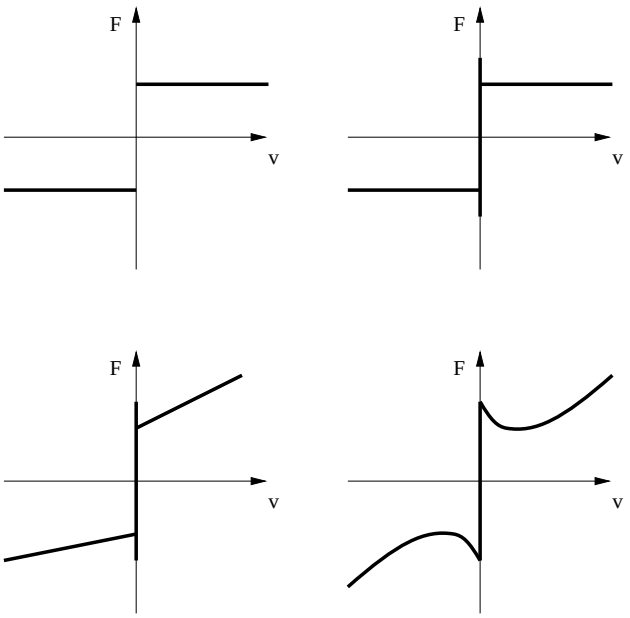

Figure 1.6 Some static friction models. From upper left: Coulomb model, Coulomb + stiction, Coulomb + stiction + viscous friction, Coulomb + stiction + viscous friction + Stribeck effect.

Coulomb friction *Coulomb friction* is the simplest form of static friction, see figure 1.6 and is defined by

$$F = F_C \text{sgn}(v). \tag{1.2}$$

Coulomb friction is also denoted *kinetic friction*, since it defines friction for non-zero velocities. For zero velocities the friction from (1.2) depends upon the definition of the sign function.

Stiction Experimentally it was early discovered that it is needed a higher force to bring a system from zero velocity to a steady-state velocity, than to maintain the steady-state velocity, i.e. the friction force at rest is higher than the kinetic friction. The most obvious modification of the Coulomb model is thus to add a term

$$F = \begin{cases} F_e, \text{ if} v = 0 \text{ and } |F_e| \leq F_s \\ F_s \text{sgn}(F_e), \text{ if } v = 0 \text{ and } |F_e| > F_s. \end{cases} \tag{1.3}$$

We say that the system is in *stick* when we need an externally applied force greater than the stiction force to reach a steady state velocity, otherwise the system is said to be in *slip*.

Viscous friction The friction force in lubricated system has a velocity dependent term originating from hydrodynamic effects. Often this is modeled by the linear relation

$$F = F_v v, \tag{1.4}$$

but generally this term exhibits a non-linear behaviour like

$$F = F_v |v|^{\delta_v} \mathrm{sgn}(v), \tag{1.5}$$

with δ_v being $1/3, 2/3$ or 1 depending on application geometry.

Stribeck effect The Stribeck effect, see section 1.2, can be included in a static friction model by modifying the kinetic friction as showed in figure 1.6.

Problems with static models In simulations or control applications the static models are dependent on detection of zero velocity, since then a switching between different equations is done. There also exist phenomena that cannot be modeled with a static friction model, such as the pre-sliding displacement, varying break-away force and frictional lag.

There exist modern static friction models, e.g. the *Karnopp model*, which is a static map from velocity and externally applied force to friction force, eliminating the use of different equations to model friction for different working points. However the trend moves towards the use of *dynamic friction models* for high precision friction modeling.

Dynamic friction models

The Bliman-Sorine model and the Lugre model, the two friction models investigated in this work, are *dynamic friction models*. I.e. they cannot be described by a static map from system states and inputs to friction force. Instead this relation is described by a (system) of non-linear differential equations. These models will be given one chapter each. Here an early dynamic friction model will be presented, giving somehow the context in which the Bliman & Sorine model and the Lugre model are introduced.

An early dynamic friction model was the *Dahl model* [8]. Dahl started with the relation

$$\frac{dF}{dt} = \frac{\partial F}{\partial t} + \frac{\partial F}{\partial x}\frac{dx}{dt}$$

where F, x denotes friction force and displacement respectively. The displacement is measured from an arbitrary origin. Dahl then made the assumption

$$\frac{dF}{dt} = \frac{dF}{dx}\frac{dx}{dt}. \tag{1.6}$$

The quantity $\frac{dF}{dx}$ is supposed to not depend on t, which implies stationarity. It should not depend explicitly on x, which means the behaviour is invariant by translation. It is positive, yielding a non-linear spring effect. (With $\frac{dF}{dx} = k$ positive and constant the expression can be written as $F = kx$ if integrating both sides, giving a linear spring model.) It is bounded by $-F_C$ and $+F_C$, F_C being the Coulomb friction force, and $|F| \to F_C, \frac{dF}{dx} \to 0$ if $|x| \to \infty$. This means the model behaves as a Coulomb model for large displacements. For small displacements $|F_C| \ll F_C$ and $\frac{dF}{dx} \sim \sigma$, where σ is a spring stiffness. The *general Dahl model* fulfils these requirements and is written

$$\frac{dF}{dx} = \sigma \left| 1 - \frac{F}{F_C}\mathrm{sgn}\frac{dx}{dt} \right|^i \mathrm{sgn}\left(1 - \frac{F}{F_C}\mathrm{sgn}\frac{dx}{dt}\right). \tag{1.7}$$

With $i = 1$ this simplifies to the *simplified Dahl model*

$$\frac{dF}{dx} = \sigma(1 - \frac{F}{F_C}\text{sgn}\frac{dx}{dt}), \tag{1.8}$$

or

$$\frac{dF}{dt} = \sigma(1 - \frac{F}{F_C}\text{sgn}\frac{dx}{dt})\frac{dx}{dt}. \tag{1.9}$$

The Dahl model includes Coulombic friction and pre-sliding displacement. The two models investigated in this report can both be seen as extensions to the Dahl model including more friction phenomena.

2. The model of Bliman and Sorine

Pierre-Alexandre Bliman and Michel Sorine have in a number of articles [5, 6, 7] proposed dry friction models based on a mathematical framework of hysteresis operators. The final model includes stiction force, Dahl pre-displacement, and hysteretic behaviour. This is acheived by a model which can be described as filtering of the Coulomb friction model (1.2) in space domain.

Bliman and Sorine first propose a general class of friction models, and then particularize on the model which is investigated in this work.The main purpose of their work they summarize as follows:

1. To present a model that exhibits rate independent transient behaviour. I.e. the friction force is independent of the velocity $|v(t)|$, but depends only upon the covered distance $\int |v(t)|dt$ when $\mathrm{sgn} v(t)$ remains constant. This according to observed experimental behaviour [15, 12].
2. Since friction dissipates energy the model should be dissipative.
3. It must be easy to perform identification to find model parameters.
4. The friction model together with the equation of motion (including control feedback) must constitute a well posed set of equations.
5. The model shall include the Coulomb friction as a special case.
6. The model must be simple enough in order to be used in real time algorithms.

2.1 Formulation in space variable

The Bliman models have their nicest representations in space formulation, instead of time, why this is the form first presented. Generally for this model, the space formulation is used for mathematical analysis and identification, while the time formulation is used for simulation and design of friction compensation.

After having presented a general class of hysteresis operators Bliman and Sorine present the important subclass of *Linear Space Invariant (LSI)* differential operators. They have the general form $A \in \mathbb{R}^{p\times p}$, $B \in \mathbb{R}^{p\times 1}$, $C \in \mathbb{R}^{1\times p}$, $D \geq 0$

$$\begin{cases} \frac{dx_s}{ds} = Ax_s + Bu_s,\ x_s(0) = x_0 \in \mathbb{R}^p \\ F(u_s) = Cx_s + Du_s \end{cases} \tag{2.1}$$

with s being a space variable. A choice of s is given by the following transformation, proposed in [5], which is fruitful for the analysis of several friction models:

$$ds = |v(t)|dt, \tag{2.2}$$

or in integral form

$$s = \int_0^t |v(\tau)|d\tau. \tag{2.3}$$

The variable s is a space variable which is defined as the *absolute relative displacement* of the bodies in contact since the last change of sign of velocity. This means that each change of sign of velocity generates a new origin in s-space. First a first order friction model is introduced by letting

$$A = -\frac{1}{\varepsilon_f},\ B = \frac{f_1}{\varepsilon_f},\ C = 1 \tag{2.4}$$

and $u_s = \mathrm{sgn}(v)$ in (2.1). The parameter f_1 has dimension force and represents the Coulomb force, and ε_f is a distance related to the pre-sliding displacement. The space invariance of the system implies *rate independency*, i.e. that the output of the system is independent of the rate of change of the velocity input. As a result the friction force generated by (1.8) (or (2.4)) is only dependent on the displacement from the origin and not on the rate with which this displacement is done. The model offers a regularization of the Coulomb model (1.2) since it removes the discontinuity at zero velocity, and it models the Dahl effect described in section 1.2. In fact the model is a first order filter in space that works with step inputs defined by $\mathrm{sgn}(v)$.

By applying (2.2) on the simplified Dahl model (1.8), which then transform to

$$\frac{dF}{ds} = -\sigma\frac{F}{F_C} + \sigma\mathrm{sgn}\frac{dx}{dt}, \tag{2.5}$$

we see that this is identical to (2.4).

A first idea to introduce a higher stiction force would be to introduce a second state in (2.4), yielding

$$A = \begin{bmatrix} 0 & 1 \\ -\frac{1}{\varepsilon^2} & \frac{-2\zeta}{\varepsilon} \end{bmatrix},\ B = \begin{bmatrix} 0 \\ \frac{1}{\varepsilon^2} \end{bmatrix},\ C = \begin{bmatrix} f_C & 0 \end{bmatrix}.$$

A representation that clearer shows what we now have is

$$\varepsilon^2\frac{d^2F}{ds^2} + 2\zeta\varepsilon\frac{dF}{ds} + F = f_C\mathrm{sgn}(v), \tag{2.6}$$

i.e. the stiction force is modeled by the overshoot of the step response in this second order system with a damping $0 \le \zeta \le 1$. We now have a friction model that models Dahl pre-sliding displacement and higher stiction force in a rate-independent way. In [5, 6] (2.1) is the presented version of the model. As noted in the refered articles this model is not dissipative, i.e. it can produce energy during certain conditions, which is an annoying property for any friction model. (The first order model (2.4) is dissipative though.)

Therefore in [7] the following reformulation of the second order model is presented.

$$A = -\frac{1}{\varepsilon_f}\begin{bmatrix} \frac{1}{\eta} & 0 \\ 0 & 1 \end{bmatrix},\ B = \frac{1}{\varepsilon_f}\begin{bmatrix} \frac{f_1}{\eta} \\ -f_2 \end{bmatrix},\ C = \begin{bmatrix} 1 & 1 \end{bmatrix}. \tag{2.7}$$

This is two first order models in parallell, i.e. the complex poles of (2.1) have been replaces by real ones. This is the latest version of the model, and the one that will be regarded in the following. Regard for a moment the Laplace transform of (2.1), (2.7). Then with $Y = \mathcal{L}\{F\}$ and $U = \mathcal{L}\{\mathrm{sgn}(v)\}$ we have

$$Y = C\left(sI - A\right)^{-1}BU = \left(\frac{f_1}{\varepsilon_f\eta s + 1} - \frac{f_2}{\varepsilon_f s + 1}\right)U, \tag{2.8}$$

which clearly shows how the model is built up by two first order models in parallell. The first of these, with a static gain f_1, is faster than the second, with static gain f_2, by a factor η in the corresponding space constants[1]. The parameters f_1 and f_2 have dimension force, ε_f dimension distance, and η is dimensionless. The only immidiate interpretation of the parameters is that of $f_1 - f_2$ which is the Coulomb friction force. Correspondance to physical parameters is given in section 2.8.

The model response becomes that of figure 2.1, where the two first order responses are plot together with their difference.

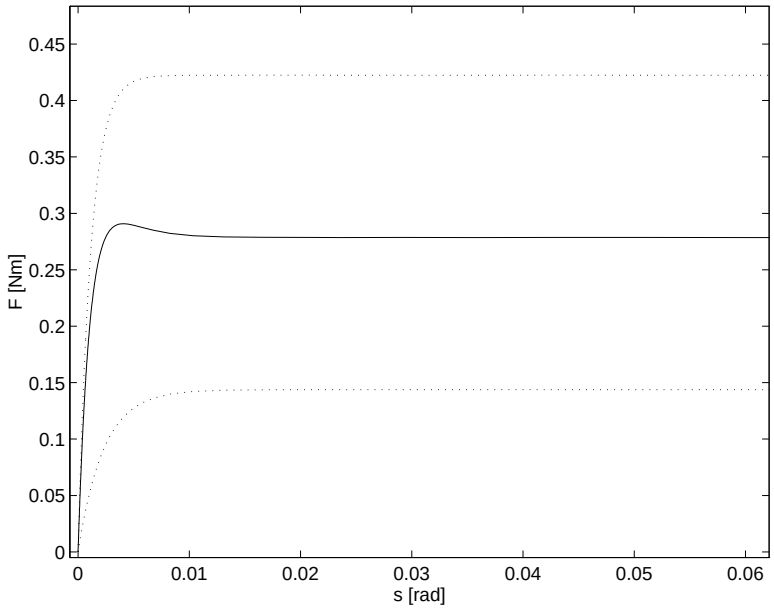

Figure 2.1 Bliman model resonse as friction force versus absolute relative displacement. The two first order model responses are plotted together with their difference.

Rewritings of (2.8) give us

$$Y = \frac{\frac{f_1 - \eta f_2}{\varepsilon_f \eta} s + \frac{f_1 - f_2}{\varepsilon_f^2 \eta}}{s^2 + \frac{\eta + 1}{\varepsilon_f \eta} s + \frac{1}{\varepsilon_f^2 \eta}} U. \tag{2.9}$$

From this we see that the system is of second order with an output zero.

2.2 Rate dependent friction phenomena

The model (2.7) is rate independent. There are however friction phenomena that are rate dependent. The most obvious is the viscous friction. In [5] it is proposed to model all rate dependent phenomena by a memoryless function. For viscous friction this approach is obvious, and the common way to go. Either by the usual linear assumption $F_v = \alpha v$, α being the viscous friction

[1]The notation "space constant" for LSI systems will be used to refer to the equivalence of time constant for LTI systems.

coefficient and v the velocity, or by some more general non-linear function. How to model a phenomenon such as rate-dependent break-away force by a memoryless function is less obvious, since this corresponds to a term that should be subtracted from the stiction and Coulomb friction, while the usual viscous friction is added. This contradiction makes it tempting to include some rate dependent behaviour in the dynamic friction model.

Another issue that not only makes it tempting, but also necessary to include rate dependent dynamics is that of frictional lag. Since the Bliman & Sorine model (2.7) is two simplified Dahl models (1.8) in parallell it inherits properties from this model. The model (2.7) only models displacement dependent transient behaviour after a sign change of velocity. Frictional lag occurs at uni-directional motion and cannot be described as a function of displacement.

2.3 Physical interpretation

The physical process the Bliman & Sorine friction model is aimed to model is the strain-stress characteristics of the junction surface as described in section 1.1. For small displacements, less than the pre-sliding displacement, the junction asperities are deformed elastically, giving a spring-like response to externally applied forces. The model exhibits an elastic behaviour for this region. For larger displacements the junction asperities deform plastically. There is in the transition between these phenomena a region with mixed behaviour. As soon as plastic deformation is part of the process the friction exhibits an hysteresis curve in the displacement versus friction plot.

In the Bliman & Sorine friction model these regions are defined by the parameters s_e, denoting the pre-sliding displacement, f_s denoting the maximum stiction force, occuring at s_e, s_p denoting the displacement after which the behaviour is mainly plastic, and f_k denoting the kinetic friction, reached at s_p. These points are illustrated in figure 2.2. These parameters are not the one that parametrize the model equations. The map translating from these parameters $[\ f_s \quad f_k \quad s_e \quad s_p\ ]$, which we denote *identification parameters*, to the model equation parameters $[\ f_1 \quad f_2 \quad \varepsilon_f \quad \eta \quad \alpha\ ]$, which we denote *model parameters* is given in section 2.8. α is linear viscous friction coefficient.

The maximal stiffness of the elastic behaviour for small displacements, k_F^+, can be expressed in model parameters. Also the extremum of the negative stiffness, k_F^- obtained after break-away can be described in these parameters. The expressions are

$$\begin{cases} k_F^- &= \frac{2f_2}{\varepsilon_f}\left(\frac{\eta^2 f_2}{f_1}\right)^{\frac{\eta}{1-\eta}}(1-\eta) \\ k_F^+ &= \frac{2}{\eta\epsilon_f}(f_1 - \eta f_2) - k_F^-. \end{cases} \tag{2.10}$$

2.4 Formulation in time

While (2.7) is a good way to write the model in term to simplify the mathematical analysis, it is not suited for simulation purposes when acting as a part of a connected system. The system (2.1) transforms to

$$\begin{cases} \dot{\boldsymbol{x}} &= |v|A\boldsymbol{x} + B\boldsymbol{v} \\ \boldsymbol{y} &= C\boldsymbol{x} \end{cases} \tag{2.11}$$

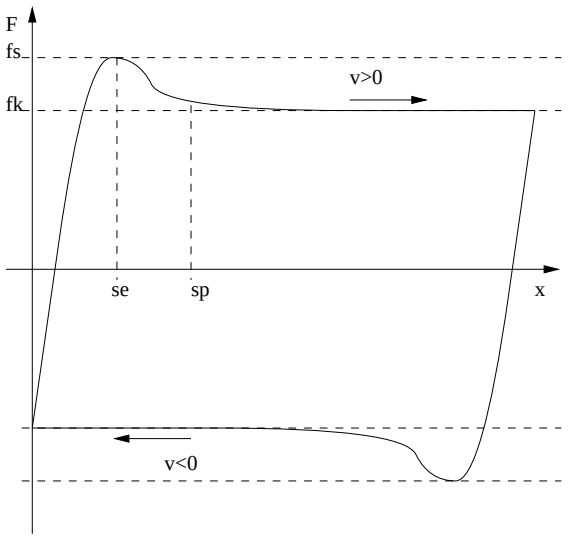

Figure 2.2 The points (s_e, f_s), (s_p, f_k) in the saturated hysteretic cyclic motion are used to determine the parameters in the Bliman & Sorine model.

for s defined by (2.2). The Bliman & Sorine time formulation then simply is (2.7), (2.11). Written out this is

$$\begin{cases} \dot{x_1} &= -|v|\frac{1}{\varepsilon_f \eta}x_1 + \frac{f_1}{\varepsilon_f \eta}v \\ \dot{x_2} &= -|v|\frac{1}{\varepsilon_f}x_2 - \frac{f_2}{\varepsilon_f}v \\ F &= x_1 + x_2 \end{cases} \tag{2.12}$$

The following change of variables gives a form which is good for comparison with the Lugre model later on

$$\begin{cases} z_1 &= \frac{\varepsilon_f \eta}{f_1}x_1 \\ z_2 &= \frac{\varepsilon_f}{f_2}x_2. \end{cases}$$

(2.12) now becomes

$$\begin{cases} \dot{z_1} &= -|v|\frac{1}{\varepsilon_f \eta}z_1 + v \\ \dot{z_2} &= -|v|\frac{1}{\varepsilon_f}z_2 + v \\ F &= \frac{f_1}{\varepsilon_f \eta}z_1 - \frac{f_2}{\varepsilon_f}z_2. \end{cases} \tag{2.13}$$

This form gives state variables with the same dimension as the state in the Lugre model, and the coefficients can therefore be compared with the parameters in the Lugre model.

2.5 Linearization

Linearisation of (2.13) around an arbitrary equilibrium point z_0,v_0 yields

$$\begin{cases} \dot{z_1} &= -\frac{1}{\varepsilon_f \eta}|v|\Big|_{v_0,z_{10}} z_1 + \Big(1 - \frac{1}{\varepsilon_f \eta}z_1 \mathrm{sgn}(v)\Big)\Big|_{v_0,z_{10}} v \\ \dot{z_1} &= -\frac{1}{\varepsilon_f \eta}|v|\Big|_{v_0,z_{20}} z_2 + \Big(1 - \frac{1}{\varepsilon_f}z_2 \mathrm{sgn}(v)\Big)\Big|_{v_0,z_{20}} v \\ F &= \frac{f_1}{\varepsilon_f \eta}z_1 - \frac{f_2}{\varepsilon_f}z_2. \end{cases}$$

The above equations are not valid for equilibrium points $v_0 = 0$ because of the sign function, which is not defined for input argument zero. In the case $z_0 = 0$ and $v_0 = 0$ there is no problem however, and the equations become

$$\begin{cases} \dot{z_1} &= v \\ \dot{z_1} &= v \\ F &= \frac{f_1}{\varepsilon_f \eta} z_1 - \frac{f_2}{\varepsilon_f} z_2, \end{cases} \tag{2.14}$$

or with integrated state variables

$$F = \sigma x, \tag{2.15}$$

with

$$\sigma = \frac{f_1 - \eta f_2}{\varepsilon_f \eta} \tag{2.16}$$

being the stiffness. For a free mass system with Bliman-Sorine friction and viscous friction the equation of motion then becomes

$$\ddot{x} + \frac{\alpha}{m}\dot{x} + \frac{f_1 - \eta f_2}{m \varepsilon_f \eta} x = 0. \tag{2.17}$$

Comparison with the standard form

$$\ddot{x} + 2\zeta\omega\dot{x} + \omega^2 x = 0 \tag{2.18}$$

yields the natural frequency

$$\omega = \sqrt{\frac{f_1 - \eta f_2}{m \varepsilon_f \eta}} \tag{2.19}$$

and the damping

$$\zeta = \frac{\alpha}{2}\sqrt{\frac{\varepsilon_f \eta}{m\,(f_1 - \eta f_2)}}. \tag{2.20}$$

Note that the damping ζ is proportional to the viscous friction α, and that there is no way to control the linearized damping without changing other important model properties. With zero viscous friction the damping is zero, and we can expect oscillatory behaviour from the system.

For an equilibrium point $z_0 \neq 0$,$v_0 = 0$ we get

$$\begin{cases} \dot{z_1} &= \left(1 - \frac{1}{\varepsilon_f \eta} z_1 \mathrm{sgn}(v)\right)|_{v, z_{10}} v \\ \dot{z_1} &= \left(1 - \frac{1}{\varepsilon_f} z_2 \mathrm{sgn}(v)\right)|_{v, z_{20}} v \\ F &= \frac{f_1}{\varepsilon_f \eta} z_1 - \frac{f_2}{\varepsilon_f} z_2. \end{cases}$$

Integrating the states for a motion $v > 0$ gives us

$$F = \left(\frac{f_1}{\varepsilon_f \eta}\left(1 - \frac{1}{\varepsilon_f \eta} z_{10}\right) - \frac{f_2}{\varepsilon_f}\left(1 - \frac{1}{\varepsilon_f} z_{20})\right)\right) x$$

and for a motion $v < 0$ we have

$$F = \left(\frac{f_1}{\varepsilon_f \eta}\left(1 + \frac{1}{\varepsilon_f \eta} z_{10}\right) - \frac{f_2}{\varepsilon_f}\left(1 + \frac{1}{\varepsilon_f} z_{20})\right)\right) x.$$

I.e. the stiffness of each linearized first order system is increased by a direction dependent factor. The change in stiffness for the total system can not be described by factors, but is given by the above equations.

2.6 Asymmetric friction

In real system the friction characteristics are often asymmetric. The kinetic friction as well as the stiction force might very well be dependent on direction. It is straightforward to introduce asymmetric friction in the Bliman & Sorine model. The model is simply used with parameters defined as

$$\begin{bmatrix} \varepsilon_f & \eta & f_1 & f_2 \end{bmatrix} = \begin{cases} \begin{bmatrix} \varepsilon_f^- & \eta^- & f_1^- & f_2^- \end{bmatrix} & v < 0, \\ \begin{bmatrix} \varepsilon_f^+ & \eta^+ & f_1^+ & f_2^+ \end{bmatrix} & v > 0. \end{cases} \tag{2.21}$$

From (2.12) we see that the discontinuity of the parameters with respect to v still give continuous right hand sides of the equations, which means that even the first derivative of F is continuous. The linearized equations also handle asymmetric parameters.

2.7 Modeled friction phenomena

There seem to be a confusion in the nomenclature regarding the Stribeck effect. In [5, 6, 7] the Stribeck effect denotes the negative slope of the friction force versus velocity plot during the transient of a dynamic motion. It is clear that there must be a drop in the friction force from the stiction force to reach the Coulomb force. The Stribeck effect as described in 1.2 is asymptotic and gives an increase of the friction force with decreasing velocities, as observed experimentally. In this report the Stribeck effect denotes the steady-state phenomenon described in section 1.2.

For system trajectories with decreasing velocities starting from a state with the kinetic friction $f_1 - f_2$ the Bliman model does not give an increase in friction force as predicted by the Stribeck effect.

Otherwise the model includes pre-sliding displacement and stiction. Since the model after a transient in an uni-directional motion gives a constant friction force, it can not reproduce phenomena like frictional lag.

2.8 Parameter identification

The authors of the model propose a parameter identification scheme based of the hysteresis plot of friction force versus displacement during a cyclic motion with sign changes of velocity. See figure 2.2. After having identified the two points (s_e, f_s) and (s_p, f_k) in this plot the parameters are given by the following map $\begin{bmatrix} f_s & f_k & s_e & s_p \end{bmatrix} \mapsto \begin{bmatrix} f_1 & f_2 & \varepsilon_f & \eta \end{bmatrix}$:

$$\begin{cases} f_1 &= \frac{(m_1 m_2 + 2)p}{2(p-1)} f_k \\ f_2 &= \frac{m_1 m_2 p + 2}{2(p-1)} f_k \\ \epsilon_f &= \frac{s_p}{3} \\ \eta &= \frac{m_1 m_2 + 2}{m_1 m_2 p + 2} \end{cases} \tag{2.22}$$

with m_1 and m_2 defined as

$$m_1 = \frac{f_s - f_k}{f_k}, \; m_2 = e^{3 s_e / s_p},$$

and $p > 0$ is the solution of

$$\frac{m_1 m_2 + 2}{m_1 m_2} \ln p = (p-1) \ln m_2. \tag{2.23}$$

This solution exists and is unique if and only if

$$\ln m_2 < \frac{m_1 m_2 + 2}{m_1 m_2},$$

for example when $3s_e < s_p$. This condition imposes constraints on which physical systems that are possible to model. The condition says that for a system with a presliding displacement s_e, the friction force drop must not have been completed before $3s_e$. In the section on model validation this problem becomes real when identification is carried out on an experimental setup.

The inverse of (2.22) is

$$\begin{cases} f_k &= f_1 - f_2 \\ f_s &= f_k + 2f_2 \left(\frac{\eta f_2}{f_1}\right)^{\frac{\eta}{1-\eta}} (1-\eta) \\ s_e &= \frac{\varepsilon\eta}{1-\eta} \ln \frac{f_1}{\eta f_2} \\ s_p &= 3\varepsilon_f. \end{cases} \tag{2.24}$$

In section 2.9 this map is further investigated.

In the identification procedure given by (2.22) the viscous friction is not taken into account, but has to be identified separately. This is fairly straightforward. A typical hysteresis curve is given for a simulation of an inertial system with Bliman & Sorine friction in figure 2.3. A sinusoidal input torque has been applied. The importance of the viscous friction term is clearly seen

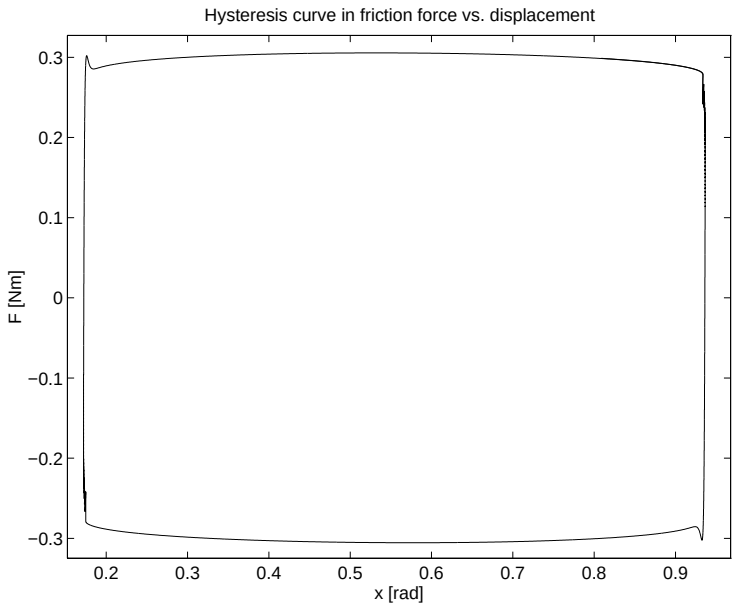

Figure 2.3 Simulated hysteresis curve for simple inertial system with Bliman & Sorine friction and a sinusoidal input torque.

in figure 2.4, where the upper left of figure 2.3 is seen in detail, and where the

hysteresis curve with the viscous friction subtracted is shown together with the original curve. All parameters are taken from a real identification case.

The identification procedure is not free from problems however. The point (s_p, f_k) is not very well defined, but up to the user to determine by hand. An example will illustrate a potential problem. Can small variations in the position of this point give large variations in parameters or system properties? Identification is done from a simulated model response of a mass system with Bliman & Sorine friction. If the identification procedure works well we of course expect to get the parameters used in the simulation as result. The correct parameter values were $\left[\begin{array}{ccccc} f_1 & f_2 & \varepsilon_f & \eta & \alpha \end{array}\right] = \left[\begin{array}{ccccc} 0.4224 & 0.1438 & 0.0023 & 0.4999 & 0.0177 \end{array}\right]$. In figure 2.4 (s_e, f_s) has been hold fixed while (s_p, f_k) has been identified as the points 1–6 respectively. The sensitivity of the identified parameters for these choices is shown in table 2.1. Notice that the identified value best corresponding to these parameters is number 3. A point that does not even lie on the hysteresis curve! In figure 2.5 simulated model responses of the different identified parameters corresponding to the different choices of (s_p, f_k) are shown. There are differences. It can be discussed if they are of a significant magnitude though. Most important is probably the differing kinetic friction. The difference between the extremes is about 5 %.

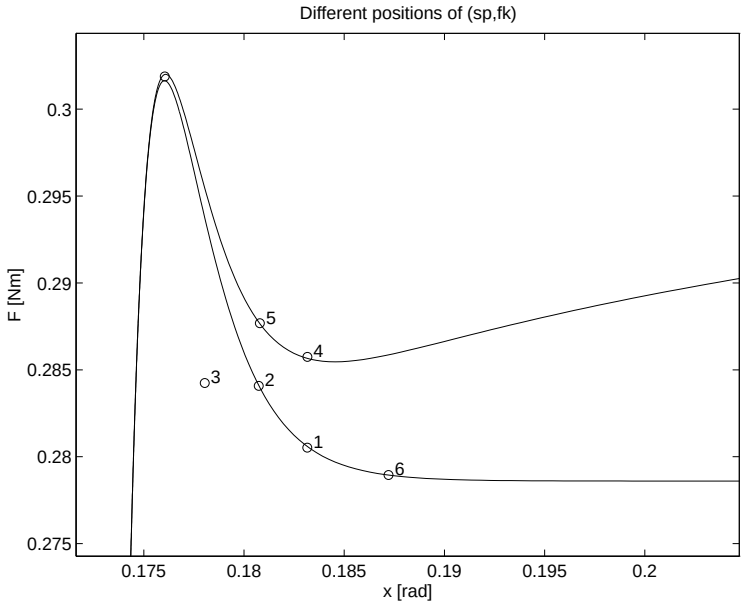

Figure 2.4 Detail of simulated hysteresis curve for Bliman & Sorine friction, with and without visous friction term. Different choices of the parameters (s_p, f_k) are shown.

A serious drawback of this procedure is the difficulty to introduce optimization. An averaged system response made up of a series of experiments might be used for the identification, but still it is up to the user to pick the identification parameters graphically. A non-gradient optimization procedure such as the simplex method might be used to minimize the square error of the experimental response and a simulated. Involving four varables and an integration in each step this seems difficult though.

Another difficulty has also been seen. If a certain model response is demanded by means of the identification parameters $\left[\begin{array}{cccc} f_k & f_s & s_e & s_p \end{array}\right]$, then

No.	f_k	s_p	f_1	f_2	ϵ_f	η
1	0.2805	0.0109	0.3192	0.0387	0.0036	0.2227
2	0.2841	0.0084	0.3321	0.0480	0.0028	0.2974
3	0.2842	0.0057	0.4139	0.1296	0.0019	0.5185
4	0.2857	0.0109	0.3144	0.0286	0.0036	0.2066
5	0.2877	0.0085	0.3245	0.0368	0.0028	0.2766
6	0.2790	0.0149	0.3076	0.0287	0.0050	0.1500

Table 2.1 The sensitivity of the identified parameters for the choice of the position of (s_p, f_k). (s_c, f_s) is fixed to $(0.0037, 0.3019)$.

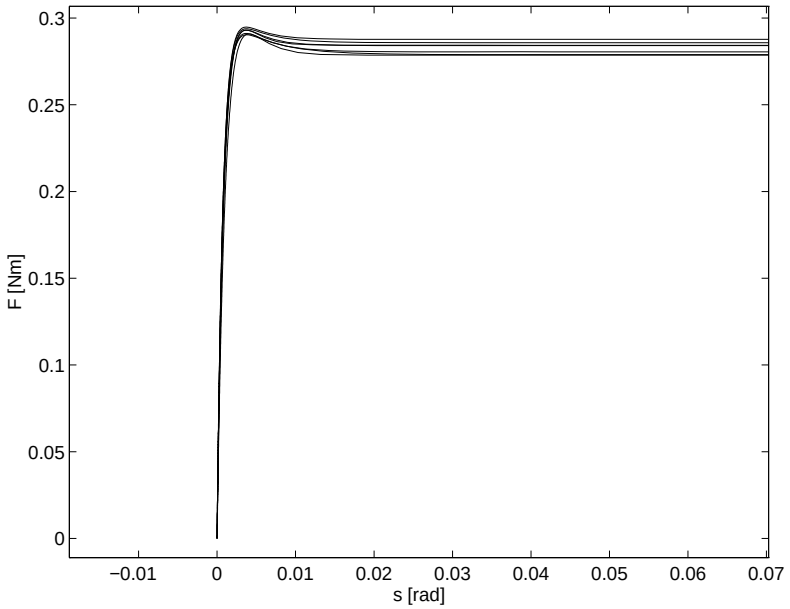

Figure 2.5 Sensitivity of identification procedure. Simulated model responses for the identified parameters obtained by different choices of the parameters (s_p, f_k).

the obtained model response may differ from this. f_k, s_e, s_p is modeled correctly, but f_s seems to be too small. Even though the map (2.22) has a solution for the identification parameters we are not guaranteed that the model will have the properties defined by these parameters when used in simulations. This problem is further discussed in section 2.9.

Identification of asymmetric friction is straightforward, the above graphical method is just applied on the hysteresis plot in the parts corresponding to positive and negative velocity respectively.

2.9 Simulations

In this section some characteristics of the Bliman & Sorine model are highlighted by simulations. The corresponding simulations are also done for the Lugre model later on. Most simulations are done on the model in figure C.2 of the experimental setup described in appendix C. The parameters used for the two models are matched. Mainly two sets of parameters have been used for each model. The first is a result of earlier identification experiments of

the setup decribed in appendix C. From these experiments Lugre parameters have been identified, and Bliman & Sorine parameters have then been identified from simulations of the Lugre system. The second parameter set is a result from the identification experiments carried out in this work. In this case both the parameters for the Lugre model and the Bliman & Sorine model are identified directly from experiments.

Integration of the model

In this section we regard either the free friction model with a velocity input, or the friction model in interconnection with an inertial system and an input torque.

In a system in rest with zero input force the friction force is zero. For the Bliman & Sorine model this is equivalent to the sum of the states being zero,

$$F = 0 \iff x_1 + x_2 = 0.$$

Note that this does not imply that the states are zero. This means that for a system in rest with zero input torque, the internal states of the friction model need not be zero. In simulations starting from rest the states are often chosen to be zero though. What are the implications of the choice of initial conditions?

Given a certain model parameter set we are promised a certain model response defined by the identification parameters. This is only valid if the system is in a cyclic symmetric stick-slip hysteretic motion where the states are saturated in each period. This kind of motion will in the following be refered to as *saturated hysteretic motion*. More precisely the stiction torque f_s, the pre-sliding displacement s_e and the plastic displacement s_p depend on initial conditions. f_k is independent of initial conditions.

To understand this, regard the solution of (2.7) for a motion $\mathrm{sgn}(v) = 1$. Integrating (2.7) with arbitrary initial conditions $x_1(0) = x_{10}$ and $x_2(0) = x_{20}$ gives

$$\begin{cases} x_1(s) &= f_1 + (x_{10} - f_1)e^{-\frac{1}{\varepsilon_f \eta}s} \\ x_2(s) &= -f_2 + (x_{20} + f_2)e^{-\frac{1}{\varepsilon_f}s} \\ F(s) &= x_1(s) + x_2(s). \end{cases} \tag{2.25}$$

Looking for a maxima $s = s_e$ in (2.25) we write

$$F(s) = f_1 + (x_{10} - f_1)e^{-\frac{1}{\varepsilon_f \eta}s} - f_2 + (x_{20} + f_2)e^{-\frac{1}{\varepsilon_f}s}.$$

Setting $F'(s_e) = 0$ we get

$$\frac{x_{10} - f_1}{\varepsilon_f \eta} e^{-\frac{1}{\varepsilon_f \eta}s_e} - \frac{x_{20} + f_2}{\varepsilon_f} e^{-\frac{1}{\varepsilon_f}s_e} = 0 \iff$$

$$\frac{-x_{10} + f_1}{(x_{20} + f_2)\eta} = e^{-\left(\frac{1}{\varepsilon_f} - \frac{1}{\varepsilon_f \eta}\right)s_e},$$

leading to

$$s_e = \frac{\varepsilon_f \eta}{1 - \eta} \ln \frac{-x_{10} + f_1}{(x_{20} + f_2)\eta}. \tag{2.26}$$

The maximum friction torque corresponding to this maxima is given by inserting (2.26) in (2.25):

$$\begin{aligned} F(s_e) &= f_1 - f_2 + (x_{10} - f_1)\left(\frac{(x_{20}+f_2)\eta}{-x_{10}+f_1}\right)^{\frac{1}{1-\eta}} \\ &+ (x_{20}+f_2)\left(\frac{(x_{20}+f_2)\eta}{-x_{10}+f_1}\right)^{\frac{\eta}{1-\eta}}. \end{aligned} \tag{2.27}$$

Remark 1. Note that (2.26) implies that for all initial conditions $[\ x_{10} \quad x_{20}\ ] = \beta[\ -f_1 \quad f_2\ ]$, $\beta \geq 0$, the maximum is found at the same relative displacement

$$s_e = \frac{\varepsilon_f \eta}{1-\eta} \ln \frac{f_1}{f_2 \eta}. \tag{2.28}$$

The initial conditions corresponding to the sign change of the velocity in the saturated hysteretic motion fulfills this condition, and consequentely (2.28) is the expression for s_e given by (2.24). Also zero initial conditions fulfills the condition.

Now regard the saturated hysteretic motion. In this motion the states are $x_1 = \pm f_1$ and $x_2 = \mp f_2$ at the sign change of velocity, defining the origo of the absolute relative displacement s. For a motion for which $\mathrm{sgn}(v) = 1$ $x_{10} = -f_1$ and $x_{20} = f_2$. Equation (2.25) becomes

$$\begin{cases} x_1(s) &= f_1\left(1 - 2e^{-\frac{1}{\varepsilon_f \eta}s}\right) \\ x_2(s) &= -f_2\left(1 - 2e^{-\frac{1}{\varepsilon_f}s}\right) \\ F(s) &= x_1(s) + x_2(s). \end{cases} \tag{2.29}$$

The maximum of (2.29) is found at s_e given by (2.28). Together with (2.27) this yields

$$F(s_e) = f_1 - f_2 + 2f_2\left(\frac{f_2\eta}{f_1}\right)^{\frac{1}{1-\eta}}(1-\eta). \tag{2.30}$$

This is the expression for f_s given by (2.24).

With zero initial conditions we have $x_{10} = 0$, $x_{20} = 0$. Inserting this in (2.25) yields

$$\begin{cases} x_1(s) &= f_1\left(1 - e^{-\frac{1}{\varepsilon_f \eta}s}\right) \\ x_2(s) &= -f_2\left(1 - e^{-\frac{1}{\varepsilon_f}s}\right) \\ F(s) &= x_1(s) + x_2(s). \end{cases} \tag{2.31}$$

The maximum of (2.31) is also found at s_e given by (2.28). Together with (2.27) this yields

$$F(s_e) = f_1 - f_2 + f_2\left(\frac{f_2\eta}{f_1}\right)^{\frac{1}{1-\eta}}(1-\eta). \tag{2.32}$$

Equations (2.26) and (2.27) show that different initial conditions give different friction torque maxima. In particular initial conditions belonging to the saturated hysteretic motion and zero initial conditions give maxima at the same relative displacement, but (2.30) and (2.32) shows that the maximum torques are different. Actually the difference $f_s - f_k$ differs by a factor

two. (2.29) and (2.31) shows that they have the same asymptotical response though, they both approach $F(s) = f_1 - f_2 = f_k$ for large s. This is the definition of f_k as given by (2.24).

Zero initial conditions are used in most simulations. That means that the transient response can not be expected to have the properties defined by the identification parameters. The problem is that the Bliman & Sorine model is described by two states, and that these states have to be "in phase" with each other in a way defined by the saturated hysteretic motion, to give the behaviour defined by the identification parameters. In other words the states have to be saturated before each sign change of velocity to give the demanded model response. A solution to this, at least for the first transient, could be to start simulations with non-zero initial conditions, as if the system was in the saturated hysteretic motion. This does not solve the problem completely though. The model responses discussed above are these of the free friction model. Connected to a physical system the situation is further complicated. In simulations of physical systems with Bliman & Sorine friction there are oscillations in the friction force due to the characteristics of the linearized equations, see (2.20). The trajectory of the friction model does not normally in these systems follow the trajectory of a pure saturated hysteretic motion, and therefore the friction model properties become different from these given by the identification parameters. The oscillatory behaviour is further treated in section 2.9.

Some of the above is illustrated by figure 2.6 which shows some model trajectories for the free friction model with a sinusoidal velocity input, and for the friction model in a simple physical system, composed of an inertia under influence of Bliman & Sorine friction and a sinusoidal input force. The input signals are chosen to give saturation of the states in each period. Model friction is given by $F = x_1 + x_2$. In the plot the level curve $x_1 + x_2 = 0$ have been plotted. Intersection between this line and the trajectory indicates where zero friction torque is reached. The maximum stiction torques correspond to the largest perpendicular distance between the dotted level curve $x_1 + x_2 = 0$ and the trajectories. (It is not equal to this distance though.) In the left figure we see the impact of zero initial conditions $x_0 = \begin{bmatrix} 0 & 0 \end{bmatrix}$. The first stiction torque is less than the succeeding. The stiction torque of the physical system is less than the stiction torque for the free friction model. The oscillations force the trajectory away from the free model trajectory. In the right plot we see the situation for initial conditions from the saturated hysteretic motion $x_0 = \begin{bmatrix} -f_1 & f_2 \end{bmatrix}$. For the free model the trajectory instantaneously follows the trajectory of the saturated hysteretic motion. In the composed system large oscillations are present initially, and asymptotically the trajectory approaches a trajectory inside the free model trajectory. It is veryfied in the simulations of the free friction model that $f_s - f_k$ differs a factor two for the first stiction torque, comparing zero initial conditions with initial conditions in the saturated hysteretic cyclic motion. For input signals that do not saturate the states in each period the trajectories can show complex behaviour. We do not illustrate this. Instead we show what can happen when the input torque amplitude is less than the sticion torque demanded by the identification parameters, but greater than the stiction torque of the first transient. An example is shown in figure 2.7, where an inertial system with Bliman & Sorine friction and sinusoidal non-biased input torque has been simulated with zero initial conditions. The result is an asymmetric motion which gives break-away only in one direction. The stiction torque demanded by the identification pa-

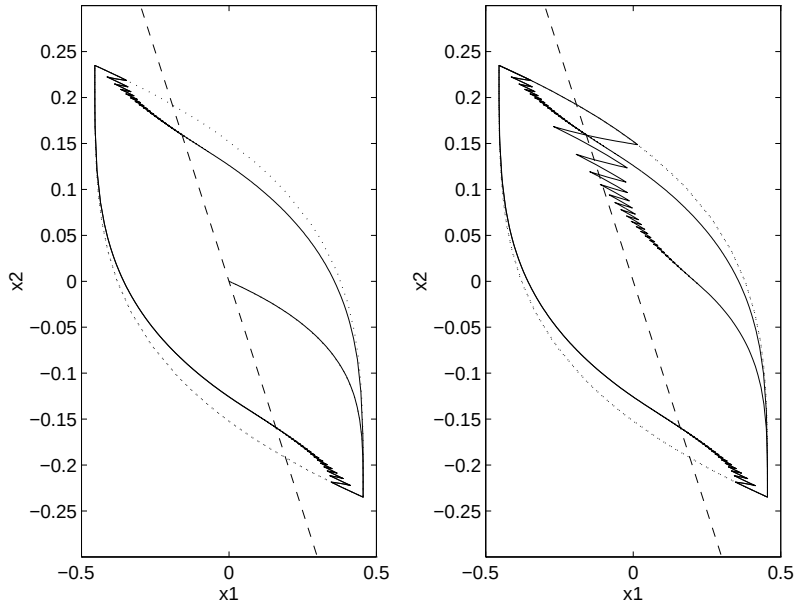

Figure 2.6 Bliman & Sorine model trajectories for different initial conditions. Dotted lines: Free friction model with sinusoidal velocity input. Solid lines: Friction model in inertial system with sinusoidal input torque. Dashed lines: The level curve $x_1 + x_2 = 0$. Left: Zero initial condition. Right: Saturated hysteretic motion initial condition.

rameters is 0.38 Nm, and the amplitude of the input torque is 0.35 Nm. The physical relevance of this behaviour can probably be questioned.

In the report zero initial conditions are used consequently, yielding sometimes strange behaviour.

Free model

The figures 2.8 and 2.9 show the response of the free Bliman & Sorine friction model with sinusoidal velocity inputs. In figure 2.8 we see that the first break-away force is smaller than the succeeding due to zero initial conditions. The entity $F_s - F_C$ differs a factor two.

In figure 2.10 the rate of the applied input velocity has been changed, and the friction force responses versus displacement are plotted. The rate independecy of the model implies that the response does not change with input rate, as seen in the figure.

Interconnected model

The system simulated is a simple mass with friction system with an externally applied sinusoidal force $u = a\sin(\omega t)$. The model parameters are

$$\begin{bmatrix} f_1 & f_2 & \varepsilon_f & \eta & \alpha \end{bmatrix} = \begin{bmatrix} 0.4224 & 0.1438 & 0.0023 & 0.4999 & 0 \end{bmatrix},$$

i.e. no viscous friction term is used. First the system is simulated with an amplitude of the input torque $a = 0.305$, which is just above the break-away torque. The rate of the sinusoid is $\omega = 5$ rad/s. In figures 2.11 and 2.12 the friction force versus time and displacement plots are shown.

We see that there are some oscillations at the sign change of the velocity. The origin of these can be found in the linearized equations. Since we have

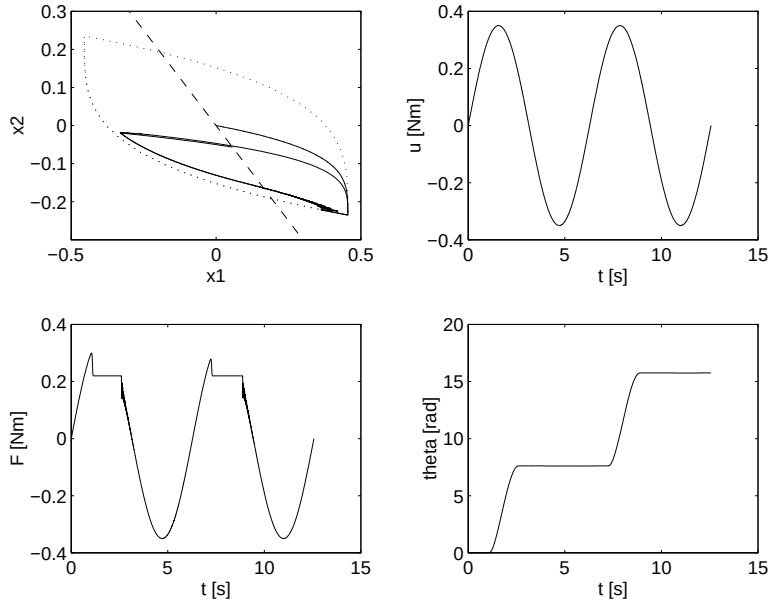

Figure 2.7 Simulation of inertial system with Bliman & Sorine friction F and symmetric non-biased sinusoidal torque input u. Upper left: Friction model trajectory, solid lines: friction model in inertial system with sinusoidal torque input, dotted lines: free friction model with sinusoidal velocity input for comparison. Upper right: Input torque. Lower left: Non-linear friction torque F (not the viscous part). Lower right: Angular position of the inertial load.

no viscous friction we have $\alpha = 0$, and thus the linearised damping is zero according to (2.20).The predicted period of the oscillations is 18 ms from (2.19), and the period found in the simulation is 19 ms. From (2.20) we see that a non-zero damping is introduced by using viscous friction, i.e. $\alpha > 0$.

The more realistic case with non-zero viscous friction, $\alpha = 0.0177$ Nms/rad, is simulated and plotted in figures 2.13 and 2.14. We see that the oscillations are diminuished, but do not disappear.

The most serious drawback with this oscillative property of the Bliman & Sorine friction model is that there is no way to increase the stiction damping, which is a low velocity property, without changing the large velocity property of viscous friction. In other words, we lack a degree of freedom.

The oscillations are relatively large in amplitude, and give a behaviour not reported by friction experimentally. The parameters used in the simulations are realistic. Moreover the oscillations consume computational power in the simulations. With everything else constant, the number of flops used in the simulation was reduced by 34% when non-zero viscous friction was introduced, and the oscillations were reduced. This can be compared with the Lugre model, for which the number of flops *increased* with 1% under the same circumstances. For a given system without viscous friction the Bliman & Sorine model required 254% more flops than the Lugre model for a given simulation. When viscous friction was introduced the overhead was reduced to 167 % more for the Bliman & Sorine model than for the Lugre model.

Small displacements

For small displacements the Bliman & Sorine model is expected to behave like a linear spring. To verify this behaviour we simulate an inertial system with

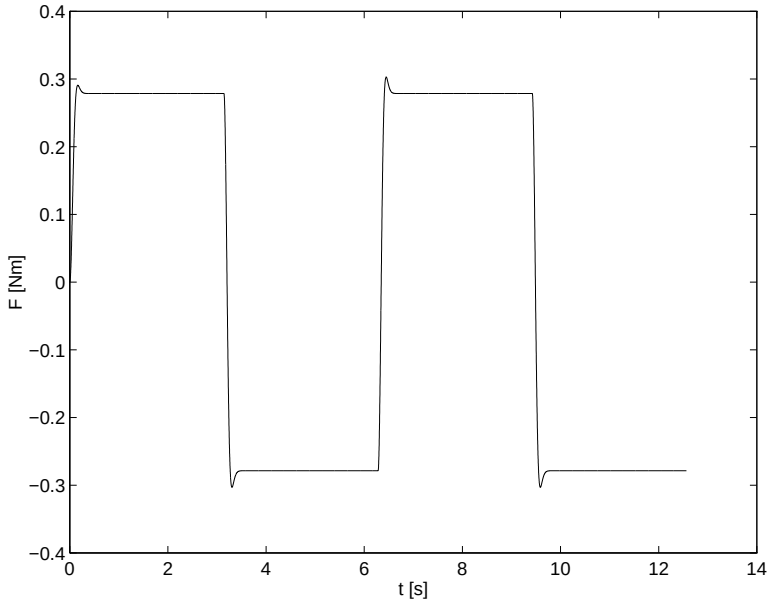

Figure 2.8 Simulation of free Bliman & Sorine friction model with sinusoidal input velocity. Friction force versus time.

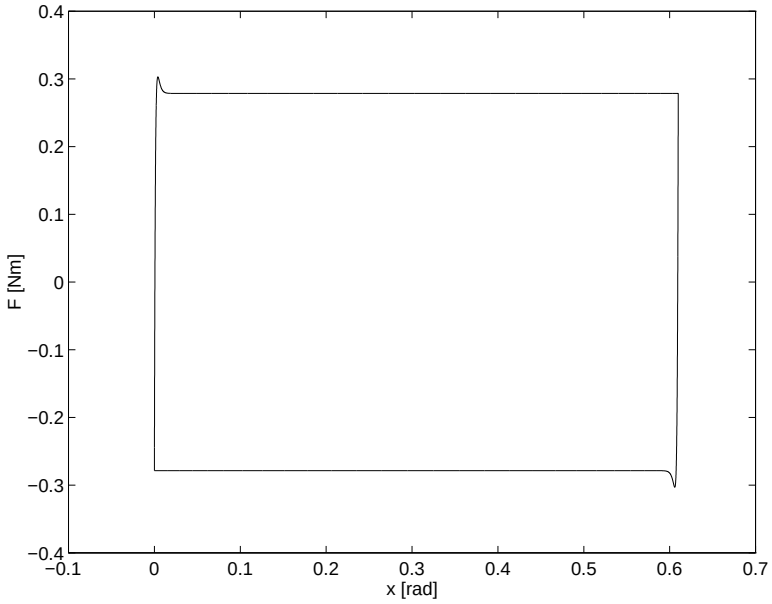

Figure 2.9 Simulation of free Bliman & Sorine friction model with sinusoidal input velocity. Friction force versus displacement.

Bliman friction and external force $u = B + A\sin(\omega t)$. The inertia is $J = 0.0025$ Nms/rad, and the Bliman model parameters are

$$\begin{bmatrix} f_1 & f_2 & \varepsilon_f & \eta & \alpha \end{bmatrix} = \begin{bmatrix} 1.6130 & 1.0869 & 0.0201 & 0.6347 & 0.0180 \end{bmatrix}.$$

Equation (2.16) gives a linear stiffness $\sigma = 72$ Nm/rad. In figure 2.15 unidirectional input torques of different magnitudes are applied. We see that for small input torques we have an almost linear behaviour, while for larger

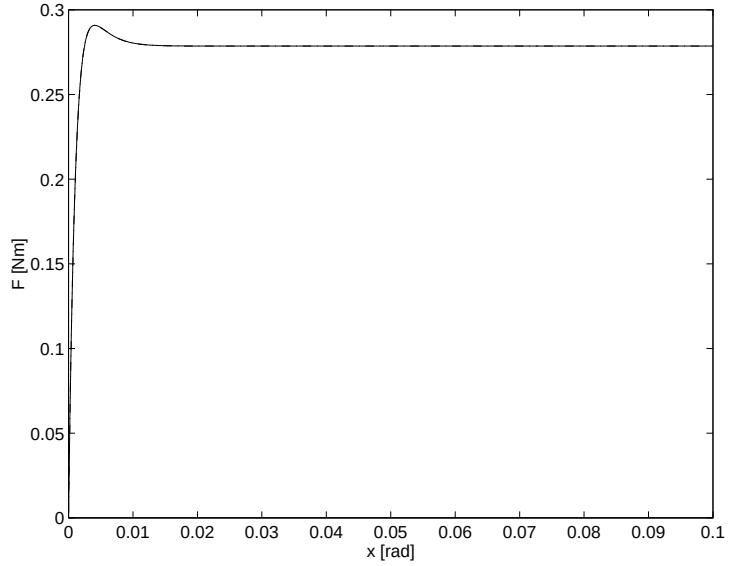

Figure 2.10 Simulations of free Bliman & Sorine friction model with sinusoidal input velocities of different rates. Friction force versus displacement.

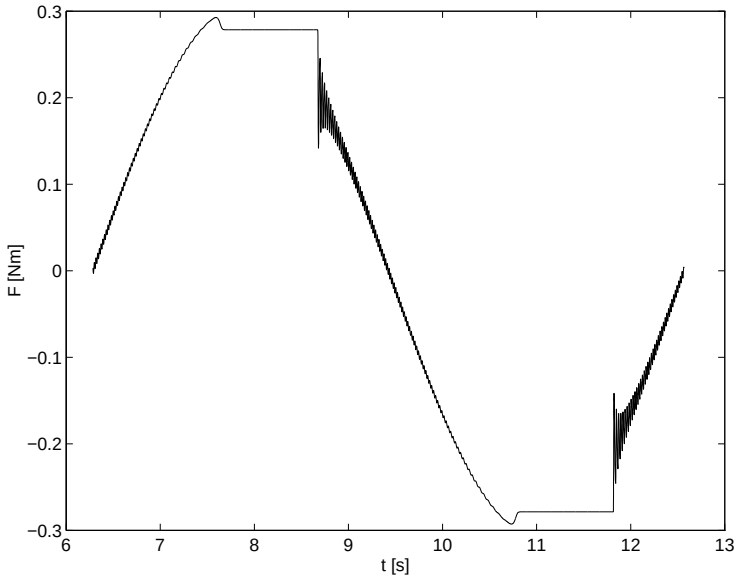

Figure 2.11 Simulation of simple inertial system with Bliman & Sorine friction and sinusoidal input torque. Zero viscous friction. Friction force versus time.

torques the response becomes non-linear and shows hysteresis. We see that unidirectional input torques do not take the system back to the initial position. In figure 2.16 symmetric bi-directional input torques with zero mean are used, and now the system return to the initial position.

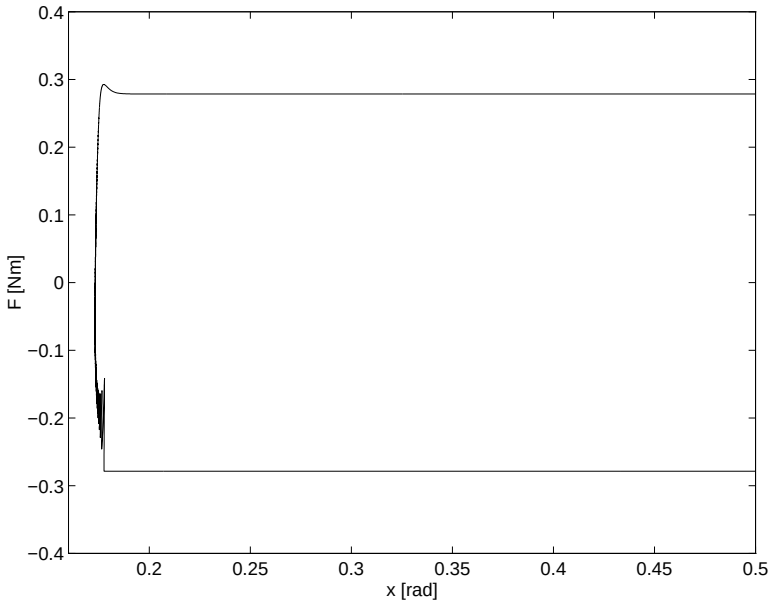

Figure 2.12 Simulation of simple inertial system with Bliman & Sorine friction and sinusoidal input torque. Zero viscous friction. Friction force versus displacement.

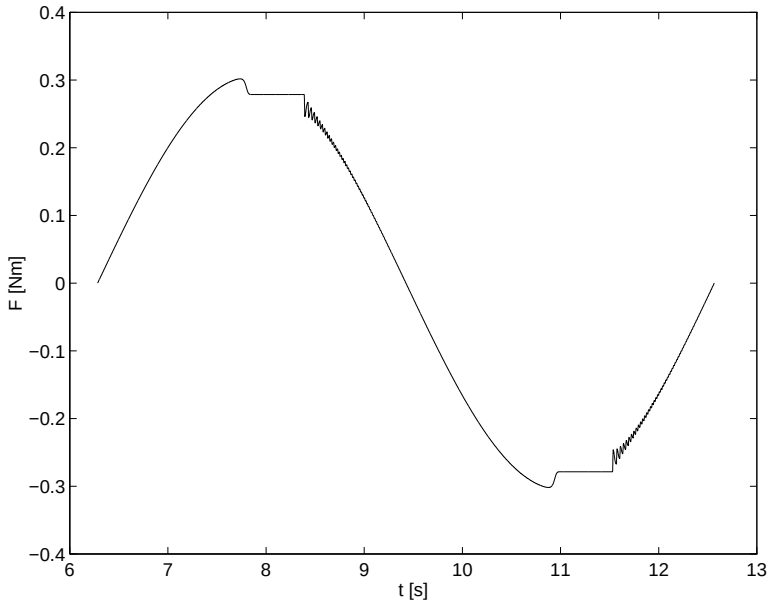

Figure 2.13 Simulation of simple inertial system with Bliman & Sorine friction and sinusoidal input torque. Non-zero viscous friction. Friction force versus time.

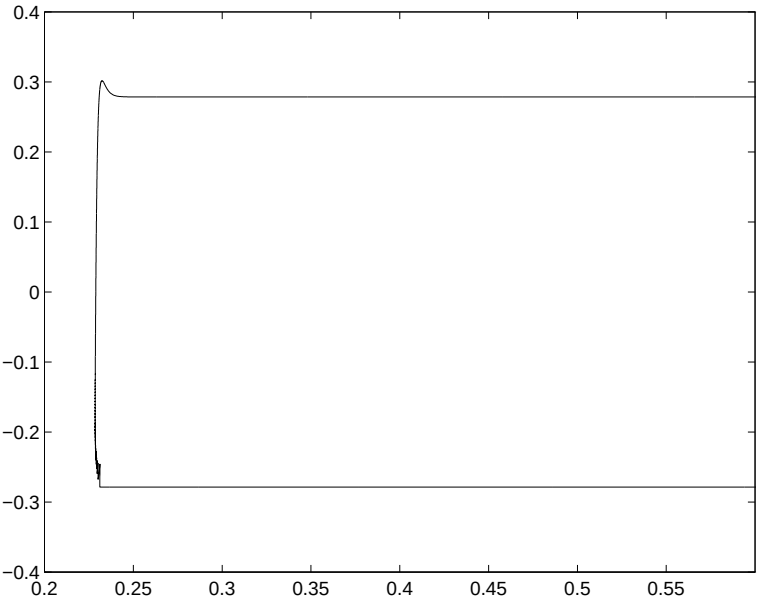

Figure 2.14 Simulation of simple inertial system with Bliman & Sorine friction and sinusoidal input torque. Non-zero viscous friction. Friction force versus displacement.

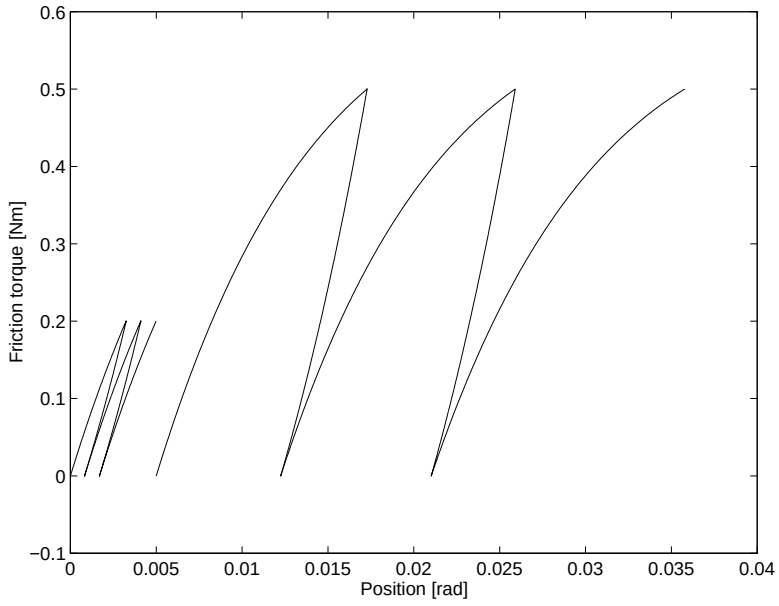

Figure 2.15 Bliman & Sorine model responses to input torque $u = B + A\sin(\omega t)$ for $B = 0.1$ Nm, $A = 0.1$ Nm and $B = 0.25$ Nm, $A = 0.25$ Nm

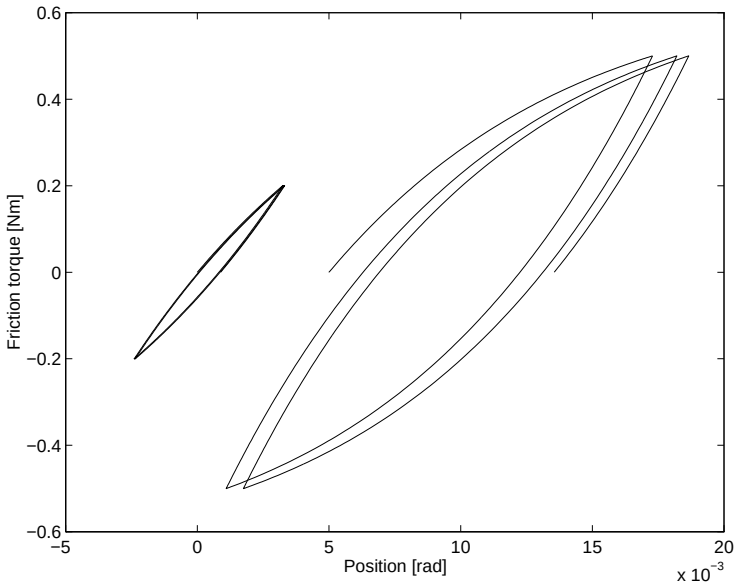

Figure 2.16 Bliman & Sorine model responses to input torque $u = B + A\sin(\omega t)$ for $B = 0$ Nm, $A = 0.2$ Nm and $B = 0$ Nm, $A = 0.5$ Nm

3. The LuGre model

The *LuGre model* [11] is a friction model proposed by Carlos Canudas de Wit[1], Henrik Olsson[2] Karl Johan Åström[2]and Pablo Lischinsky[1]. It is a dynamic model with the relative velocity between the bodies in contact as input, and the friction force as output. The model is inspired by steady state properties found experimentally, but none the less it models several dynamic phenomena as well. It approximates friction as a phenomenon caused by bristles in contact, which gives the parameters included simple physical interpretations. The model can be seen as an extension of the simplified Dahl model (1.8).The model has the following general form

$$\begin{cases} \frac{dz}{dt} &= v - \sigma_0 \frac{|v|}{g(v)} z \\ F &= \sigma_0 z + \sigma_1(v)\frac{dz}{dt} + f(v) \end{cases} \tag{3.1}$$

where $v(t)$ is the relative velocity of the bodies in contact. The meaning of the parameters and the choice of $g(v)$, $\sigma_1(v)$ and $f(v)$ will be discussed below.

3.1 Bristle interpretation of friction

As mentioned above the model is inspired by the interpretation of friction as the force generated by a system of bristles in contact. That is to say that the asperity junctions of the physical friction interface behaves like bristle contacts. The elastic deformation is described by the spring like behaviour of the bristles for small displacements, while the plastic deformation and rupture are captured by sliding of the bristles at larger displacements. See figure 3.1. The bristle interpretation was introduced by Haessig and Friedland 1990 [15], who proposed a model in which one regard the individual bristles. This is somehow inconvenient, and as an alternative they also presented a model which regards the aggregate behaviour of multiple bristles. The LuGre model gives a new formulation of this aggregate behaviour, while adding some extra features.

From this follows that for small displacements the model will behave in a spring like manner. The parameter σ_0 being the stiffness of the bristles, and $\sigma_1(v)$ the damping. The reason for eventually making σ_1 velocity dependent will be discussed later. For larger displacements sliding will occur. The transition to sliding dependends on the function $g(v)$ as well as the rate of change of velocity. Since σ_0 and σ_1 parametrize this dynamic behaviour they are refered to as *dynamic parameters*.

For constant velocities a steady state friction force

$$F_{ss} = g(v_{ss})\text{sgn}(v_{ss}) \tag{3.2}$$

is reached. Hence the function $g(v)$ is used to model the Stribeck effect. A choice of g which gives a good approximation of the Stribeck effect while having nice mathematical properties is

$$g(v) = \alpha_0 + \alpha_1 e^{-(v/v_0)^2}. \tag{3.3}$$

[1]Laboratoire d'Automatique de Grenoble (CNRS-INPG-UJF)
[2]Department of Automatic Control, Lund Institute of Technology

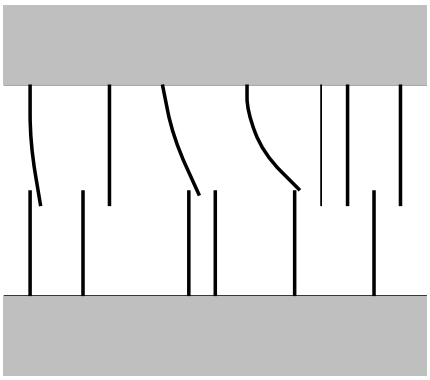

Figure 3.1 The friction interface between two surfaces is thought of as a contact between bristles. For simplicity the bristles on the lower part is shown as being rigid.

The sum $\alpha_0 + \alpha_1$ then correspond to stiction force and α_0 to Coulomb friction force. The parameter v_0 influences when transition from stick to slip is to appear. The parameters α_0, α_1 and v_0 thus models static behaviour, and are refered to as *static parameters*.

The term $f(v)$ is the viscous friction, which is important only for higher velocities, and does not influence the low velocity properties to a large extent. A common choice is linear viscous friction $f(v) = \alpha_2 v$.

The above discussion has lead us to the following particularization of the model, giving what we shall call the *standard parametrization*:

$$\begin{cases} \dot{z} &= v - \sigma_0 \frac{|v|}{g(v)} z \\ g(v) &= \alpha_0 + \alpha_1 e^{(v/v_0)^2} \\ F &= \sigma_0 z + \sigma_1 \dot{z} + \alpha_2 v \end{cases} \tag{3.4}$$

This is the published form of the model and the further analysis shall mostly regard this parametrization.

Nominal parameters for the model are given in table 3.1.

σ_0	σ_1	v_0	α_0	α_1	α_2
[N/m]	[Ns/m]	[m/s]	[N]	[N]	[Ns/m]
[Nm/rad]	[Nms/rad]	[rad/s]	[Nm]	[Nm]	[Nms/rad]
10^5	$2\sqrt{10^5}$	0.01	0.5	1	0.4

Table 3.1 Nominal Lugre parameters well suited for simulations. Units are given for parameters in force as well as torque systems.

3.2 Formulation in space variable

It is instructive to reformulate the Lugre model in the space variable $s = \int_0^t |v(\tau)| d\tau$, denoting absolute relative displacement. This is the distance covered since the last change of sign of velocity. The standard model (3.4) transforms to

$$\begin{cases} \frac{dz}{ds} &= \text{sgn}(v) - \sigma_0 \frac{1}{g(v)} z \\ F &= \sigma_0 z + |v| \sigma_1 \frac{dz}{ds} + \alpha_2 v. \end{cases} \tag{3.5}$$

Neglecting for a moment the small displacement damping and the viscous friction term, i.e. $\sigma_1 \equiv 0$ and $\alpha_2 \equiv 0$, we see that the resulting system

$$\frac{dF}{ds} = \sigma_0 \left(\text{sgn}(v) - \frac{1}{g(v)} F \right) \tag{3.6}$$

is a first order order model in space with a velocity dependent coefficient $\frac{\sigma_0}{g(v)}$, and the sign of the velocity scaled by σ_0 as input. In the standard parametrization $g(v)$ is bounded as $\alpha_0 \leq g(v) \leq \alpha_0 + \alpha_1$. Thus the output of (3.6) is bounded by the outputs of

$$\frac{dF}{ds} = \sigma_0 \text{sgn}(v) - \frac{\sigma_0}{\alpha_0 + \alpha_1} F \tag{3.7}$$

and

$$\frac{dF}{ds} = \sigma_0 \text{sgn}(v) - \frac{\sigma_0}{\alpha_0} F. \tag{3.8}$$

For low velocities (3.6) is close to the first of these bounding systems, while for higher velocities it becomes close to the second. These bounding systems are first order space invariant systems. That means that they are rate independent. The output only depends on the displacement, and not on the velocity. A rate dependency of the Lugre model is introduced by varying (3.6) in a velocity dependent way between the bounding systems. The transition between the two extremes of $g(v)$ is determined by the system velocity v and the model parameter v_0. To model a break-away force higher than the Coulomb friction force α_0 this transition needs to take place at a displacement for which the output of the first of the bounding systems is close to it's maximum. The earlier this transition takes place, the less the break-away force will be. This is in line with experimental observations. The space constant for the system (3.6), $\frac{g(v)}{\sigma_0}$, determines the pre-sliding displacement of the physical system. As the pre-sliding displacement is the displacement before break-away for velocities that let F reach close to it's maximum, i.e. follows the first bounding system, we have (assuming "close" is 90%)

PROPERTY 3.1
The pre-sliding displacement ε for a system with Lugre friction is approximately given by

$$\varepsilon = \frac{\alpha_0 + \alpha_1}{\sigma_0} \ln(10).$$

□

Although taking into account non-zero σ_1 and v_0 the above interpretations and results still holds. The σ_1-term introduces complex properties of the model though, as we shall see later. Since σ_1 is multiplied by $\dot{z}$, it gives a addition to the total friction that is proportional to the rate of change of z with respect to time. That means that when z increases, the increase in friction force becomes larger than what is given by (3.6), since $\dot{z} > 0$, and equivalently a decrease of z gives a larger total decrease in friction force than given by (3.6) since $\dot{z} < 0$. In (3.5) we see that $\sigma_0 \dot{z}$ transforms to $\sigma_1 |v| \frac{dz}{ds}$, i.e. this term is rate dependent. We thus have three rate dependencies in the model, the rate dependent variation of (3.6), the friction term $\sigma_1 \dot{z}$, and of course the viscous friction term $\alpha_2 v$.

In figure 3.2 the above properties are illustrated by plotting the bounding system responses and the response of (3.6) to a sinusoidal velocity input from zero initial conditions.

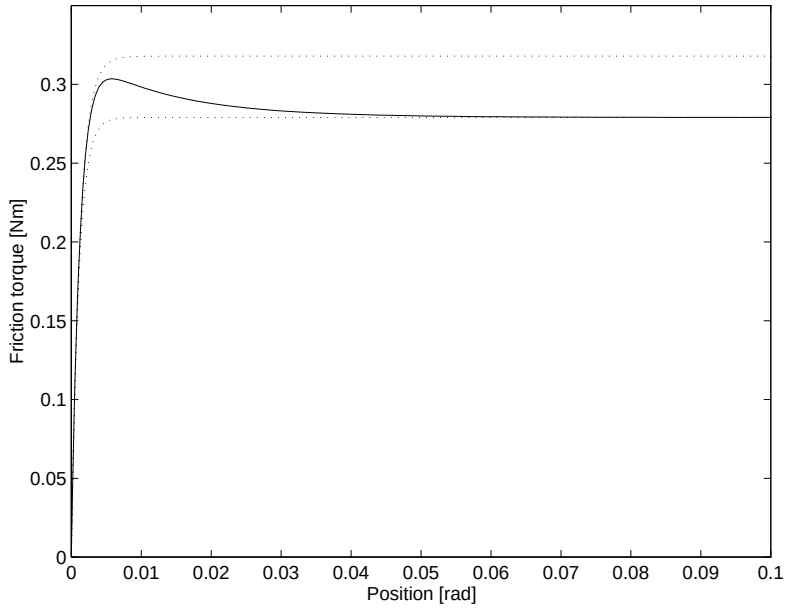

Figure 3.2 Lugre model response and responses of the bounding systems. Friction force versus displacement at break-away.

figure 3.3 shows how the transition between the bounding systems is dependent on the velocity. In the simulation $v_0 = 0.1$ rad/s. At this velocity the response is in the middle of the transition between the bounding systems.

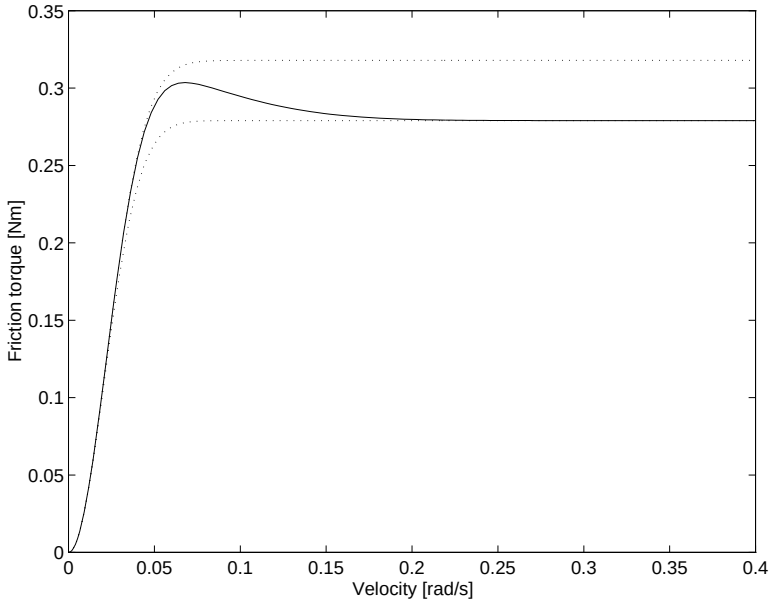

Figure 3.3 Lugre model response and responses of the bounding systems. Friction force versus velocity at break-away.

Further rewritings of 3.5 yield

$$\begin{cases} \frac{dz}{ds} &= \operatorname{sgn}(v) - \sigma_0 \frac{z}{g(v)} \\ F &= \sigma_0 z \left(1 - \sigma_1 \frac{|v|}{g(v)}\right) + (\sigma_1 + \alpha_2)\, v. \end{cases} \tag{3.9}$$

From this we can see that the term $\sigma_1 \dot{z}$ can be interpreted as an addition of σ_1 to the viscous friction, and a velocity dependent scaling of the small displacement stiffness σ_0 by a factor $1-\sigma_1 \frac{|v|}{g(v)}$. We spy here a potential problem as we see that this factor might become negative for large velocities. We shall return to this later.

Remark 1. The bounding systems are first order space invariant systems of the same kind used to form the Bliman & Sorine friction model. While the Bliman & Sorine model uses two systems of this kind in parallell to model stiction, the Lugre model uses one first order space variant system, which is bounded by two first order space invariant systems, to model the same phenomenon. Thus the Lugre model can describe the same phenomenon with one less state, while in addition the model becomes variant.

Remark 2. The bounding systems are in fact identical to the simplified Dahl model (1.8). The relation between the Lugre model and the Dahl model can be seen here.

3.3 Linearization of the model

In [22] linearization in stiction regime is carried out for the general Lugre model. Here the results are used on the standard parametrization (3.4) Linearisation around $v_0 = 0$ and $z_0 = 0$ gives[3]

$$\begin{cases} \frac{dz}{dt} &= v \\ F &= \sigma_0 z + (\sigma_1 + \alpha_2)\, v. \end{cases} \tag{3.10}$$

Integrating the first equation in (3.10) yields

$$F = \sigma_0 x + (\sigma_1 + \alpha_2)\, v.$$

For a simple free mass system this gives the following equation of motion for small displacements

$$M\ddot{x} + (\sigma_1 + \alpha_2)\, \dot{x} + \sigma_0 x = 0.$$

which when compared to the general second order differential equation

$$M\ddot{x} + 2\zeta\omega\dot{x} + \omega^2 x = 0$$

lets us identify the damping and the natural frequency as

$$\omega = \sqrt{\frac{\sigma_0}{M}} \tag{3.11}$$

and

$$\zeta = \frac{\sigma_1 + \alpha_2}{2\sqrt{M\sigma_0}}. \tag{3.12}$$

We see that (3.12) is quite similar to (2.20), but that in (3.12) we have the additional parameter σ_1 to control the damping. I.e. there is a way to modify the damping without changing explicitely other model properties. Of course

[3] v_0 in this context does not refer to the Stribeck velocity

changes in σ_1 affects the overall behaviour of the model, but we have one more degree of freedom in this extra parameter. In simulations with matched parameters the Lugre model also exhibits a much less oscillatory behaviour than the Bliman & Sorine model.

Linearization around $v_0 = 0$ and $z_0 \neq 0$ gives

$$\begin{cases} \frac{dz}{dt} &= G(v, z_0)v \\ F &= \sigma_0 z + (\sigma_1 G(v, z_0) + f'(0))\, v \end{cases} \tag{3.13}$$

where

$$G(v, z_0) = \begin{cases} \left(1 - \frac{\sigma_0 z_0}{g(0^+)}\right) & v > 0 \\ \left(1 + \frac{\sigma_0 z_0}{g(0^-)}\right) & v < 0 \end{cases}$$

and allows asymmetry of $g(v)$. The effect is that stiffness and damping are scaled by a factor $G(v, z_0)$.

3.4 Properties of the friction model $v \mapsto F$

Some passivity aspects

There are two reasons for wanting the model to be passive. Firstly passivity results can be used in stability analysis. But also passivity also reflects the physical property of power dissipation. For an input-output model that describes a physical process, and that gets all it's energy from the input, to be generally accepted, it ought to be passive, since that is how nature works. We will now take a closer look at some passivity properties, [22], of the standard parametrization (3.4).

PROPERTY 3.2
The standard model (3.4) is passive from $v \mapsto \sigma_0 z$ with respect to the storage function $V : z \mapsto \sigma_0 \frac{z^2}{2}$ for every choice of parameter values. □

Proof. It follows directly from the definition A.2 with $u \equiv v$ and $y \equiv z$ that

$$\begin{aligned} \int_0^t \sigma_0 z v d\tau &= \int_0^t \sigma_0 z(\dot{z} + \frac{\sigma_0}{g(v)}|v|z) d\tau \\ &= \int_0^t \sigma_0 z \dot{z} d\tau + \int_0^t \frac{\sigma_0^2}{g(v)}|v| z^2 d\tau \\ &= \sigma_0 \int_0^t z dz + \int_0^t \frac{\sigma_0^2}{g(v)}|v| z^2 d\tau \\ &\geq \sigma_0 \frac{z^2(t) - z^2(0)}{2} \end{aligned}$$

□

PROPERTY 3.3
Passivity for the mapping $v \mapsto \sigma_0 z + \sigma_1 \dot{z}$ holds with respect to the storage function $V : z \mapsto \sigma_0 \frac{z^2}{2}$ under the sufficient condition $\sigma_1 < \frac{4g(v)}{|v|}$. □

Proof. Definition A.2 with $u \equiv v$ and $y \equiv \sigma_0 z + \sigma_1 \dot{z}$ gives

$$\begin{aligned}
\int_0^t uy d\tau &= \int_0^t v(\sigma_0 z + \sigma_1 \dot{z}) d\tau \\
&= \int_0^t (\dot{z} + \sigma_0 \frac{|v|}{g(v)} z)(\sigma_0 z + \sigma_1 \dot{z}) d\tau \\
&= \int_0^t \sigma_0 z\dot{z} + \sigma_0^2 \frac{|v|}{g(v)} z^2 + \sigma_1 \dot{z}^2 + \sigma_0 \sigma_1 \frac{|v|}{g(v)} z\dot{z} d\tau \\
&= \sigma_0 \frac{z^2(t) - z^2(0)}{2} + \sigma_1 \int_0^t \dot{z}^2 + \sigma_0 \frac{|v|}{g(v)} z\dot{z} + \frac{\sigma_0^2}{\sigma_1} \frac{|v|}{g(v)} z^2 d\tau \\
&= \sigma_0 \frac{z^2(t) - z^2(0)}{2} \\
&+ \sigma_1 \int_0^t \dot{z}^2 + 2\frac{\sigma_0}{2} \frac{|v|}{g(v)} z\dot{z} + (\frac{\sigma_0}{2} \frac{|v|}{g(v)} z)^2 - (\frac{\sigma_0}{2} \frac{|v|}{g(v)} z)^2 \frac{\sigma_0^2}{\sigma_1} \frac{|v|}{g(v)} z^2 d\tau \\
&= \sigma_0 \frac{z^2(t) - z^2(0)}{2} \\
&+ \sigma_1 \int_0^t (\dot{z} + \frac{\sigma_0}{2} \frac{|v|}{g(v)} z)^2 d\tau + \sigma_1 \sigma_0^2 \int_0^t (\frac{1}{\sigma_1} - \frac{1}{4} \frac{|v|}{g(v)}) \frac{|v|}{g(v)} z^2 d\tau \\
&\geq V(t) - V(0)
\end{aligned}$$

where a sufficient condition for the inequality to hold is

$$\sigma_1 < 4 \frac{g(v)}{|v|} \tag{3.14}$$

□

Hence it is clear that the standard parametrization can be made passive by introducing a velocity dependency on σ_1 such that

$$\sigma_1(v) < 4 \frac{g(v)}{|v|}.$$

It is clear that a model with constant σ_1 might violate the sufficient condition (3.14) for passivity. Does this mean that the model is not passive under these conditions though? By simulation this shall be investigated. We start by regarding the integral expresson of the proof of property 3.3,

$$\int_0^t uy d\tau = \int_0^t \underbrace{\sigma_0 z\dot{z}}_{d_0} + \underbrace{\sigma_0^2 \frac{|v|}{g(v)} z^2}_{d_1} + \underbrace{\sigma_1 \dot{z}^2}_{d_2} + \underbrace{\sigma_0 \sigma_1 \frac{|v|}{g(v)} z\dot{z}}_{d_3} d\tau. \tag{3.15}$$

Note that the dimension of this integral is energy. The above integral can in the general case be divided into one part which can be expressed in the chosen storage function, and one part that can not, and that has to be positive for passivity to follow.

We have here four terms, d_0, which can be expressed in the chosen storage function V, and d_1, d_2, d_3 corresponding to power dissipation in the system. For physical reasons we want the power dissipation to be positive in the above notation. A positive power dissipation with the chosen storage function corresponds to the condition $d_1 + d_2 + d_3 \geq 0$. Indeed the term d_3 causes the

problem, since d_1 and d_2 are positive. Is there another choice of storage function that includes d_1, d_2 or d_3? Since the storage function shall be a function of the states only this is impossible in this case. However, assume that d_1 and d_2 could be expressed with a storage function. This makes the inequality even harder to fulfill since we now require $d_3 \geq 0$.

Since it is impossible to separate the dependency of the input v from d_1, d_2 and d_3, there exist no other storage function that better fulfills the passivity definition than $V(z) = \sigma_0 \frac{z^2}{2}$.

With this in mind we now turn to the simulation results. The friction model (3.4) with a velocity input $v(t) = A\text{sgn}(\sin(2\pi t))\sin(4\pi t)$, with $A = 0.0005$ and the parameters of table 3.2 has been simulated.

σ_0	σ_1	v_0	α_0	α_1	α_2
[N/m]	[Ns/m]	[m/s]	[N]	[N]	[Ns/m]
1	2	10	1	1	0

Table 3.2 Passivity simulation parameters.

See figure 3.4. The corresponding terms d_0, d_1, d_2 and d_3 has been plotted together with the sum $d_1 + d_2 + d_3$ in figure 3.5. It is seen that the sum $d_1 + d_2 + d_3$ is negative for some time intervals. Hence with corresponding choices of initial values, input signal and parameters the inequality in the passivity definition is shown not to hold.

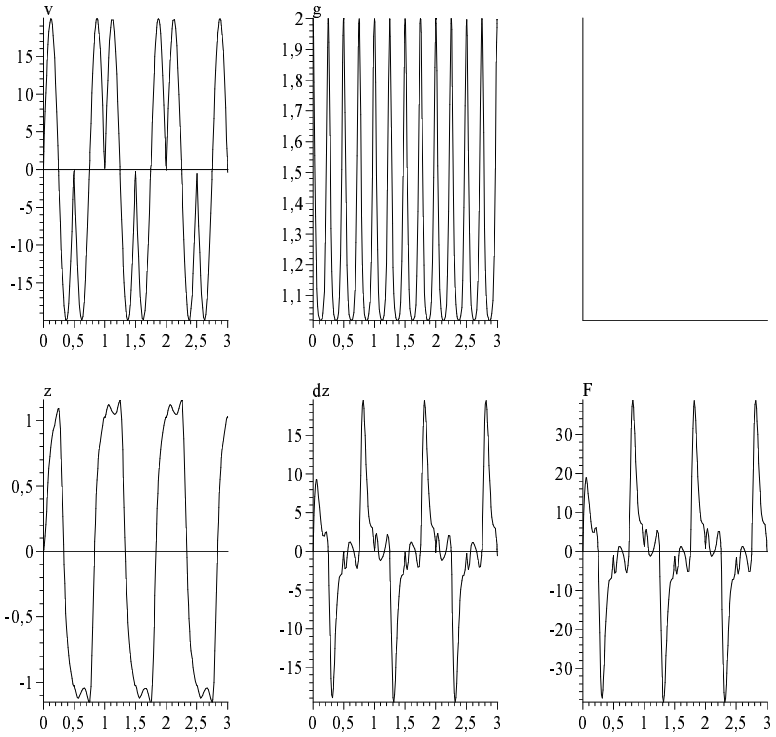

Figure 3.4 Simulation of standard parametrization of LuGre model for investigating passivity property. From upper left: input velocity v, $g(v)$, z, $\dot{z}$ and F

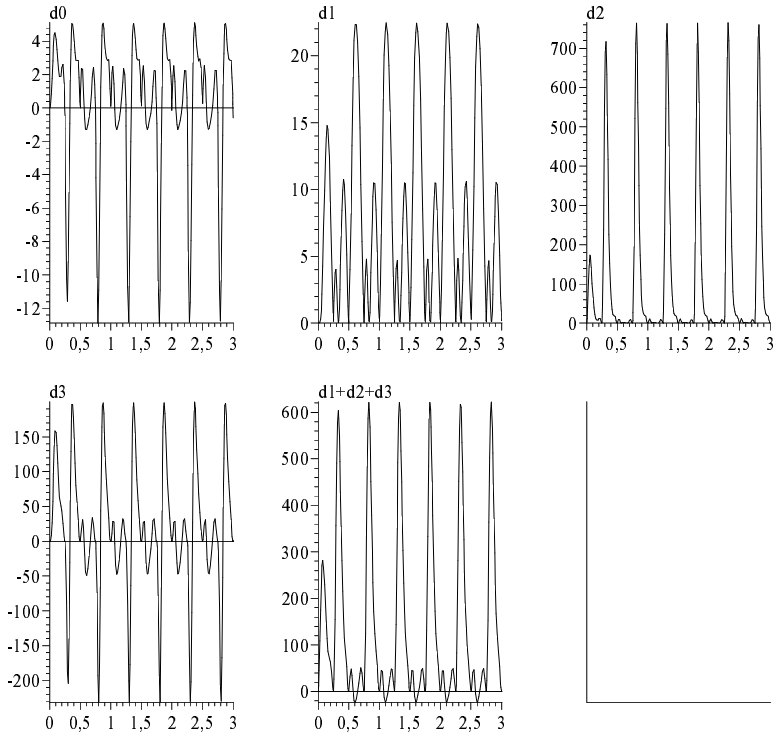

Figure 3.5 Simulation of standard parametrization of LuGre model for investigating passivity property. Storage and dissipation terms according to (3.15)

This, together with the claim that there exist no other choice of storage function for which the passivity definition holds better, show that the sufficiency of the acheived condition above is to be taken seriously.

Another approach to this problem of the standard parametrization is taken in the section on asymptotical stablility 3.5. The passivity problem arise only under some very special conditions, when the velocity changes very abruptly. The model has been shown to work properly for simulations as well as for friction compensation in spite of this sometimes non-physical behaviour.

Boundedness of the state variable z

From [11] we have the following important property

PROPERTY 3.4—BOUNDEDNESS OF z
Assume that $0 < g(v) \leq a$. If $\sigma_0|z(0)| < a$ then $\sigma_0|z(t)| < a, \forall t \geq 0$. □

This means that starting with bounded initial conditions on the state variable z according to this property we are guaranteed to have bounded z for all times t. This implies that the reachable state space of (3.17) then is (a subspace of)

$$R = \{x = \begin{bmatrix} v & z \end{bmatrix}^T | v \in \mathbb{R}, z < \frac{\alpha_0 + \alpha_1}{\sigma_0}\}. \tag{3.16}$$

3.5 Properties of the physical system $u \mapsto F$

Since the model (3.4) has been found to not fullfill the conditions for passivity at all time it might be interesting to further investigate it's stability properties

while connected to a physical system. We want to show that the problem with passivity does not imply any problems with stability, although the system might "create" energy under certain conditions. Moreover we want to show that the friction model gives a system with the physical property of coming to rest when no external forces are applied.

We shall regard a simple mass-force system, where the mass is under influence of friction according to (3.4). See figure 3.6.

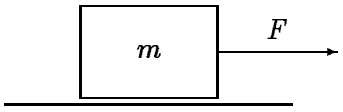

Figure 3.6 Physical system, mass with friction and applied force.

We choose as output the mass velocity (position would not be a good choice since we are not interested in knowing if the mass will return to a certain position). This defines an origin which corresponds to rest. The system is

$$m\ddot{x} = u - F.$$

This system is nonlinear of second order with

$$\begin{cases} \dot{v} &= -\frac{1}{m}F + \frac{1}{m}u \\ \dot{z} &= v - \sigma_0 \frac{|v|}{g(v)} z \\ g(v) &= \alpha_0 + \alpha_1 e^{-(v/v_s)^2} \\ F &= \sigma_0 z + \sigma_1 \dot{z} + \alpha_2 v \end{cases}$$

or

$$\begin{cases} \dot{v} &= -\frac{1}{m}(\sigma_1 + \alpha_2)v + \frac{\sigma_0\sigma_1}{m}\frac{|v|}{g(v)}z - \frac{\sigma_0}{m}z + \frac{1}{m}u \\ \dot{z} &= v - \sigma_0 \frac{|v|}{g(v)} z \\ y &= v \end{cases} \tag{3.17}$$

This is a second order non-linear dynamical system of the general form

$$\begin{cases} \dot{x} &= f(x,u) \\ y &= h(x,u) \end{cases} \tag{3.18}$$

with $x = \begin{bmatrix} v & z \end{bmatrix}^T$. In a more general case where the friction parameters are allowed to vary with time, e.g. due to varying normal load, f and h in (3.18) becomes dependent of t.

Input-output stability

The natural way to examine BIBO stability (definition B.2) of interconnected nonlinear dynamical systems is to apply the *small gain theorem* (theorem B.1), which yields

PROPERTY 3.5—BIBO STABILITY
The system (3.17) is BIBO-stable with the gains of the linear part and the nonlinear friction respectively equal to

$$\begin{aligned} \gamma_1 &= \int h(t)dt \\ \gamma_2 &= \sigma_1 \left(1 + \frac{\alpha_0 + \alpha_1}{\alpha_0}\right) + \alpha_2 \end{aligned}$$

if $\gamma_1\gamma_2 < 1$. □

Proof. Designate by H_1 the mass and by H_2 the friction model. For the small gain theorem to apply we need to show that there exist a finite gain γ and a constant β that satisfies (B.1) for (3.4). H_1 is a linear system and thus has a gain $\gamma_1 = \int h_1(\tau)d\tau$, where $h_1(t)$ is the impulse response of the system. We have

$$\begin{aligned}
\|F\| &= \|\sigma_0 z + \sigma_1 \dot{z}\| + \alpha_2 v \\
&\leq \sigma_0\|z\| + \sigma_1\|\dot{z}\| + \alpha_2\|v\| \\
&= \sigma_0\|z\| + \sigma_1\|v - \sigma_0\frac{|v|}{g(v)}z\| + \alpha_2\|v\| \\
&\leq \sigma_0\|z\| + \sigma_1\|v\| + \frac{\sigma_0\sigma_1}{g(v)}\|z\|\|v\| + \alpha_2\|v\| \\
&= \sigma_0\|z\| + (\sigma_1 + \frac{\sigma_0\sigma_1}{g(v)}\|z\| + \alpha_2)\|v\| \\
&\leq \alpha_0 + \alpha_1 + (\sigma_1 + \sigma_1\frac{\alpha_0 + \alpha_1}{\alpha_0} + \alpha_2)\|v\|
\end{aligned}$$

In the last inequality we have used the boundedness of $g(v)$ and the boundedness of z, property 3.4. Thus

$$\begin{aligned}
\beta_2 &= \alpha_0 + \alpha_1 \\
\gamma_2 &= \sigma_1\left(1 + \frac{\alpha_0 + \alpha_1}{\alpha_0}\right) + \alpha_2
\end{aligned}$$

□

This requires that σ_1 is small enough. The number of inequalities in the derivation gives us a hint that the result may be rather conservative though. It does not however give any information on stability of particular solutions, and therefore we go on with investigating Lyapunov stability of the system.

Asymptotical stability

In this section we regard the autonomous system

$$\dot{\boldsymbol{x}} = \boldsymbol{f}(t, \boldsymbol{x}, 0). \tag{3.19}$$

For this system we state

PROPERTY 3.6—ASYMPTOTICAL STABILITY
The equilibrium point $\boldsymbol{x} = 0$ of the system (3.17) with $u \equiv 0$ is asymptotically stable for all initial conditions $\boldsymbol{x}_0 \in R$. □

Proof. It follows trivially from (3.17) that $\boldsymbol{x} = 0$ is an equilibrium point.

Assume the Lyapunov function candidate

$$V(\boldsymbol{x}) = \frac{mv^2}{2} + \frac{\sigma_0 z^2}{2} \tag{3.20}$$

for which we have $V(0) = 0$, $V(\boldsymbol{x}) > 0, \boldsymbol{x} \in \mathbb{R} - \{0\}$. It remains to show negative semidefiniteness for $\dot{V}(\boldsymbol{x})$.

We have

$$\begin{aligned}\dot{V}(\boldsymbol{x}) &= mv\dot{v} + \sigma_0 z\dot{z} \\ &= mv\left\{-\frac{1}{m}(\sigma_1+\alpha_2)v - \frac{\sigma_0}{m}z + \frac{\sigma_0\sigma_1}{m}\frac{|v|}{g(v)}z\right\} + \sigma_0 z(v - \sigma_0\frac{|v|}{g(v)}z) \\ &= -(\sigma_1+\alpha_2)v^2 - \sigma_0 vz + \sigma_0\sigma_1\frac{v|v|}{g(v)}z + \sigma_0 vz - \sigma_0^2\frac{|v|}{g(v)}z^2 \\ &= -(\sigma_1+\alpha_2)v^2 + \sigma_0\sigma_1\frac{v|v|}{g(v)}z - \sigma_0^2\frac{|v|}{g(v)}z^2\end{aligned}$$

We can see directly from the above expression that there exists at least one set of points in the state space for which $\dot{V}(\boldsymbol{x}) \geq 0$, namely $\{\boldsymbol{x}|v=0\}$. Therefore it does not suffice to use theorem B.2, instead we turn to the results of invariant sets analysis to show that stability still follows. See [19, LaSalle's principle] for an introduction to this framework.

In the following we will refer to the following form of $\dot{V}(\boldsymbol{x})$:

$$\dot{V}(\boldsymbol{x}) = -(\sigma_1+\alpha_2)v^2 + \sigma_0\sigma_1\frac{v|v|}{g(v)}z - \sigma_0^2\frac{|v|}{g(v)}z^2. \tag{3.21}$$

To get an idea of how $\dot{V}(\boldsymbol{x})$ looks we examine the level curves $\dot{V}(\boldsymbol{x}) = 0$. Expression (3.21) equal to zero gives

$$v\left(\frac{\sigma_1+\alpha_2}{\sigma_0^2}g(v)v + \frac{\sigma_1}{\sigma_0}vz - z^2\right) = 0.$$

Thus

$$\begin{cases} v &= 0, \text{or} \\ \frac{\sigma_1+\alpha_2}{\sigma_0^2}g(v)v + \frac{\sigma_1}{\sigma_0}vz - z^2 &= 0. \end{cases} \tag{3.22}$$

We start by examining the line $v = 0$, which is surrounded by a set of points for which $\dot{V}(\boldsymbol{x}) < 0$. Setting $v = 0$, $u \equiv 0$ in (3.17) however gives

$$\begin{cases} \dot{v} &= -\frac{\sigma_0}{m}z \\ \dot{z} &= 0 \end{cases}$$

why no solutions can stay on this line unless $z = 0$. Thus the origin is the smallest invariant set and this line causes no stability problems according to LaSalle's invariant principle.

We now carry on with the second domain of $\dot{V}(\boldsymbol{x})$ which can cause problems. This domain is defined by (3.22), and in this domain we have $\dot{V}(\boldsymbol{x}) > 0$. From (3.21) we can see that there can be a problem with negative semidefiniteness only when v and z have equal signs, and that $\dot{V}(\boldsymbol{x})$ is symmetric regarding signs. Therefore it is enough to regard the case $v > 0$, $z > 0$, which will be assumed below.

We have

$$z^2 - \frac{\sigma_0}{\sigma_1}vz + \frac{\sigma_1+\alpha_2}{\sigma_0^2}g(v)v = 0$$

giving

$$z = \frac{\sigma_1 v \pm \sqrt{\sigma_1^2 v^2 - 4(\sigma_1+\alpha_2)g(v)v}}{2\sigma_0} \tag{3.23}$$

and real solutions for

$$\sigma_1^2 v^2 \geq 4(\sigma_1 + \alpha_2) g(v) v. \tag{3.24}$$

The solution (3.23) with negative sign gives

$$z_- = \frac{2(\sigma_1 + \alpha_2) g(v) v}{\sigma_0 (\sigma_1 v + \sqrt{\sigma_1^2 v^2 - 4(\sigma_1 + \alpha_2) g(v) v})} \tag{3.25}$$

Now regard the system with initial conditions $x_0 \in R \cap \{x | \dot{V}(x) > 0\}$. That is

$$\begin{aligned}
|z| &< \frac{\alpha_0 + \alpha_1}{\sigma_0}, \text{ from the definition of } R, \\
|z| &> z_- = \frac{2(\sigma_1 + \alpha_2) g(v) v}{\sigma_0 (\sigma_1 v + \sqrt{\sigma_1^2 v^2 - 4(\sigma_1 + \alpha_2) g(v) v})}, \\
&\quad \text{necessary condition for } \dot{V}(x) > 0, \\
\frac{v}{g(v)} &> \frac{4}{\sigma_1} \left(1 + \frac{\alpha_2}{\sigma_1}\right) \text{ necessary condition for } \dot{V}(x) > 0 \text{ from (3.24).}
\end{aligned}$$

Equation (3.17) with the above given constraints inserted gives

$$\begin{aligned}
\dot{z} &= v - \sigma_0 \frac{|v|}{g(v)} z \\
&< v - \sigma_0 \frac{|v|}{g(v)} \frac{2(\sigma_1 + \alpha_2) g(v) v}{\sigma_0 (\sigma_1 v + \sqrt{\sigma_1^2 v^2 - 4(\sigma_1 + \alpha_2) g(v) v})} \\
&= \left(1 - \frac{2(\sigma_1 + \alpha_2) v}{\sigma_1 v + \sqrt{\sigma_1^2 v^2 - 4(\sigma_1 + \alpha_2) g(v) v}}\right) v \\
&= \frac{-\sigma_1 v + \sqrt{\sigma_1^2 v^2 - 4(\sigma_1 + \alpha_2) g(v) v} - 2\alpha_2 v}{\sigma_1 v + \sqrt{\sigma_1^2 v^2 - 4(\sigma_1 + \alpha_2) g(v) v}} v < 0
\end{aligned}$$

since

$$\sigma_1 v > \sqrt{\sigma_1^2 v^2 - 4(\sigma_1 + \alpha_2) g(v) v} \iff \sigma_1^2 v^2 > \sigma_1^2 v^2 - 4(\sigma_1 + \alpha_2) g(v) v.$$

Thus no solutions can stay in this domain since z will decrease until the system trajectory has reached the region for which $\dot{V}(x) < 0$. That is $\{x | \dot{V}(x) > 0\}$ is not an invariant set. This completes the proof of asymptotical stability. □

Remark 1. Note that the form

$$\dot{V}(x) = -\left(\sigma_1 + \alpha_2 - \sigma_0 \sigma_1 \frac{\operatorname{sgn}(v)}{g(v)} z\right) v^2 - \sigma_0^2 \frac{|v|}{g(v)} z^2$$

of (3.21) gives a sufficient condition for negative semidefiniteness

$$|z| < \frac{g(v)}{\sigma_0} (1 + \frac{\alpha_2}{\sigma_1}),$$

and that the fullfillment of this condition does *not* follow from property 3.4.

σ_0	σ_1	v_0	α_0	α_1	α_2
[N/m]	[Ns/m]	[m/s]	[N]	[N]	[Ns/m]
260	1.2	0.1	0.279	0.0389	0.0177

Table 3.3 Lugre parameters identified from a real system.

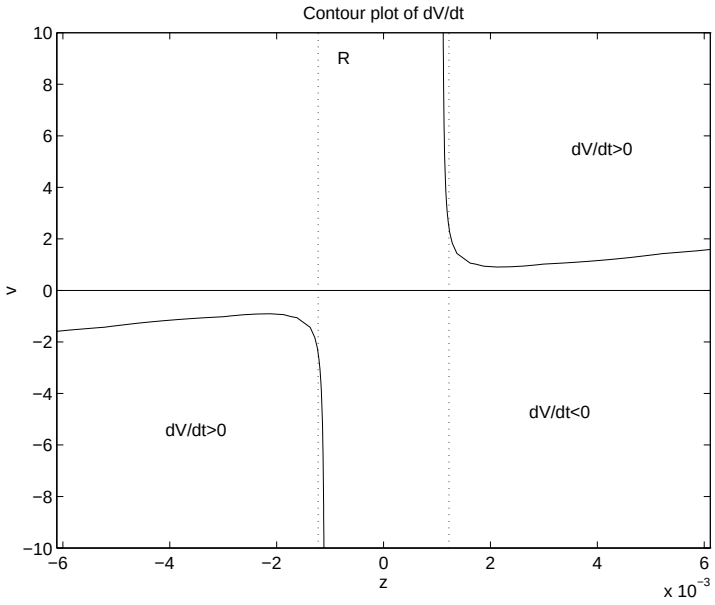

Figure 3.7 The level curves $\dot{V}(x) = 0$ (solid lines), and the set R (dotted lines).

A plot of the level curves $\dot{V}(x) = 0$ for the parameters of table 3.3 is shown in figure 3.7 together with the set R.

It is clear that an intersection exists between R and $\{x|\dot{V}(x) > 0\}$, i.e. that property 3.4 cannot guarantee negative semidefiniteness of $\dot{V}(x)$.

Remark 2. The inequality (3.24) means that there exists a lowest velocity for which $\dot{V}(x) > 0$ given a constant σ_1 and a bounded $g(v)$.

Remark 3. The condition (3.24) can be written as

$$\sigma_1 \geq 4\frac{g(v)}{v}(1 + \frac{\alpha_2}{\sigma_1}),$$

which can be compared with the sufficient condition for passivity (3.4).

Remark 4. The solution (3.23) with positive sign

$$z_+ = \frac{\sigma_1 v + \sqrt{\sigma_1^2 v^2 - 4(\sigma_1 + \alpha_2)g(v)v}}{2\sigma_0} \to \infty \text{ as } v \to \infty,$$

and the solution (3.25) with negative sign

$$\begin{aligned} z_- &= \frac{\sigma_1^2 v^2 - \sigma_1^2 v^2 + 4(\sigma_1 + \alpha_2)g(v)v}{2\sigma_0(\sigma_1 v + \sqrt{\sigma_1^2 v^2 - 4(\sigma_1 + \alpha_2)g(v)v})} \\ &= \frac{2(\sigma_1 + \alpha_2)g(v)}{\sigma_0(\sigma_1 + \sqrt{\sigma_1^2 - 4(\sigma_1 + \alpha_2)\frac{g(v)}{v}})} \end{aligned}$$

$$\rightarrow \quad \frac{(\sigma_1+\alpha_2)\alpha_0}{\sigma_0\sigma_1}$$
$$= \quad \frac{\alpha_0}{\sigma_0}\left(1+\frac{\alpha_2}{\sigma_1}\right) \text{ as } v \rightarrow \infty,$$

which can be seen from figure 3.7.

From the above equation and property 3.4 we get a sufficient condition for a non-empty intersection between R and $\{\boldsymbol{x}|\dot{V}(\boldsymbol{x}) > 0\}$.

PROPERTY 3.7

$$\frac{\alpha_0}{\sigma_0}\left(1+\frac{\alpha_2}{\sigma_1}\right) < \frac{\alpha_0+\alpha_1}{\sigma_0} \Longrightarrow R \cap \{\boldsymbol{x}|\dot{V}(\boldsymbol{x}) > 0\} \neq \emptyset$$

□

Actually the proof of property 3.6 gives global asymptotical stability since it has been shown that all solutions starting in $\{\boldsymbol{x}|\dot{V}(\boldsymbol{x}) > 0\}$ will leave this region. This is not so important though, since all trajectories starting in R will remain in R. Anyway we have

PROPERTY 3.8—GLOBAL ASYMPTOTICAL STABILITY
The equilibrium point $\boldsymbol{x} = 0$ of the system (3.17) with $\boldsymbol{u} \equiv 0$ is globally asymptotically stable. □

What happens with unforced trajectories starting in the intersection $R \cap \{\boldsymbol{x}|\dot{V}(\boldsymbol{x}) > 0\}$? Obviously the Lyapunov function will at least initially increase along the solution. This is verified by simulation, see figure 3.8. For comparison a simulation with initial conditions close to the former, but outside $R \cap \{\boldsymbol{x}|\dot{V}(\boldsymbol{x}) > 0\}$ has also been done. See figure 3.9. The Lyapunov function has the intuitive interpretation as system energy potential as kinetic energy stored in the state v, and spring potential energy store in the state z. If $V(\boldsymbol{x})$ is the complete description of the system energy the increase of $V(\boldsymbol{x})$ along unforced trajectories means that the system produces energy. In the simulation of figure 3.8 the system energy is computed from

$$W = \int_0^t Fv d\tau. \tag{3.26}$$

The result shows that indeed the model produces energy initially. A strongly non-physical behaviour in other words. No stability problems are shown by the simulations though, as expected.

$R \cap \{\boldsymbol{x}|\dot{V}(\boldsymbol{x}) > 0\} \neq \emptyset$ gives a non-physical behaviour. This is probably the same property that gives the problems with passivity. Also here the problem is fixed by introducing a velocity dependece on σ_1, see (3.24), having the effect of removing the real solutions of (3.23). The conditions for which the state trajectories enter this region are rather special though. There is needed a combination of large v and large z for this to happen, but for increasing velocities v the state z tends to decrease. It therefore is required that the system is given an firm impuls from a slow steady state motion to enter this region.

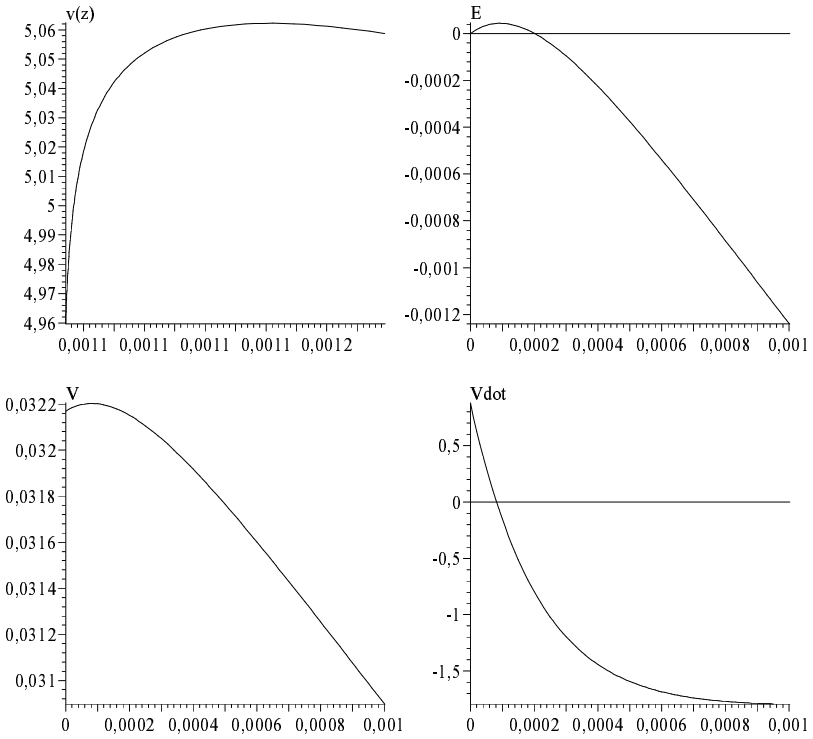

Figure 3.8 Simulation with $\dot{V}(x) > 0$. Initial values taken from figure 3.7 inside the intersection $R \cap \{x | \dot{V}(x) > 0\}$ with $v = 5.0587$, $z = 0.001179$. From upper left: phase portrait, energy computed from (3.26) with initial energy defined as zero, Lyapunov function V and $\dot{V}$.

3.6 Velocity dependent damping σ_1

It has been shown that a velocity dependent σ_1 solves some mathematical difficulties with passivity and stability. In applications these difficulties have not implied any problems however. Is it rational to complicate the model by introducing a velocity dependent σ_1 if in practice there will be no difference?

The following two velocity dependent σ_1 have been proposed and investigated in [22]:

$$\sigma_1(v) = \sigma_1 e^{-(v/v_d)} \tag{3.27}$$

and

$$\sigma_1(v) = \frac{\sigma_1}{v}. \tag{3.28}$$

(3.27) introduces an additional parameter v_d. How shall this be identified? The identification procedure is non-trivial even with the six parameters of the standard model. (3.28) requires reformulation of the model which hides the nice and simple physical interpretation.

Physically it seems motivated to use velocity dependent damping. There is no reason for the damping to be linear throughout the whole velocity range. Different physical situations are found at low velocities and high velocities. Rather it seems rational to use different dampings at different velocities. This is also supported by simulations compared with experimental results. E.g. it is shown in [22] that (3.27) gives a better model of frictional lag than the standard model (3.4).

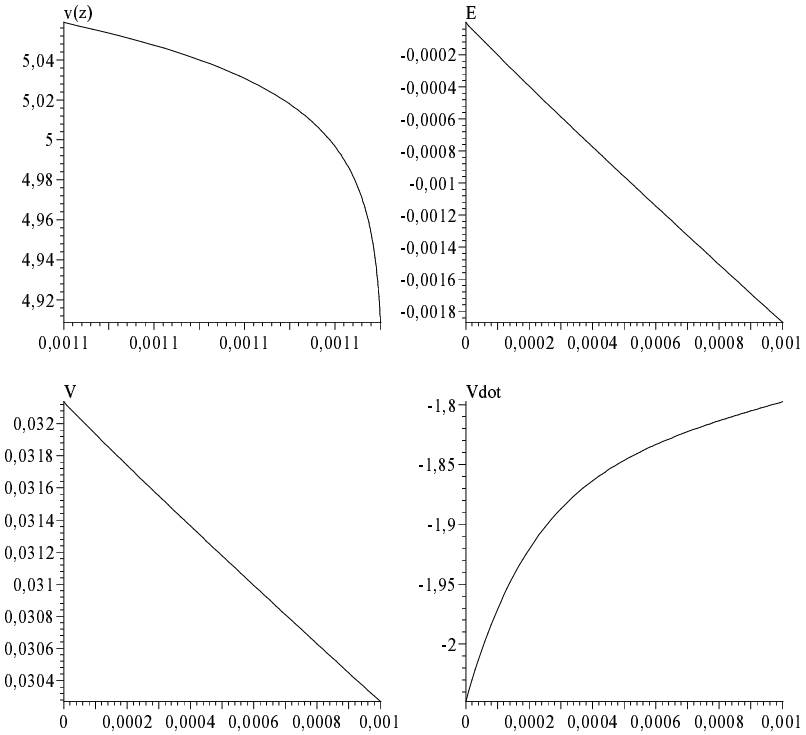

Figure 3.9 Simulation with $\dot{V}(x) < 0$. Initial values taken from figure 3.7 outside the intersection $R \cap \{x|\dot{V}(x) > 0\}$ with $v = 5.0587$, $z = 0.001066$. From upper left: phase portrait, energy computed from (3.26) with initial energy defined as zero, Lyapunov function V and $\dot{V}$.

It is another question if a velocity dependent σ_1 gives significantly better friction compensation. If not there is no reason to abandon the standard model (3.4).

3.7 Asymmetric friction

In real systems the friction characteristics are often dependent on the sign of the velocity. There is no problem with introducing such a dependency in the Lugre model. When an asymmetric model is used the static parameters will be refered to as α_0^+, α_0^-, α_1^+, α_1^-, v_0^+, v_0^- with the upper index corresponding to the sign of the velocity.

Remark 1. In [22] it is noted that the asymmetric parametrization gives a discontinuous function $g(v)$, but that the right hand side of the first equation of (3.4) still is continuous at zero velocity.

For the dynamic parameters the dependency is not due to the sign of the velocity, but to the sign of z. This can be understood by regarding the linearized equations (3.10). For small displacements which give a negative sign of the spring like friction force the spring constant σ_0 and the damping σ_1 are fixed, though the velocity changes sign in the motion. Motions in the other direction might have other spring characteristics, and other values of the dynamic parameters are then valid.

For σ_0 this is straightforward, though the parameter is discontinuous the

equations (3.4) and (3.10) still are continuous. A discontinuous σ_1 with respect to sgn(z) will give a discontinuous friction force both in (3.4) and (3.10) though, why this parametrization should be avoided. It would be possible to make σ_1 depend on sgn(v) with maintained continuity of the equations. The physical interpretation of this is somewhat doubtful though, why it may be better to leave this parameter symmetric.

The dynamic parameters in an asymmetric model will be refered to as $\sigma_0^+, \sigma_0^-, \sigma_1^+, \sigma_1^-$, with the upper index corresponding to the sign of z and the sign of v respectively.

Remark 1. A model that is asymmetric with respect to the dynamic parameters impose a challenge to integration routines. If the integration is not very accurate around $z = 0$, small jumps in z might introduce large peaks in the $\sigma_1 \dot{z}$ term. Pay attention! Even though real systems may show asymmetry in dynamic parameters in identification, it might be better to use a symmetric average in simulations.

3.8 Identification

In [26, 10] an identification procedure on the model of figure C.2 based on four steps, each involving an experiment, a model reduction and a least squares identification, is presented. Because of practical reasons this procedure has not been used here, but instead a simplified procedure based on other experiments has been carried out. In the procedure used here the inertia J is considered known apriori. See [18] for an overview as well as in-depth discussions on system identification in general. Application of the procedure presented here will be carried out in chapter 4.

The procedure presented here is expected to give reasonable parameter values, at least for the static parameters. Optimization of all estimates is not carried out.The procedure can however easily be changed to give least squares estimates if wanted. Refinements of the procedure is not within the scope of this work, and as the emphasis of the work lies on qualitative comparisons rather than quantitative, approximate parameter values are sufficient.

The procedure is based on the following equation

$$J\ddot{\theta} = u - \alpha_2\dot{\theta} - \tau, \tag{3.29}$$

where u is applied external torque, $\alpha_2\dot{\theta}$ is the linear viscous part of the friction torque, and τ is the friction force given by 3.4 (except for the viscous friction which is treated separately in this context).

The identification procedure is divided into four steps which will each be described in a subsection below.

1. Identification of viscous friction coefficient α_2 and the coulomb friction α_0.

2. Identification of α_1.

3. Identification of dynamic parameters σ_0 and σ_1.

4. Identification of Stribeck velocity v_0.

Step 1, $\longrightarrow \alpha_0, \alpha_2$

α_2, α_0 are identified from the steady state friction relation

$$F_{ss} = g(v_{ss})\text{sgn}(v_{ss}) + \alpha_2 v_{ss}.$$

For $v_{ss} > v_0$ $g(v_{ss}) = \alpha_0$ giving

$$F_{ss} = \alpha_0 \text{sgn}(v_{ss}) + \alpha_2 v_{ss}. \tag{3.30}$$

An estimate of the viscous friction can thus be taken the slope of the Stribeck curve for $v_{ss} > v_0$, whereas the Coulomb friction α_0 will be found at the intersection of the extrapolated extension of this line with $v_{ss} = 0$.

Step 2, $\longrightarrow \alpha_1$

In the chapter on limit cycles it is noted that the control signal amplitude in any limit cycle is equal to the break-away torque τ_B. Neglecting the rate dependency of τ_B torque predicted by the Lugre model (limit cycles often are slow in this sense, why the maximum break-away torque is expected to be found), and assuming that the $\tau_B = \alpha_0 + \alpha_1$, it is possible to estimate α_1 by $\alpha_1 = \tau_B - \alpha_0$, α_0 being given by the preceding step. τ_B can easily be found by introducing a limit cycle in the system and measure the amplitude of the control signal.

Step 3, $\longrightarrow \sigma_0, \sigma_1$

Equation (3.10)and (3.13) gives expressions possible to use for identification of the dynamic parameters. Rewriting (3.10) as

$$F = \sigma_0 x + \sigma_1 v \tag{3.31}$$

noting that $z(t) = x(t)$ if $z(0) = x(0) = 0$ we get an expression well suited for identification. This means that $x = 0$ corresponds to the steady state position where the friction force is zero. Very small motions in stiction regime near $x = 0$ means that this linearized equation can be used as a regression model for (least squares) identification if F, x and v are known.

Remark 1. This identification is very difficult to carry out since it is experimentally very difficult to measure the regressors F, x and v. The other identification procedure refered to also has problems with identifying the dynamical parameters. In fact only σ_0 is identified, whereas σ_1 is chosen to give well damped linearized equations.

Step 4, $\longrightarrow v_0$

The Stribeck velocity can be found in the Stribeck curve by identifying the region where the steady-state friction increases with decreasing steady state velocity. This region is however found at such low velocities that it becomes experimentally very difficult to maintain the velocity without stick-slip motion. Another approach will be therefore be used. In the Lugre model v_0 defines when a decrease of the friction force shall be present in the motion from stick to slip. As a result, by starting in stick, and then ramp up an externally applied force until slip is reached, and during this record velocity and friction torque, it is possible to plot friction torque τ versus velocity $\dot{\theta}$ and graphically identify v_0. v_0 will then correspond to the point where the friction force is $\alpha_0 + \alpha_1/2$, i.e.

the friction force has made half the drop from the break-away force to the kinetic friction force.

The graphical approach may not seem to be very rigorous, but will anyway give an estimate within the correct range. Of course it would be possible to use an iterative optimization procedure together with simulations to find an optimal value.

3.9 Modeled friction phenomena

As for the Bliman & Sorine model stiction and pre-sliding displacement are modeled. The Lugre model rate-dependency also models varying break-away force. While the Bliman & Sorine model only reproduces a transient Stribeck effect different from the one described in 1.2, the Lugre model exhibits a steady state Stribeck effect. While the Bliman & Sorine model because of the dependency on absolute relative displacement only, impossibly can model a phenomenon as frictional lag, the Lugre model correctly seems to reproduce this phenomenon. The reason for this is that the coefficient of (3.6) can vary with velocity.

3.10 Simulations

In this section we illustrate the properties of the Lugre model by doing some simulations. See the corresponding section of the chapter on the Bliman & Sorine model for comparisons and comments on the choices of parameters.

Integration of the model

The problems with break-away force depending on initial conditions found for the Bliman & Sorine model are not found for the Lugre model. This is due to the Lugre model being a single state model, and the problems were due to the fact that two states were "out of phase". In the Lugre model the bounding systems always have the same maximum values, but the location may vary with initial conditions. The break-away force thus is not dependent on initial conditions, but still is rate-dependent. The pre-sliding displacement is dependent on initial conditions though, as for the Bliman & Sorine model.

The problems with oscillatory behaviour in interconnection with a mass system is not found either. From (3.12) it is clear that the linearized damping is controlled with the parameter σ_1, which then can be chosen to give good damping.

Free model

In figures 3.10 and 3.11 we see the response of the free Lugre model to a sinusoidal input velocity. The main diffrences from the corresponding Bliman & Sorine simulations are that we now do not have a problem with initial conditions affecting first break-away, and that there are peaks in friction force also at the transition from slip to stick.

Figure 3.12 shows what happens if we change the rate of the sinusoidal input torque. Two simulations are plotted, and the rate dependency of the friction is clearly seen.

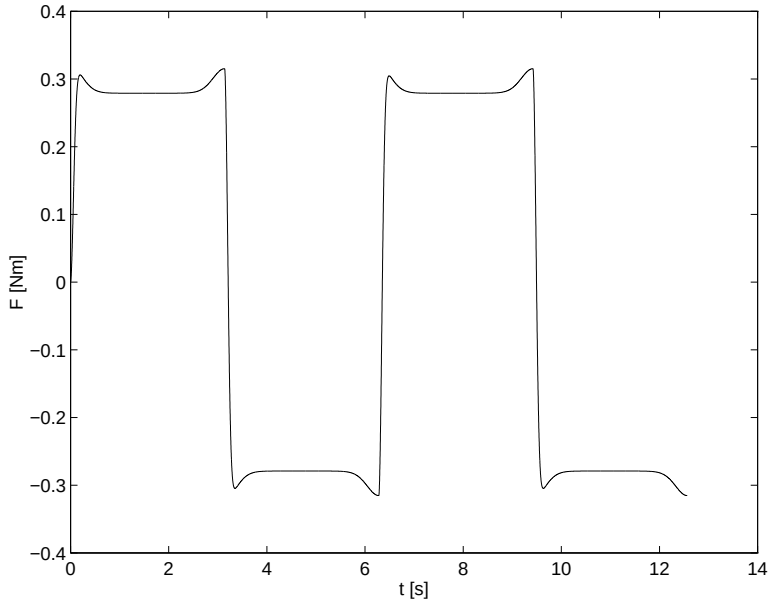

Figure 3.10 Simulation of free Lugre model with sinusoidal input velocity. Friction force versus time.

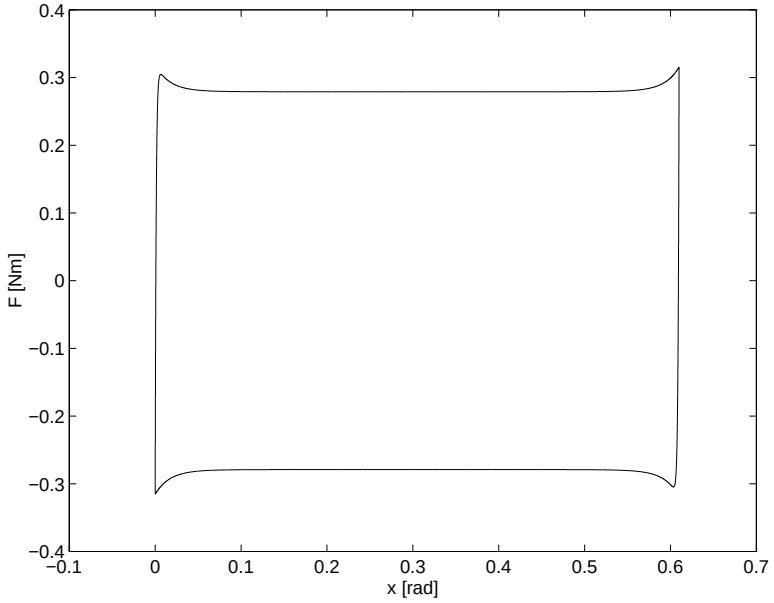

Figure 3.11 Simulation of free Lugre model with sinusoidal input velocity. Friction force versus displacement.

Interconnected model

The simulated system is the same inertial system used for the Bliman & Sorine model simulations earlier. This time with Lugre friction. The Lugre parameters are

$$\begin{bmatrix} \sigma_0 & \sigma_1 & v_0 & \alpha_0 & \alpha_1 & \alpha_2 \end{bmatrix} = \begin{bmatrix} 260 & 1.2 & 0.1 & 0.279 & 0.0389 & 0 \end{bmatrix}.$$

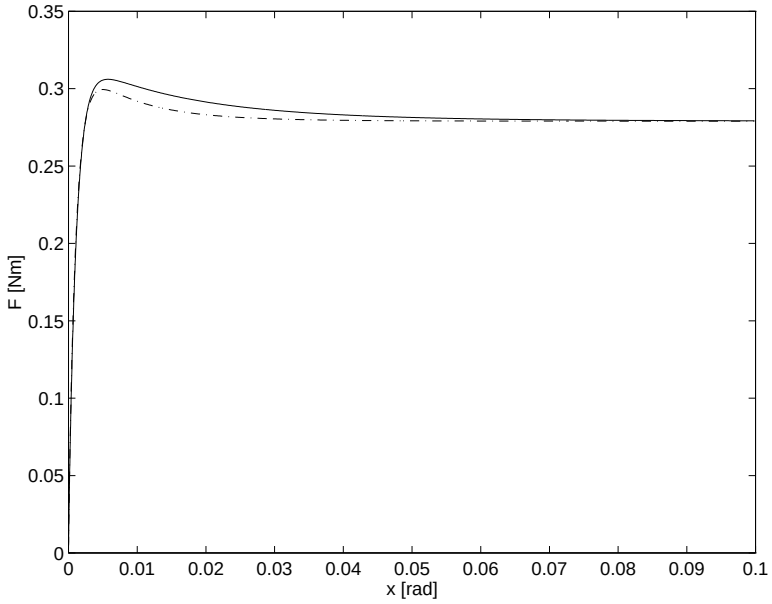

Figure 3.12 Simulation of free Lugre model with sinusoidal input velocities of different rates. Friction force versus time. Solid: Slower input rate. Dash-dotted: Higher input rate.

In figure 3.2 we see the response to an external force $u = a\sin(\omega t)$ with $a = 0.32$ Nm and $\omega = 1$ rad/s. The responce is shown in figure 3.13. Note that although we have no viscous friction we have a well damped behaviour in stiction regime. The parameter σ_1 allows us to determine stiction damping independently of viscous friction. Moreover we see that the Lugre model exhibits a peak in the friction torque also at the transition from slip to stick, in contrast to the Bliman & Sorine model.

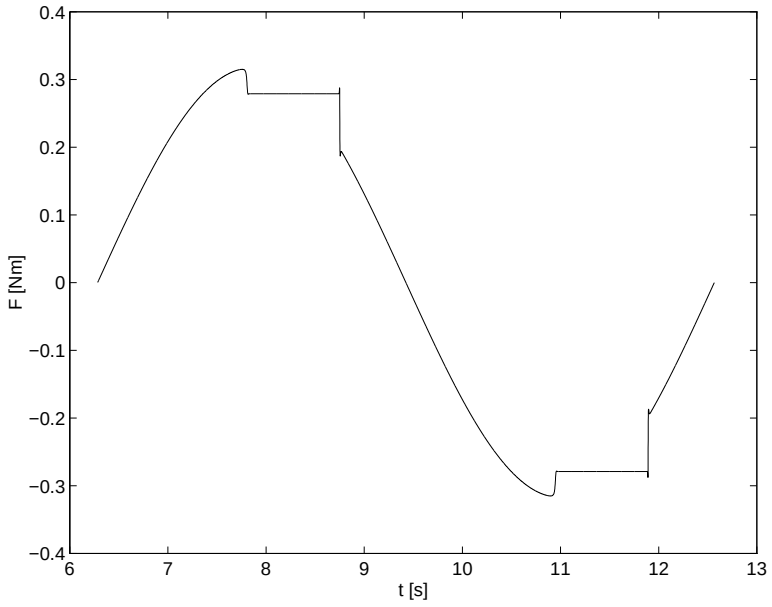

Figure 3.13 Simulation of simple inertial system with Lugre friction and sinusoidal input torque. Zero viscous friction. Friction force versus time.

A case with non-zero viscous friction ,$\alpha_2 = 0.0177$ Nms/rad, is also simulated and shown in figure 3.14.

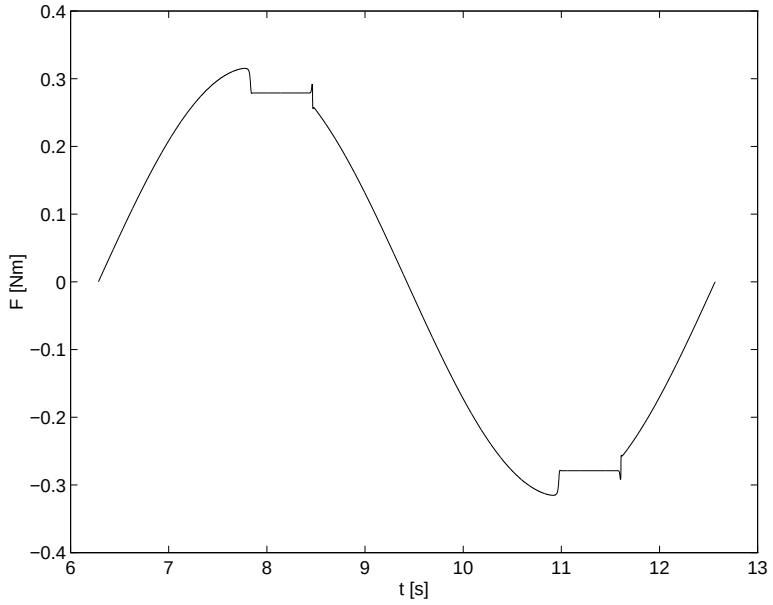

Figure 3.14 Simulation of simple inertial system with Lugre friction and sinusoidal input torque. Non-zero viscous friction. Friction force versus time.

The rate dependency of the Lugre model responce is illustrated in figure 3.15, where the break-away region of the simulation is shown in zoom together with a new simulation with $\omega = 5$ rad/s. We see that the break-away torque is less in the latter case.

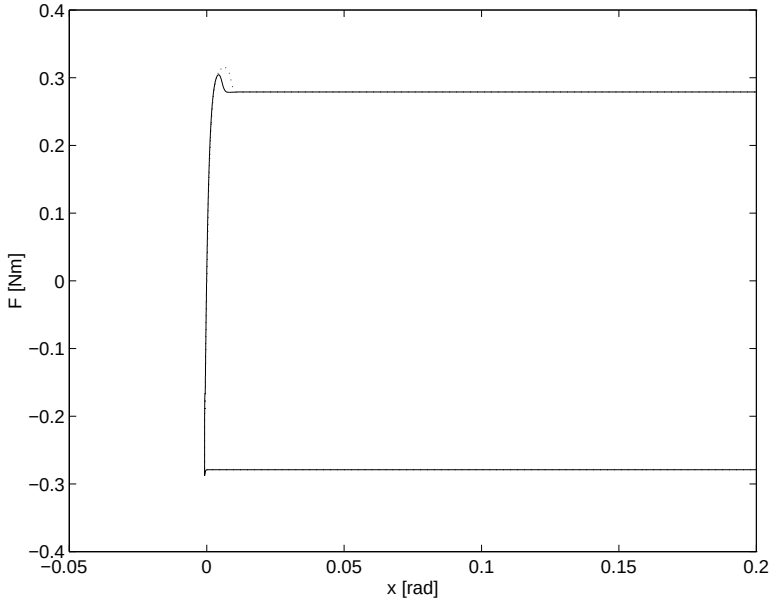

Figure 3.15 Simulations of simple inertial system with Lugre friction and sinusoidal input torques with different rates. Non-zero viscous friction.Friction force versus displacement. Solid: Higher input rate. Dotted: Lower input rate.

Just to illustrate the influence of the damping parameter σ_1 we show a simulation where this parameter is set to zero. The result is shown in figure 3.16 as a plot of friction force versus time. We get a oscillatory behaviour similar to that of the Bliman & Sorine model. The conclusion is that the damping term $\sigma_1 \dot{z}$ is essential to acheive good behaviour at sign changes of velocity, while maintaining freedom in the choices of large velocity properties such as viscous friction.

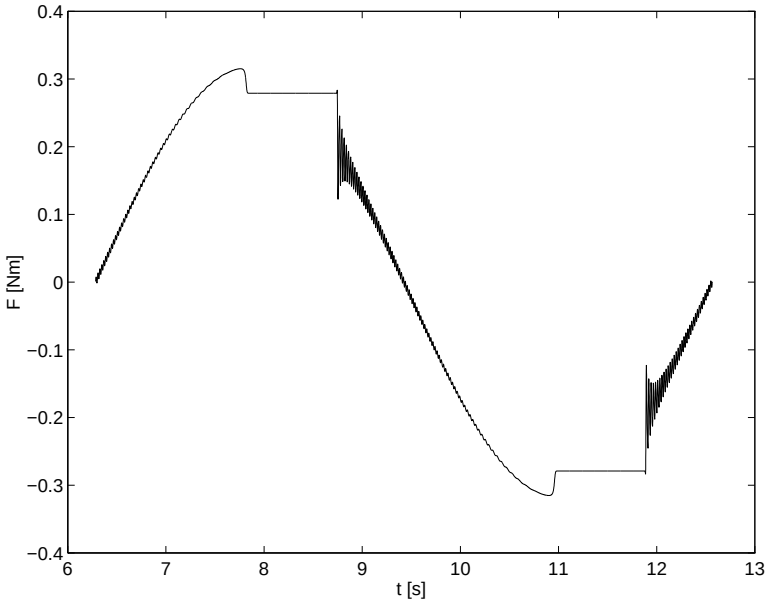

Figure 3.16 Simulations of simple inertial system with Lugre friction and sinusoidal input torques with different rates. Zero viscous friction. Zero stiction damping σ_1. Friction force versus displacement.

Small displacements

For small displacements the Lugre model is expected to behave like a linear spring. To verify this behaviour we simulate a mass with Lugre friction and external force $u = B + A\sin(\omega t)$. In figure 3.17 uni-directional input torques of different magnitudes are applied. We see that for small input torques we have an almost linear behaviour, while for larger torques the response becomes non-linear and shows hysteresis. We see that uni-directional input torques do not take the system back to the initial position. In figure 3.18 symmetric bi-directional input torques with zero mean are used, and now the system return to the initial position.

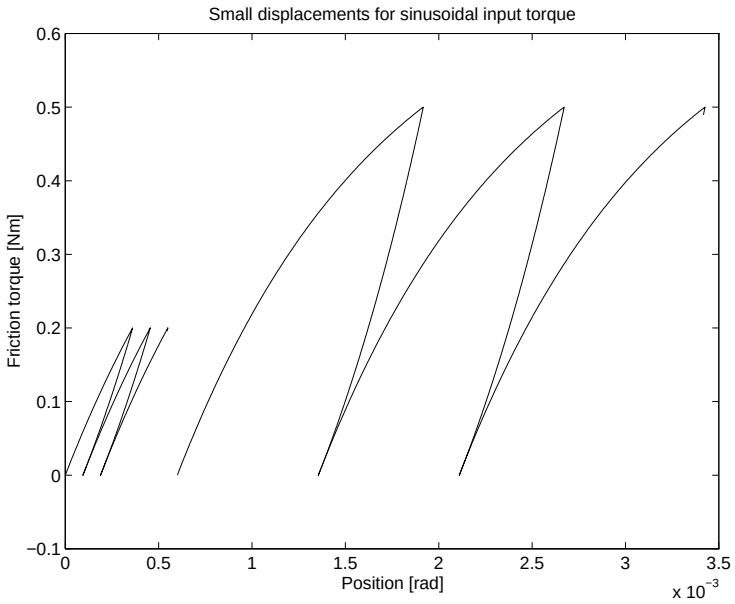

Figure 3.17 Lugre model responses to input torque $u = B + A\sin(\omega t)$ for $B = 0.1$ Nm, $A = 0.1$ Nm and $B = 0.25$ Nm, $A = 0.25$ Nm

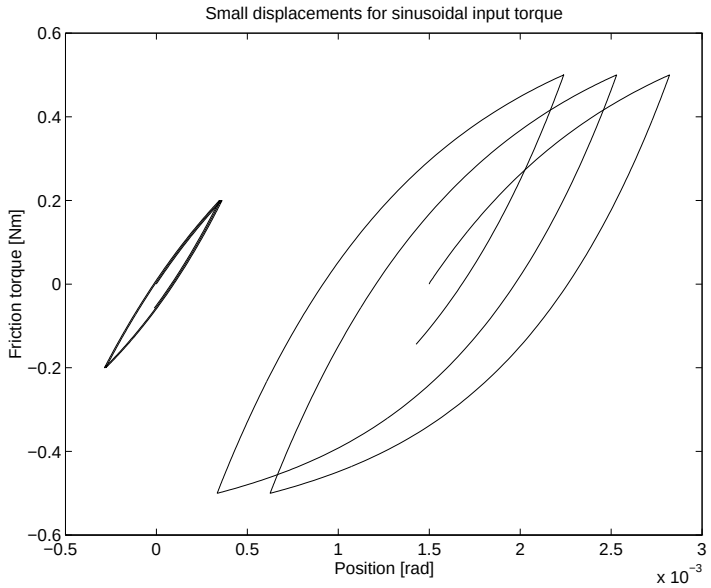

Figure 3.18 Lugre model responses to input torque $u = B + A\sin(\omega t)$ for $B = 0$ Nm, $A = 0.2$ Nm and $B = 0$ Nm, $A = 0.5$ Nm

4. Validation experiments

The experimental setup is described in appendix C. In terms to do model validation the correct model parameters are needed. The identification procedures used for the Bliman & Sorine model and the Lugre model are described in sections 2.8 and 3.8 respectively. Other experiments on the same setup is reported in [10, 26].

In all the following experiments the model of figure C.2 is assumed. This model is described by

$$J\ddot{\theta} = u - \alpha_2\dot{\theta} - \tau. \tag{4.1}$$

where u is applied external torque, $\alpha_2\dot{\theta}$ is the linear viscous part of the friction torque, and τ is the non-linear friction torque, in this section simply refered to as friction torque.

The experiments will be carried out in open loop or closed loop, in the latter case a simple PID or PI controller of the form

$$u = \left(k_p + \frac{1}{s}k_i + sk_d\right)e$$

is used. It should be noted here that the controller design is carried out without taking the viscous friction α_2 into account, although having almost the same effect as the derivative part of the controller.

The only signals directly available are the control output u and the measured position θ. The velocity $\dot{\theta}$ and the acceleration $\ddot{\theta}$ will be estimated by filtering the position data. Derivatives will be approximated by forward differences $\frac{dx}{dt}|_{t_k} \approx (x(t_{k+1}) - x(t_k))/h$. Low-pass Butterworth filters are used for disturbance reduction. The filters are run twice to avoid phase distortion, resulting in a total non-causal filter of the double order. The friction torque τ is then estimated from (4.1) as

$$\tau = u - \alpha_2\dot{\theta} - J\ddot{\theta}. \tag{4.2}$$

It should also be noted that all experiments have been carried out under a period of several days, and that the friction characteristics seem to have slightly changed during this time. The qualitative behaviour remains the same though.

4.1 Dry friction

In this section identification of the experimental setup described in appendix C with significant additional frictional load applied will be carried out. The dominating friction is therefore expected to be dry.

Identification

The procedures described in 2.8 and 3.8 will be used. The identification of the Bliman model parameters is done from the same experiments used in step 4 in the Lugre identification. An asymmetric model will be identified.

It should be noted that the friction is dependent on the position of the inertial load element, and that this dependecy is not modeled. The best way

to carry out the identification would therefore be to assure that the data sequencies collected represent a position average, i.e. a number of full turns of the load. This would be very time consuming though, and this position dependency has simply been ignored instead.

Step 1 The goal of this step is to find the Coulomb friction force α_0, and the viscous friction coefficient α_2.

Steady state velocity experiments under closed loop high gain PI control are done to collect data. Velocities in the range 0.1–10.0 rad/s are used in both directions. The friction force is estimated as an average of the applied control signal during the experiment. The smallest velocities tend to give stick-slip motion, why these values are not of good quality. The experimental steady state relationship between friction and velocity is found in figure 4.1. The nonlinearity of this relaionship can be seen, however a linear model seems to be accurate in the velocity range plotted.

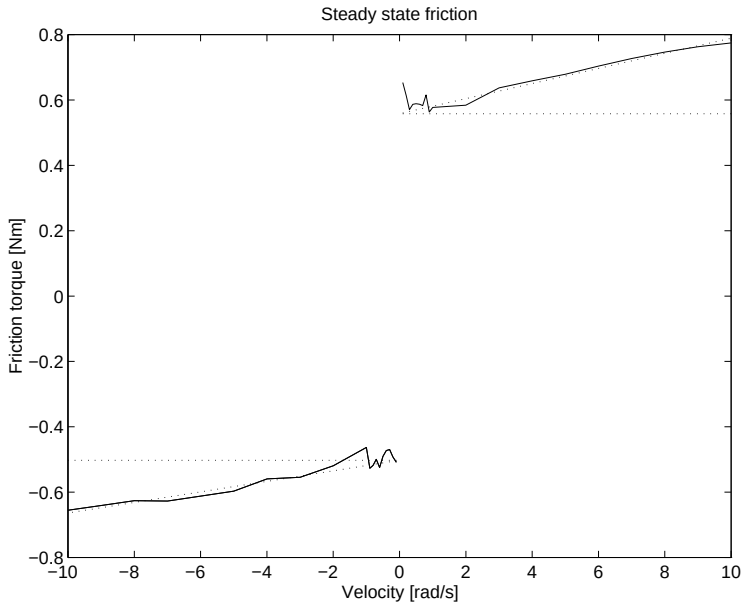

Figure 4.1 Experimental steady state relationship between friction and velocity.

The Stribeck velocity could not be found due to the stick-slip motion at low velocities. The parameter v_0 will instead be identified in another way.

Polynomial fits have been done on the data to find α_0 and α_2 as illustrated in the figure. The estimated parameters are $\alpha_0^+ = 0.58$ Nm, $\alpha_0^- = 0.50$ Nm, $\alpha_2^+ = 0.020$ Nms/rad and $\alpha_2^- = 0.016$ Nms/rad.

Step 2 In this step we identify the break-away force τ_B from a limit cycle in PID position control. The break away force has been estimated as the average of the control signal at break-away during five periods of the limit cycle. α_1 is given as $\tau_B - \alpha_0$ with α_0 taken from the preceding experiment. The result is shown in table 4.1

Step 3 We will now try to find the dynamic parameters σ_0 and σ_1. The regression model given in section 3.8 will be used together with least squares estimation. Small motions are induced by a sinusoidal input torque without

τ_B^+	τ_B^-	α_1^+	α_1^-
[Nm]	[Nm]	[Nm]	[Nm]
0.72	0.61	0.14	0.11

Table 4.1 The resulting break-away forces resulting from the experiment described in this section. The upper indices refer to the sign of the velocity during the slip following break-away.

sign changes $u = B + A\sin(\omega t)$. The frequency is fixed to $\omega = 2.0$ rad/s. The reason for not changing sign on the input torque is the small backlash present in the system. The input torque was chosen as $B = 0.1$ Nm and $A = 0.1$ Nm in both directions, which corresponds to a fraction of the earlier estimated break away torques. For comparison an experiment with larger input torques corresponding to the whole range from zero to just below break-away was carried out. It is clear that the spring like behaviour becomes clearly hysteretic for larger displacements. Se figure 4.2.

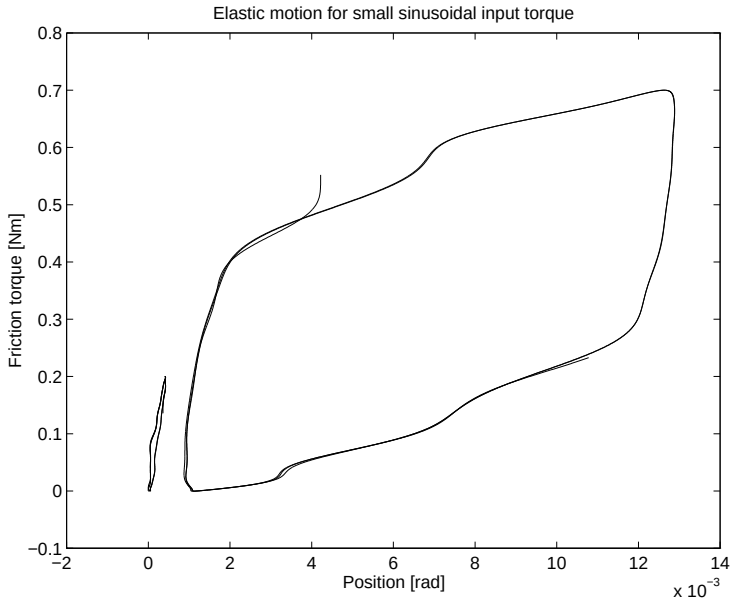

Figure 4.2 Spring like behaviour for small displacements, becoming hysteresis for larger displacements. Left: $B = 0.35$ Nm, $A = 0.35$ Nm, Right: $B = 0.10$ Nm, $A = 0.10$ Nm

The regression model is

$$F = \sigma_0 x + \sigma_1 v + e$$

where e is assumed to be white noise with variance σ_e. Defining the the output as $y = F$, the parameter vector as $\begin{bmatrix} \sigma_0 & \sigma_1 \end{bmatrix}^T$ and the regressor as $\varphi = \begin{bmatrix} x & v \end{bmatrix}^T$, we have

$$y = \varphi^T \theta.$$

With the matrices

$$Y = \begin{bmatrix} y_1 \\ y_2 \\ \vdots \\ y_N \end{bmatrix}$$

and

$$\Phi = \begin{bmatrix} \varphi_1^T \\ \varphi_2^T \\ \vdots \\ \varphi_N^T \end{bmatrix}$$

with N being the number of data points we then have

$$Y = \Phi\theta.$$

The least squares estimate

$$\min_{\hat{\theta}} \frac{1}{2}\varepsilon^T\varepsilon$$

of the prediction errors

$$\varepsilon = \left(Y - \Phi\hat{\theta}\right)$$

is then given by the normal equations

$$\hat{\theta} = \left(\Phi^T\Phi\right)^{-1}\Phi^T Y.$$

An estimate of the noise variance is given by

$$\hat{\sigma}_e^2 = \frac{\varepsilon^T\varepsilon}{N-2}$$

and an estimate of the covariance matrix of the predicted parameter vector is given by

$$\hat{\text{cov}}[\hat{\theta}] = \sigma_e^2\left(\Phi^T\Phi\right)^{-1}.$$

See [2, 18] for a detailed description of least squares estimation.

Now to the results. Identification were done in two directions with respect to an origin with zero friction force. The estimated parameters together with their estimated variance, the estimated noise variance and the roots corresponding to the linearized equation (3.10) are given below.

σ_0^+ : 460 Nm/rad
σ_1^+ : 42 Nms/rad
$\text{cov}\hat{\theta}$: $\begin{bmatrix} 0.39 & -0.018 \\ -0.018 & 0.22 \end{bmatrix}$
$\hat{\sigma}_e^2$: $2.4 \cdot 10^{-4}$
$[\ r_1 \quad r_2\ ]$: $[\ -11 \quad -17000\ ]$

σ_0^+ : 840 Nm/rad
σ_1^+ : 45 Nms/rad
$\text{cov}\hat{\theta}$: $\begin{bmatrix} 7.0 & 0.30 \\ 0.30 & 1.9 \end{bmatrix}$
$\hat{\sigma}_e^2$: $9.2 \cdot 10^{-4}$
$[\ r_1 \quad r_2\ ]$: $[\ -19 \quad -18000\ ]$

Remark 1. With v and F being estimated by forward differences the regression model corresponds to a FIR model with u as output and x as input. It then becomes important to fulfill the conditions for *persistent excitation* [2] to be able to solve the normal equations. The position signal here shows a sinusoidal form, thereby indicating that it is persistently exciting of order two, implying that it can be used to estimate two parameters, as in our case.

Remark 2. We see that the spring like characteristics are highly direction [1] dependent with respect to σ_0, whereas σ_1 seems to be essentially the same in both directions. This is good news since we are not very happy about introducing a direction dependency in this parameter. (See discussion in section 3.7).

Remark 3. The poles of the linearized equation of motion are real and of very different magnitude, and will most probably result in stiff equations badly conditioned for numerical integration. Assuming that σ_0 is the most important parameter we can therefore choose σ_1 to give well damped complex poles which are better suited for simulations.

Step 4 In this step identification of the parameter v_0 is done. In the Lugre model v_0 decides at which velocity a drop in the friction force shall take place, see section 3.2. For a slowly ramped up input torque this drop take place at the Stribeck velocity v_0, and this will here be used to identify this parameter. More precisely half the drop has been made at the Stribeck velocity. By doing this experiment and estimate velocity v and friction force τ, and then plot τ versus v the velocity v_0 is found graphically.

The same experiment is used to obtain the friction τ versus position x from which Bliman model parameters are identified.

A sinusoidal input torque input torque $u = B + A\sin(\omega t)$ with $A = 1$ Nm, $B = 0.06$ Nm and $\omega = 0.1$ rad/s will be used. The reason for the small bias is totally practical and is due to the asymmetric friction. The bias corresponds to half the different break-away torque in the different directions and gives an almost symmetric motion. This is however not at all required for the results.

Figure 4.3 shows the obtained curve for $u > 0$. From this we can see that $v \approx 0.01$ rad/s at break-away, and that $v \approx 0.1$ rad/s at half the drop. A corresponding plot for $u < 0$ gives the same values also in this direction.

In figure 4.4 the corresponding plot for friction force τ versus position x is plotted. The Bliman identification parameters are graphically identified as

$$[\ f_k \quad f_s \quad s_e \quad s_p\ ] = [\ 0.48 \quad 0.70 \quad 0.024 \quad 0.025\ ].$$

The map (2.22) from these parameters to model parameters has no solution for these values though, whereas the identification becomes impossible. The problem is that s_p is too close to s_e, which make the condition for the map to have solutions not to be fulfilled. The friction torque drop after break-away is too fast, in other words.

A second try, in which we chose s_p less close to s_e gives a solution to the map. The identification parameters now become

$$[\ f_k \quad f_s \quad s_e \quad s_p\ ] = [\ 0.5261 \quad 0.7077 \quad 0.0297 \quad 0.0604\ ],$$

and the model parameters

$$[\ f_1 \quad f_2 \quad \varepsilon_f \quad \eta\ ] = [\ 1.6130 \quad 1.0869 \quad 0.0201 \quad 0.6347\ ].$$

[1] Direction here does not signify the sign of velocity, but on which side of the position origin corresponding to zero friction force the motion takes place.

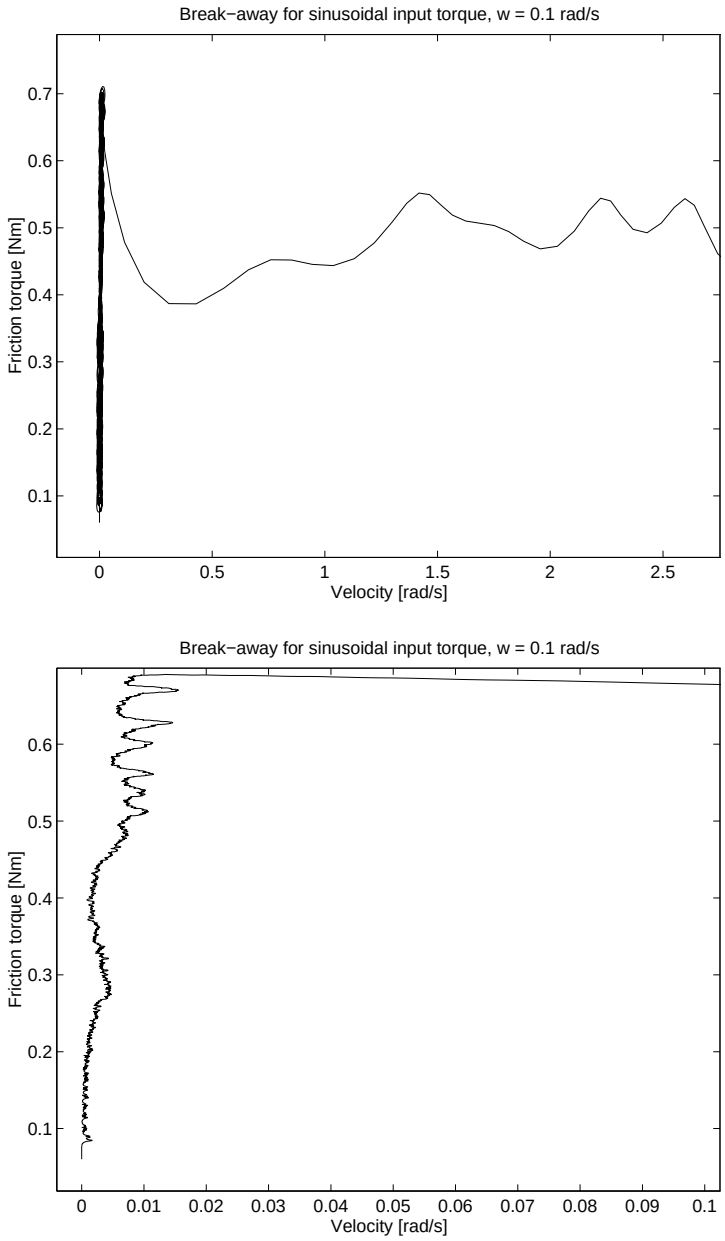

Figure 4.3 Upper: Part of hysteresis curve for cyclic motion in stick and slip region induced by a sinusoidal input torque, used for identification of v_0. Lower: The break-away region in zoom.

For completion we also show how the system during this motion behaved during the transition from slip to stick in the friction force versus position plot. This is shown in figure 4.5. The increase in friction torque just before stick is clearly seen.

Remark 1. The identification of the Bliman parameters is complicated by the fact that there is a backlash present in the system. The identification shall be done in the hysteresis curve for friction versus position where the distance from the position corresponding to sign change of velocity to the postion of the break-away torque shall be determined. In this setup this distance is increased

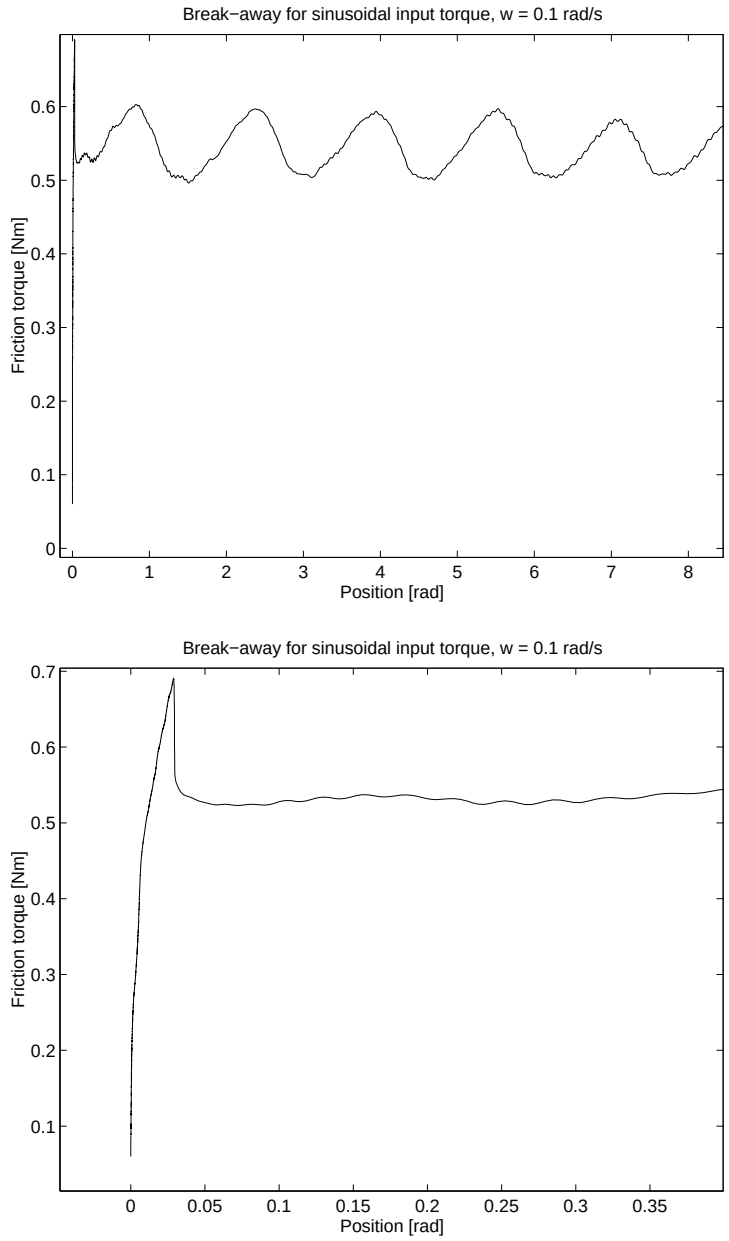

Figure 4.4 Upper: Part of hysteresis curve for cyclic motion in stick and slip region induced by a sinusoidal input torque, used for identification of v_0. Lower: The break-away region in zoom.

by the backlash magnitude.

Remark 2. Moreover the Bliman model impose conditions on s_e and s_p to give a solution to the identification mapping (2.22), e.g. $3s_e < s_p$. This relation is not fulfilled in this system, which makes the identification impossible. A possibility would be to pick s_e arbitrarily at a point that fulfills the condition, giving at least a set of parameters, however of doubtful quality.

A conclusion migh be that the Bliman model poorly models dry friction with relative large pre-sliding displacement, where the points s_e and s_p tends to be close but still not very small.

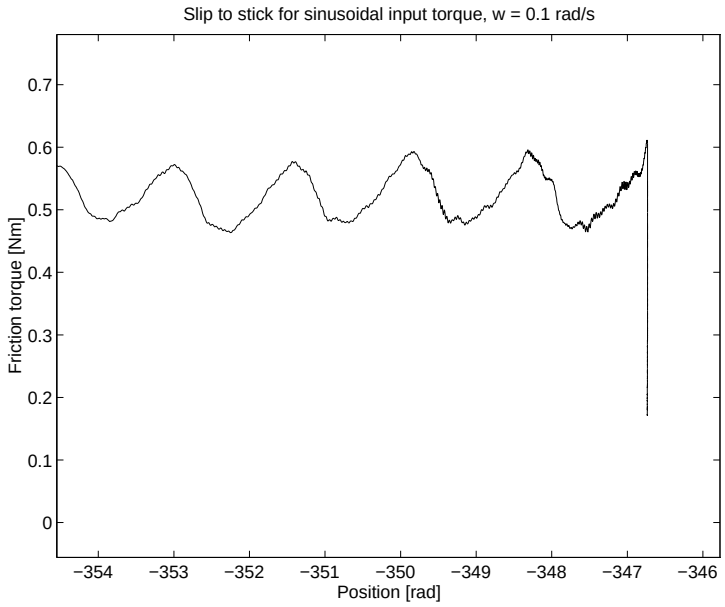

Figure 4.5 Part of hysteresis curve for cyclic motion in stick and slip region induced by a sinusoidal input torque.

Remark 3. The friction torque drop after break-away seems to be very abrupt, and almost discontinuous. Compare with wet friction.

Result A summary of the identification is given in table 4.2. An asymmetric σ_0 makes it very important to have good accurancy around $z = 0$ in simulations. For practical reasons we will therefore use an average of σ_0. A value of σ_1 giving less stiff equations is also wanted. From the linearized equations one can see that $\sigma_1 \approx 3$ Nms/rad gives a damping around one. (Approximatively since the asymmetric α_2 makes the linearized equation ambiguous.)

The parameters above should be seen as initial guesses only since the identification procedure used not is optimal. The important thing is to look at simulations of the system and trim the parameters to fit the experimental results. This is an iterative procedure which requires some feeling for how system performance changes when a certain parameter is changed.

	σ_0 [Nm/rad]	σ_1 [Nms/rad]	v_0 [rad/s]	α_0 [Nm]	α_1 [Nm]	α_2 [Nms/rad]
+	460	44	0.1	0.58	0.14	0.020
−	840	44	0.1	0.50	0.11	0.016
+	650	1	0.1	0.58	0.14	0.020
−	650	1	0.1	0.50	0.11	0.016

Table 4.2 Identified Lugre parameters for dry friction case.

Hysteresis for large motions

figures 4.6 and 4.7 shows characteristic hysteresis curves in friction versus position for motion induced by a sinusoidal input torque. The sharp drop in

friction torque after break-away is difficult to achieve with the Bliman-Sorine model if the pre-sliding displacement is significant, see discussion in 2.8.

Remark 1. In figure 4.6 the velocity reached during slip is so large that the linear model of the viscous friction is no longer valid. Thus the viscous friction term is over-estimated, and the estimated friction according to (4.2) becomes too small. The "waves" visible in figure 4.6 is due to an unmodeled position dependency of the dynamics of a period $\pi/2$ rad, probably due to excentricity of a wheel in the gear-box. This dependency is seen in most plots, except when low-pass filters of very low bandwidth have been used. There is also a $\approx$135 Hz time periodic disturbance present in the system. Maybe an aliasing frequency of the 40 kHz puls-width modulated control signal. It might also be an effect of two samplers with different sampling frequency in series after the position sensor. This disturbance is filtered away when possible. For fast motions this is not possible without filter away system dynamics as well. A velocity dependent torque ripple were expected to be found in addition to the above mentioned disturbances, but was not.

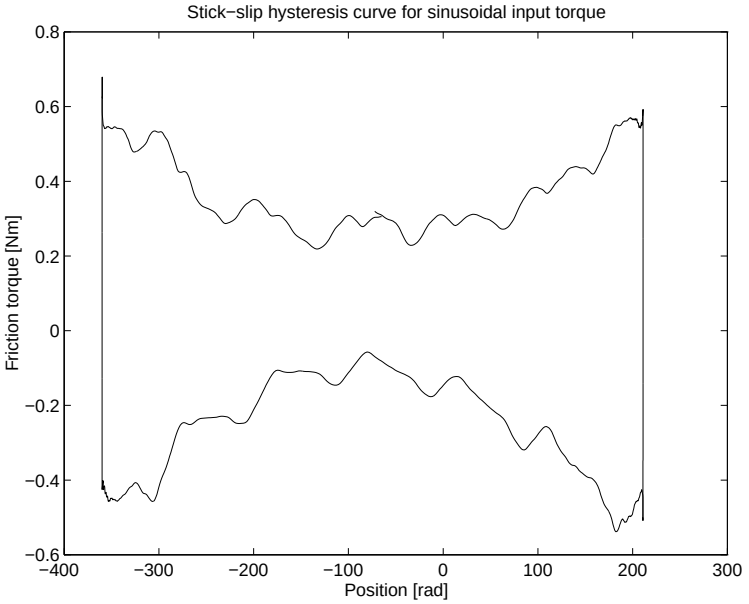

Figure 4.6 Hysteresis curve for cyclic motion in stick and slip region induced by a sinusoidal input torque. The frequency of the input torque was 5 rad/s.

Rate dependency

Experiments were carried out in which an sinusoidal input torque $u = B + A\sin(\omega t)$, $A = 0.06$ Nm, $B = 1.0$ Nm, gave a stick-slip cycle. Different angular frequencies ω were used to investigate the rate dependency of the break-away torque. The break-away torque is taken as an average of five break-away points. The results are given in table 4.3. For the frequency $\omega = 10$ rad/s the break-away peak is no longer distinguishable. As one can see the variances of the experimental figures are rather high, only five periods were used for the averaging. The trend is clear though, and corresponds well with the Lugre model response.

In table 4.4 the magnitudes of the friction force peak at the transition from slip to stick are given for experiments and simulations. The experimental values

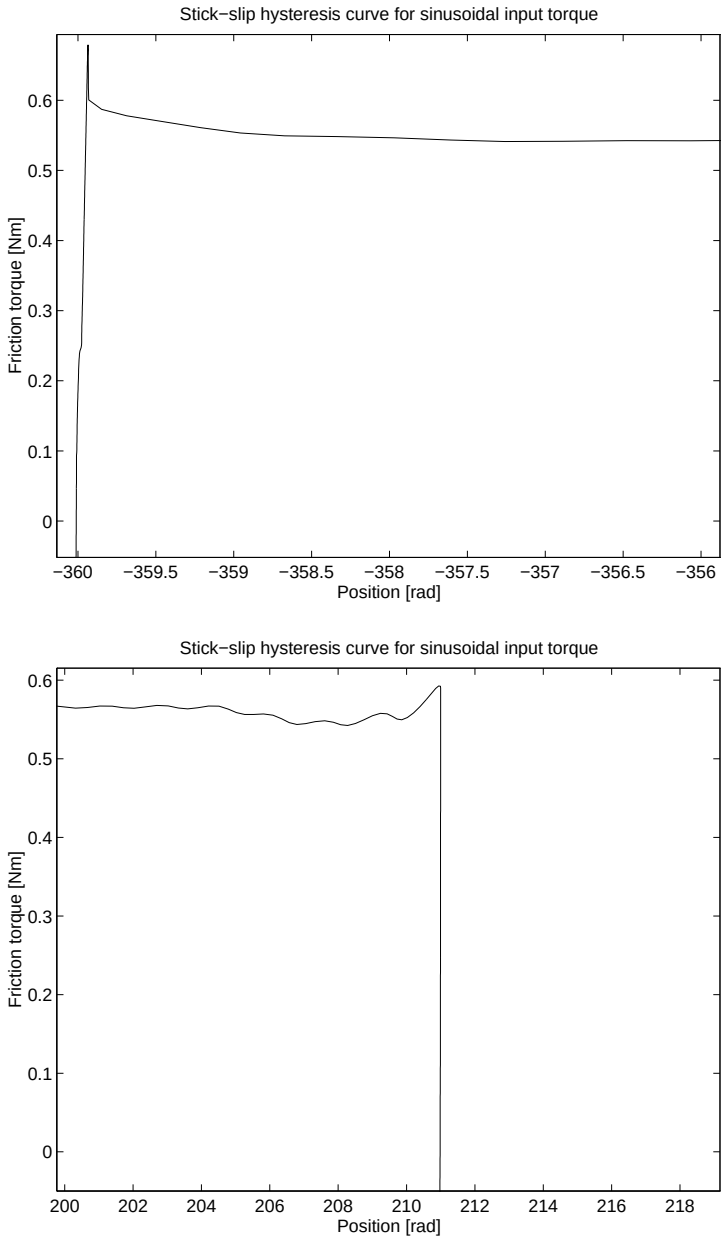

Figure 4.7 Zooms from figure 4.6. Upper: Break-away region in zoom. Lower: Slip to stick region in zoom.

have been taken from inspection of representative plots, and no averaging has been done. The conclusion one can draw though is that the Lugre model well seems to reproduce the phenomenon.

Figures 4.8, 4.9, 4.10 shows experimental responses together with Lugre model responses to three different rates of sinusoidal input torque. The Lugre model clearly shows the correct qualitative behaviour. Note that the Lugre parameters used do not match the kinetic friction, nor the pre-sliding displacement exactly.

	ω [rad/s]	τ_B^+ [Nm]	$V[\tau_B^+]$	$\dot{u}^+$ [Nm/s]	τ_B^- [Nm]	$V[\tau_B^-]$	$\dot{u}^-$ [Nm/s]
Experimental	0.1	0.77	0.0036	0.076	0.58	0.0022	0.070
	1.0	0.72	0.013	0.83	0.55	0.0030	0.83
	10.0	-	-	≈ 10	-	-	≈ 10
Lugre	0.1	0.71	-		0.61	-	
	1.0	0.69	-		0.59	-	
	10.0	0.60	-		0.51	-	

Table 4.3 Varying break-away torques experimentally and from Lugre simulations. ω is angular frequency of the applied input torque. τ_B^+, τ_B^- are break-away torques in different directions. $V[\cdot]$ is variance. $\dot{u}$ is velocity at break-away.

	ω [rad/s]	τ^+ [Nm]	τ^- [Nm]
Experimental	0.1	0.63	0.50
	1.0	0.62	0.48
	10.0	-	-
Lugre	0.1	0.62	0.53
	1.0	0.59	0.51
	10.0	0.58	0.50

Table 4.4 Friction torque peaks at the transition from slip to stick, experimentally and from Lugre model simulations.

Small displacements

The experimental responses to small sinusoidal input torques $u = B + A\sin(\omega t)$ are shown in figure 4.2. The corresponding Lugre model responses are shown in figure 3.17. The reason for using a smaller amplitude for the larger input torque in the simulation is that the Lugre model with the parameters used overestimates the rate dependency of the break-away torque, and thus give break-away for the torque used experimentally. We can see that the Lugre displacements are of the correct magnitude though. Also we see that the experimental system returns to the initial position while Lugre does not. This might be a qualitatively wrong behaviour. We have to ask ourselves though what we see in the experimental result. Is it frictional small displacements or mechanism stiffness? In figure 2.15 the corresponding responses for the Bliman & Sorine model are shown. We see that the qualitatively wrong behaviour is found also here. This is expected since both models have similar linearized equations. An important difference is the magnitude of the displacements. It differs almost a factor 10. This can be explained by (2.16), which gives $\sigma = 72$ Nm/rad, to be compared with $\sigma_0 = 650$ Nm/rad for the Lugre model. The Lugre response shows better accordance with experiments.

In figure 3.18 the Lugre responses with symmetric input torques are shown. These show the shapes we wanted in the previous figure. The experimental conditions were not these however. Experimentally input torques without sign changes were used to avoid the small backlash in the system. Figure 2.16 shows the corresponding responses of the Bliman & Sorine model. Qualitatively the same as Lugre, but still differs a factor 10 in magnitude.

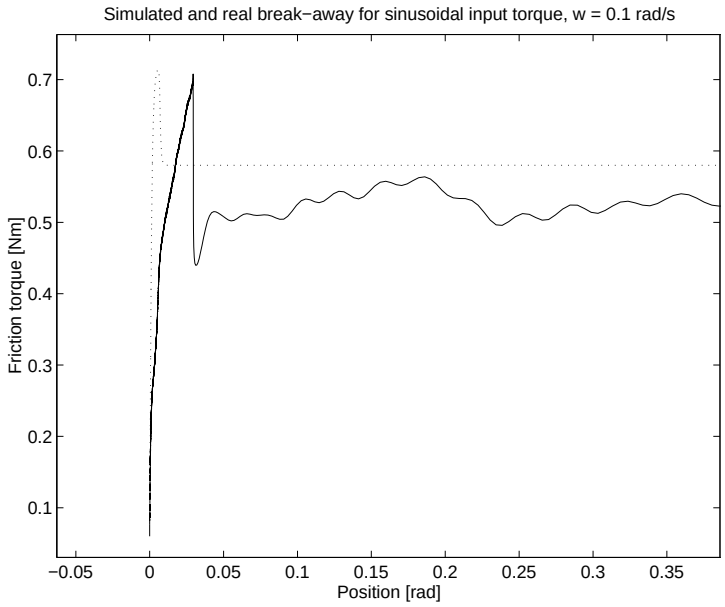

Figure 4.8 Experimental (solid) and Lugre (dashed) model response to input torque $u = B + A\sin(\omega t)$ for $B = 0.06$ Nm, $A = 1.0$ Nm, $\omega = 0.1$ rad/s.

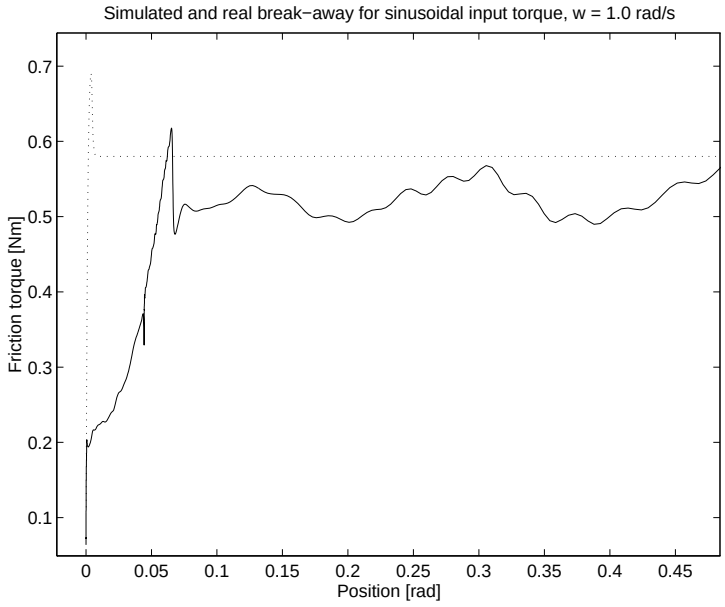

Figure 4.9 Experimental (solid) and Lugre (dashed) model response to input torque $u = B + A\sin(\omega t)$ for $B = 0.06$ Nm, $A = 1.0$ Nm, $\omega = 1.0$ rad/s.

Non-linear viscous friction

As noted above the linear model of viscous friction is only valid in a limited velocity range. In figure 4.11 this is illustrated by plotting a fast motion with velocities without the range from within the viscous friction was estimated. The friction force plotted is estimated from (4.2), and is thus dependent on a correct estimate of viscous friction. Ideally in this plot friction should be equal to kinetic friction during slip, and appear as a horizontal straigh line.

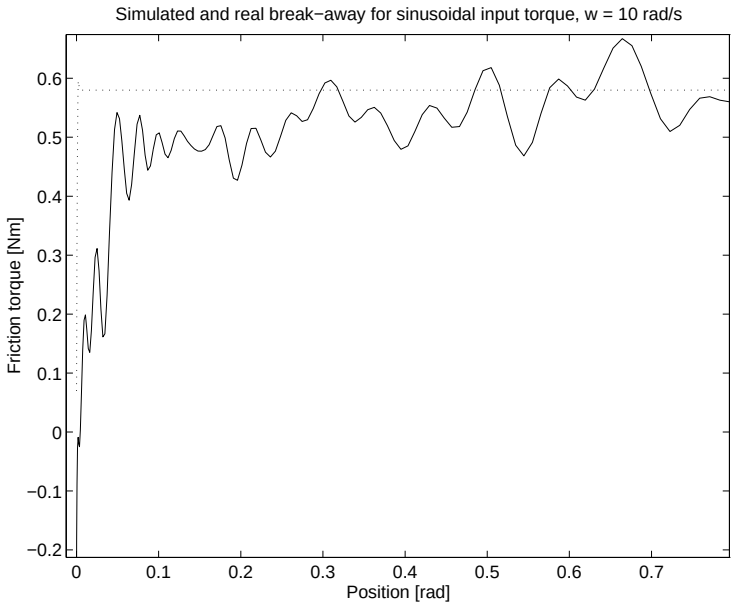

Figure 4.10 Experimental (solid) and Lugre (dashed) model response to input torque $u = B + A\sin(\omega t)$ for $B = 0.06$ Nm, $A = 1.0$ Nm, $\omega = 10$ rad/s.

A motion with low velocity is seen in figure 4.4, where apparently the viscous friction is correctly estimated (after break-away we have constant kinetic friction).

The conclusion thus is that for motions varying over a large velocity range non-linear viscous friction modeling seems necessary.

Other non-linearities

In the setup used the friction is distributed in several parts, between which there exist small backlashes. This gives a complex behaviour at break-away since different parts start to move at different times. In this system the backlash is of a magnitude 2–3 times larger than the pre-sliding displacement.

In figure 4.12 the distributed friction– backlash behaviour is seen at break-away. The break-away is in fact two break-aways. First a small which is immidiately stopped after a distance corresponding to the backlash magnitude (motion from left to right contact in the backlash). In this position the system remains in stick until the break-away torque is reached, and slip occurs. The backlash magnistude is from the plots estimated to approximately 70 mrad, while the pre-sliding displacement is around 25 mrad.

4.2 Wet friction

Here we carry out experiments on the system without externally applied friction, resulting in a system with only lubricated, or wet, friction. We want to investigate if such a system has qualitatively different properties than the dry friction system. If so, which of the investigated dynamic friction models is best in each case?

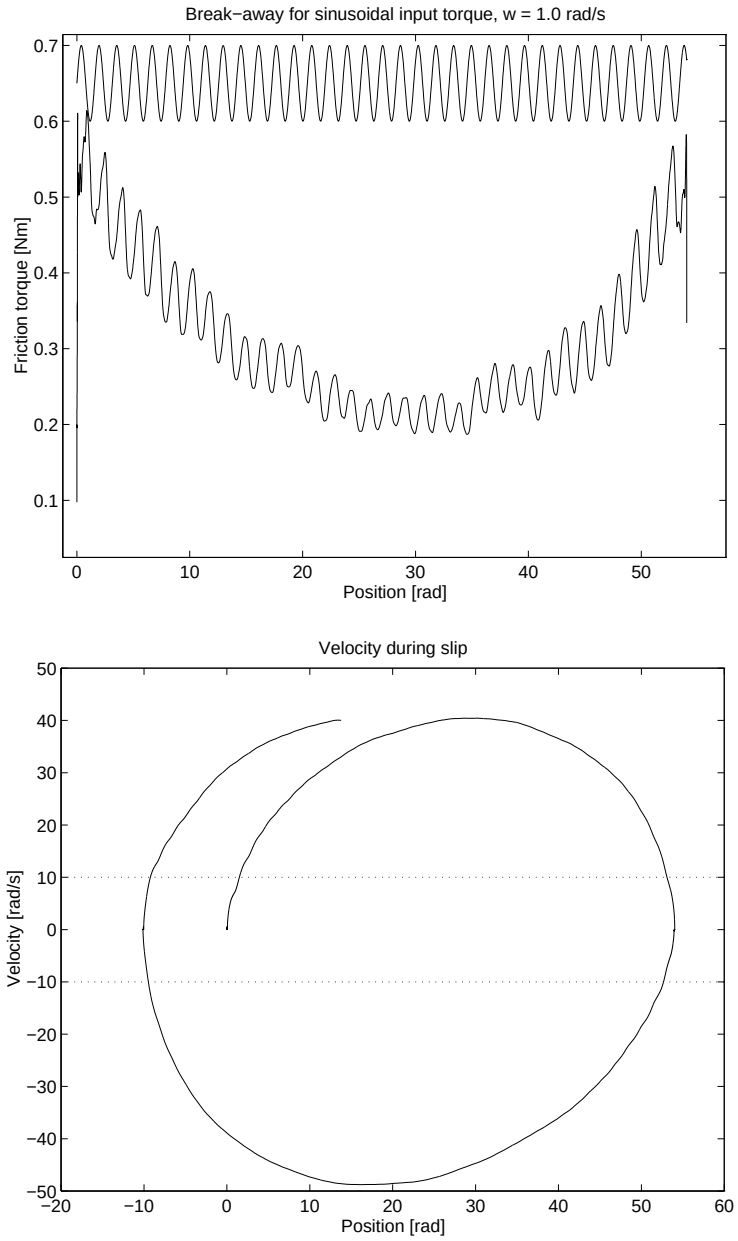

Figure 4.11 Failure of linear viscous friction modeling. Upper: Overcompensation of viscous friction. Friction versus position hysteresis plot and a sinusoidal reference signal of period $\pi/2$ rad to compare with the position dependent variation. Lower: Velocity during slip plotted versus posistion. The velocity range from within the linear model is identified is marked with dotted lines.

Identification

Step 1 The procedure is the same as for dry friction. The obtained steady state friction force versus velocity plot is found in figure 4.13.

The Stribeck velocity was not found here either, but this time due to the very low velocities, implying unreasonable long experiments to obtain representative data. The parameter v_0 will instead be identified as in step 4 above.

Polynomial fits gives α_0 and α_2 as illustrated in the figure. The estimated

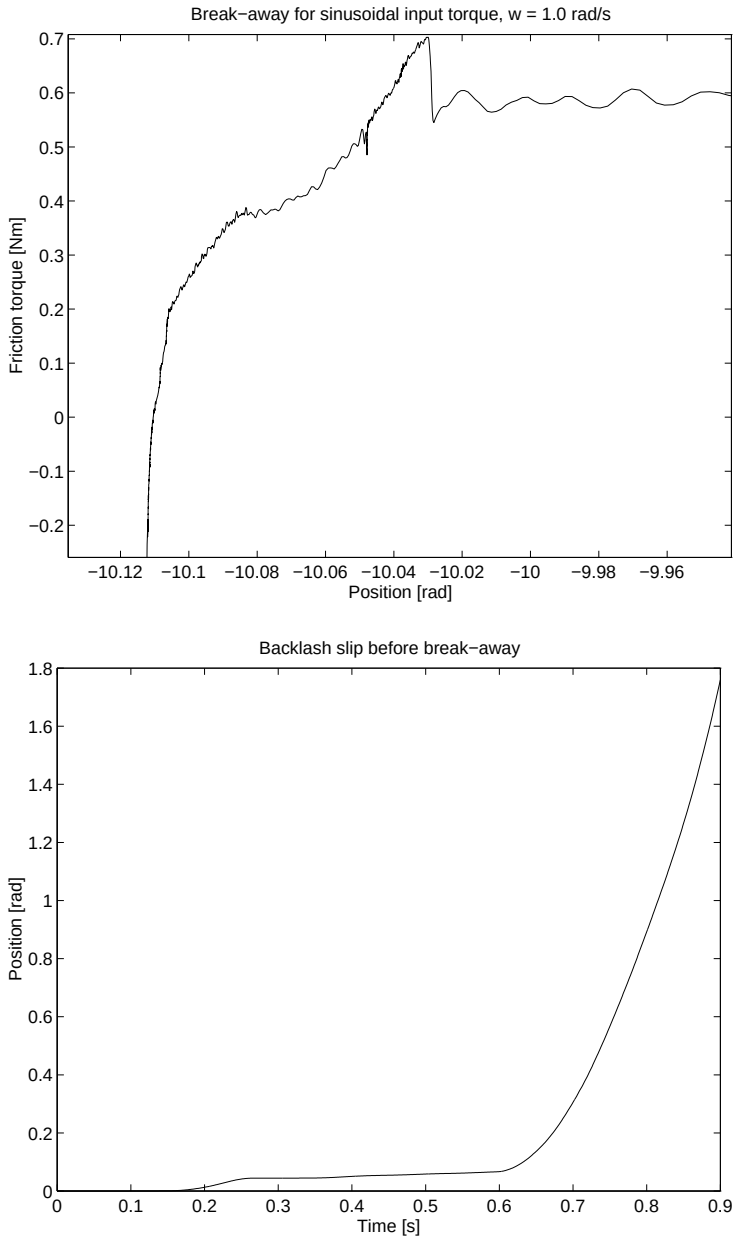

Figure 4.12 Backlash and distributed friction.

parameters are $\alpha_0^+ = 0.36$ Nm, $\alpha_0^- = 0.24$ Nm, $\alpha_2^+ = 0.017$ Nms/rad and $\alpha_2^- = 0.017$ Nms/rad, which well fits earlier identifications made on the system.

Step 2 The procedure is identical to the one used in the dry friction case. The result is shown in table 4.5 and figure 4.14.

Step 3 Refer to step 3 in the dry case to learn the procedure. The input torque has in this case been scaled down appropriately. The experimentally found friction force versus displacement plots are found in figure 4.15.

Estimated parameters are given below.

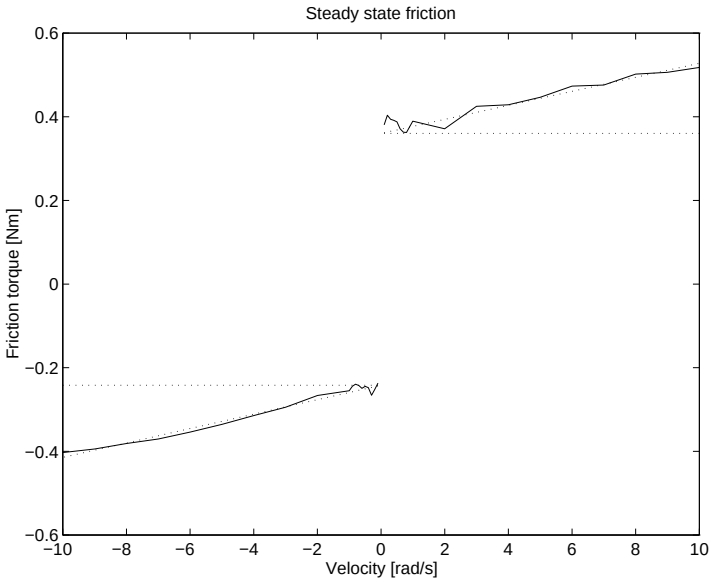

Figure 4.13 Experimental steady state relationship between friction and velocity.

τ_B^+ [Nm]	τ_B^- [Nm]	α_1^+ [Nm]	α_1^- [Nm]
0.46	0.29	0.098	0.050

Table 4.5 The resulting break-away forces resulting from the experiment described in this section. The upper indices refer to the sign of the velocity during the slip following break-away.

$$
\begin{array}{lcl}
\sigma_0^+ & : & 330 \text{ [Nm/rad]} \\
\sigma_1^+ & : & 25 \text{ [Nms/rad]} \\
\mathrm{cov}\hat{\theta} & : & \begin{bmatrix} 0.653 & 0.0156 \\ 0.0156 & 0.1826 \end{bmatrix} \\
\hat{\sigma}_e & : & 1.4 \cdot 10^{-4} \\
\begin{bmatrix} r_1 & r_2 \end{bmatrix} & : & \begin{bmatrix} -13 & -10000 \end{bmatrix}
\end{array}
$$

$$
\begin{array}{lcl}
\sigma_0^+ & : & 230 \text{ [Nm/rad]} \\
\sigma_1^+ & : & 28 \text{ [Nms/rad]} \\
\mathrm{cov}\hat{\theta} & : & \begin{bmatrix} 0.0334 & 0.0020 \\ 0.0020 & 0.0266 \end{bmatrix} \\
\hat{\sigma}_e & : & 2.1 \cdot 10^{-5} \\
\begin{bmatrix} r_1 & r_2 \end{bmatrix} & : & \begin{bmatrix} -8 & -11000 \end{bmatrix}
\end{array}
$$

Step 4 Again, same procedure as for the dry case. A sinusoidal input torque input torque $u = B + A\sin(\omega t)$ with $A = 0.5$ Nm, $B = 0.08$ Nm and $\omega = 0.1$ rad/s is this time used.

Figure 4.16 shows the obtained curve for $u > 0$. Here it can be seen that the break-away region shows a complex structure. As a matter of fact, we have two break-away points. The former shows no torque peak in the friction force versus displacement plot. The latter is picked for identification of v_0. From this we can see that $v \approx 0.01$ rad/s at break-away. The value at half the drop,

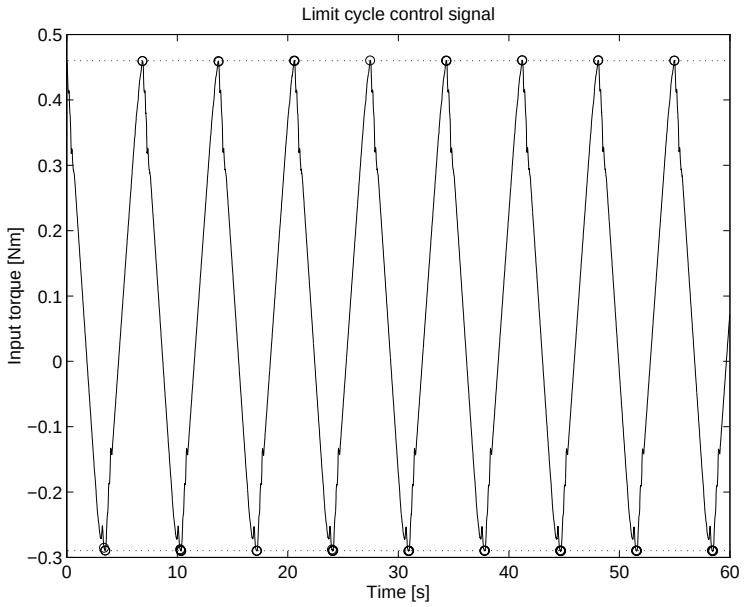

Figure 4.14 Identified break-away reached in control signal.

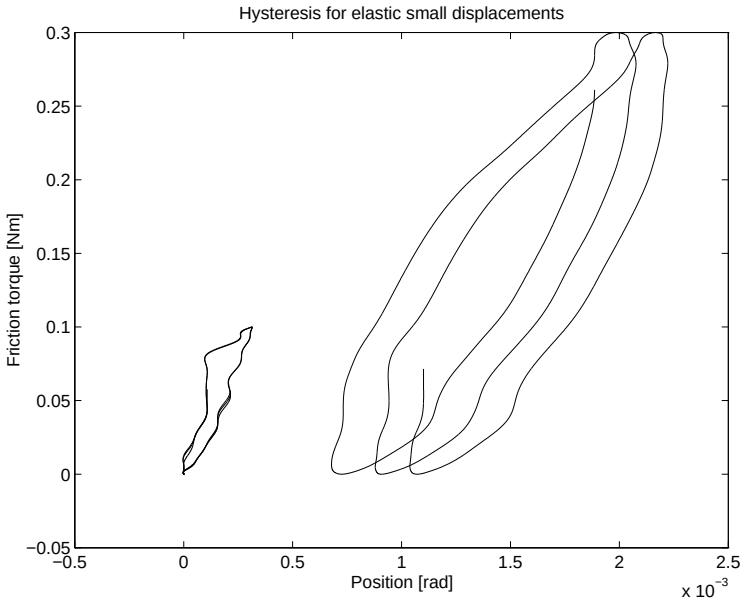

Figure 4.15 Spring like behaviour for small displacements, becoming hysteresis for larger displacements. Left: $B = 0.15$ Nm, $A = 0.15$ Nm, Right:$B = 0.05$ Nm, $A = 0.05$ Nm

corresponding to v_0, is not easily seen. We assume $v \approx 0.1$ rad/s is a good value as in the dry case. A corresponding plot for $u < 0$ gives the same values also in this direction.

In figure 4.17 the corresponding plot for friction force τ versus position x is plotted. The complex break-away region makes the Bliman identification difficult. Figure 4.18 shows that again we have several partial break-aways preceding the full break-away. The Bliman identification parameters are graphically

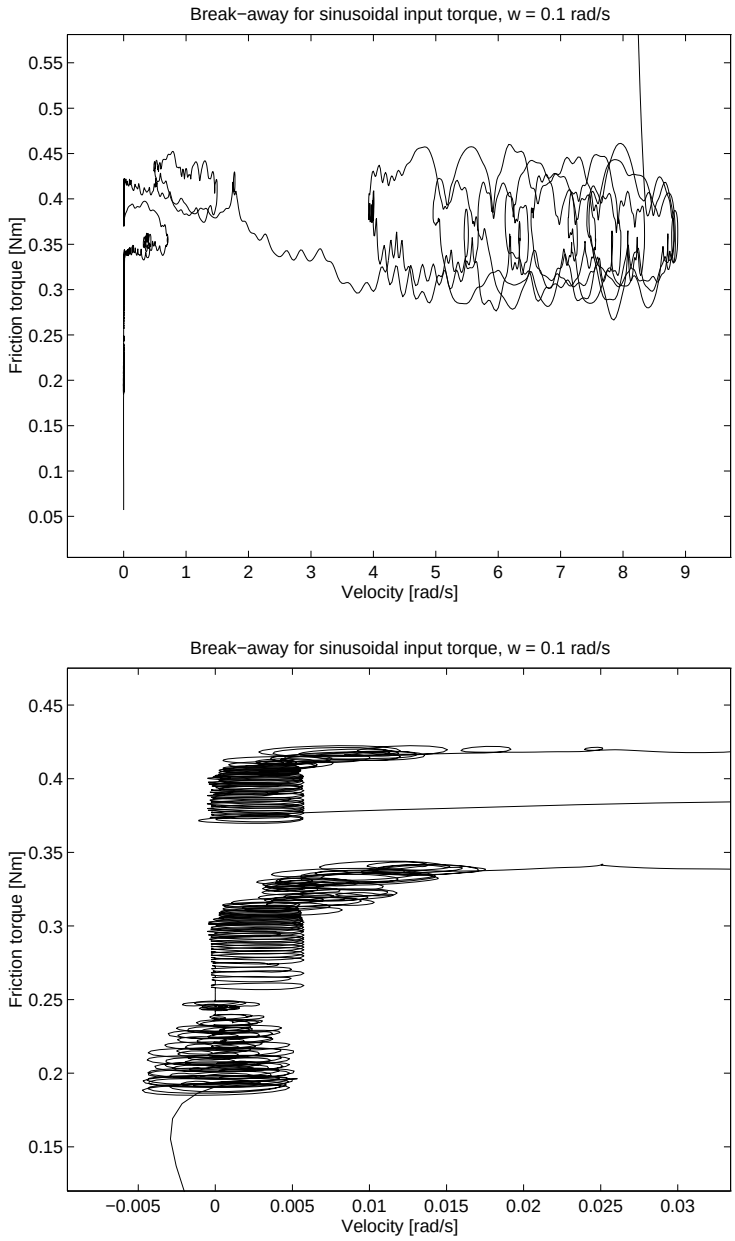

Figure 4.16 Upper: Part of hysteresis curve for cyclic motion in stick and slip region induced by a sinusoidal input torque, used for identification of v_0. Lower: The break-away region in zoom.

chosen as

$$\begin{bmatrix} f_k & f_s & s_e & s_p \end{bmatrix} = \begin{bmatrix} 0.3276 & 0.4183 & 0.2519 & 0.6016 \end{bmatrix}.$$

The map (2.22) from these parameters to model parameters gives

$$\begin{bmatrix} f_1 & f_2 & \varepsilon_f & \eta \end{bmatrix} = \begin{bmatrix} 0.6136 & 0.2859 & 0.2005 & 0.4434 \end{bmatrix}.$$

Result A summary of the identification is given in table 4.6. The comments from the result section in the dry case are still valid.

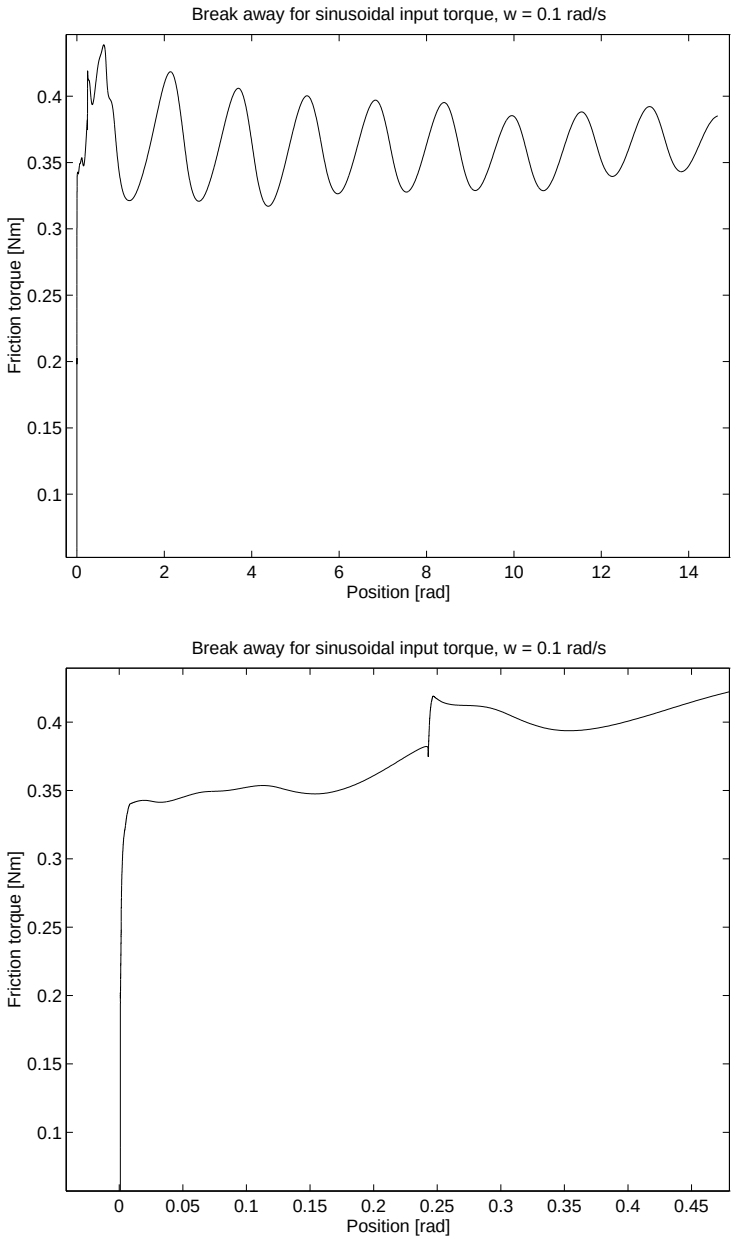

Figure 4.17 Upper: Part of hysteresis curve for cyclic motion in stick and slip region induced by a sinusoidal input torque, used for identification of v_0. Lower: The break-away region in zoom.

From figure 4.15 we see that the experimental behaviour show better correspondence with the Lugre model behaviour in figure 3.17 for the lubricated case than for the dry. Still the qualitative behaviour is different for the model. Figure 3.18, which shows the Lugre model response for symmetric input torque, better corresponds to the experimental results.

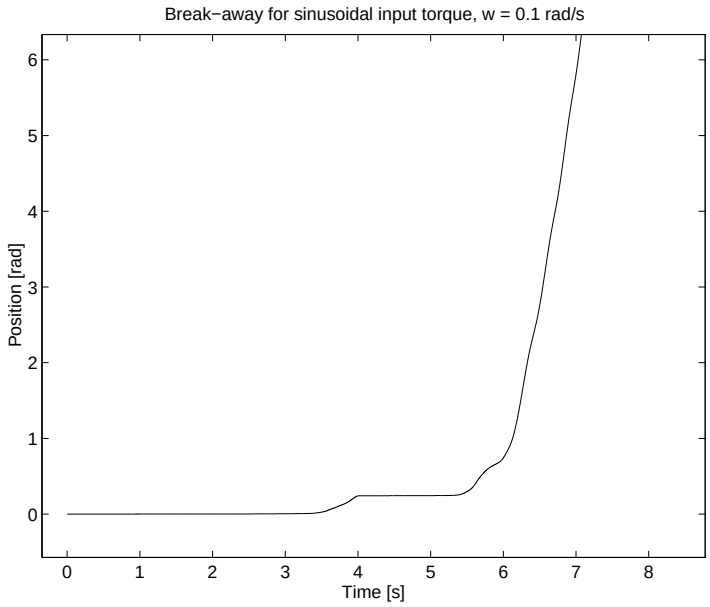

Figure 4.18 System break-away composed of several partial break-aways.

	σ_0 [Nm/rad]	σ_1 [Nms/rad]	v_0 [rad/s]	α_0 [Nm]	α_1 [Nm]	α_2 [Nms/rad]
+	330	26	0.1	0.36	0.098	0.017
−	230	26	0.1	0.24	0.050	0.017
+	280	1	0.1	0.36	0.098	0.017
−	280	1	0.1	0.24	0.050	0.017

Table 4.6 Identified Lugre parameters from wet friction case.

4.3 Conclusions

As emphasized before the purpose of this validation has been to qualitatively verify model properties. The identification procedure has been rather simple, and can in no way be expected to give optimal results. Qualitatively both the Bliman & Sorine and the Lugre model well models the phenomena they are supposed to. In the case with pre-sliding displacements qualitatively wrong behaviour is seen for both models. We are not sure that what we see experimentally is actual frictional pre-sliding displacements. The displacement magnitudes are too large, and probably we have mechanism stiffness playing the same role.

In both the dry and the wet friction case the wet friction is the same. From the identified parameters we see that the additional dry friction does not add any significant viscous friction. The stiction and the kinetic friction are larger for the dry case. The only qualitative difference encountered is that the stiction force peak in the dry case is much sharper than in the wet case. This is more easy to capture with the Lugre model. The Bliman & Sorine model has difficulties with such behaviour, at least when the pre-sliding displacement is relatively large. This may sound contradictory to the purposes of the models. The Bliman & Sorine model is presented as a dry friction model, and thus

could be expected to well capture this behaviour. The Lugre model is inspired by properties introduced by lubrication.

The discrepancies sometimes found between experimental results and simulated model results might be explained by a poor identification. Efforts have been made however to manually tune parameters to fit observations, but changing the parameters change the overall model behaviour in a complex way why it has been impossible to find one set of parameters that fits all phenomena. Therefore a good strategy might be to analyze which phenomena are of most importance in a specific system, and then adapt friction model parameters to model these in a good way.

5. Limit cycles

Limit cycles are known to appear in systems with friction controlled by a PID regulator. Often these are of a *stick-slip* character, i.e. motion alter between zero velocity and non-zero velocity due to a difference between stiction force and kinetic friction. Stick-slip limit cycles can appear as stick-slip motion in velocity control, or as oscillations around the setpoint in position control. In this chapter we investigate the ability of the models (2.7) and (3.4) to reproduce this behaviour in position control from simulation as well as from describing function analysis. We also take a heuristic approach to limit cycle prediction, where the limit cycles are found by little knowledges of the system and approximations of the equations of motion. This method is then generalized by removing the approximations. The results are then validated by experiments.

For a given system with friction and a PID controller we shall try to give answers to the following questions:

1. For which controller parameters can there be a limit cycle present?
2. Which are the conditions for the limit cycle to appear?
3. What are then the period and the error amplitude of the limit cycle?

5.1 Limit cycles in experiments

The experimental setup is presented in appendix C.

A PID controller will be used for position control. Assuming that the discrete time PID that is used experimentally is close enough to a continuous time PID for short sampling periods we choose the system in figure 5.1 for design and later on simulations.

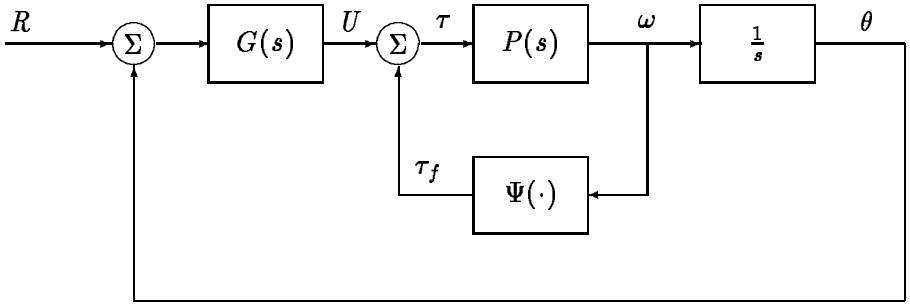

Figure 5.1 Model of experimental setup used for design and simulation.

The PID is first designed as for a system without friction, and chosen to give a closed loop transfer function characteristic polynomial

$$(s^2 + 2\zeta_c\omega_c s + w_c^2)(s + n_c\omega_c). \tag{5.1}$$

The plant has the transfer function

$$G_0(s) = \frac{1}{Js^2} \tag{5.2}$$

from torque to position, and the PID control law is

$$U = G(s)E \tag{5.3}$$

with $E = R - Y$, and U having dimension torque.

$$G(s) = \frac{k_d s^2 + k_p s + k_i}{s} = J\frac{\bar{k}_d s^2 + \bar{k}_p s + \bar{k}_i}{s} \tag{5.4}$$

The closed loop transfer function becomes

$$G_c(s) = \frac{GG_0}{1 + GG_0} = \frac{\bar{k}_d s^2 + \bar{k}_p s + \bar{k}_i}{s^3 + \bar{k}_d s^2 + \bar{k}_p s + \bar{k}_i}. \tag{5.5}$$

Identification of coefficients in (5.1) gives the PID parameters $\bar{k}_p$, $\bar{k}_i$ and $\bar{k}_d$.

If linear friction modeling is used and the viscous friction coefficient α is known, it is certainly better to include this in the design. This is straightforward, and the resulting design equation becomes

$$G_c(s) = \frac{GG_0}{1 + GG_0} = \frac{\bar{k}'_d s^2 + \bar{k}'_p s + \bar{k}'_i}{s^3 + (\bar{k}'_d + \alpha)s^2 + \bar{k}'_p s + \bar{k}'_i}. \tag{5.6}$$

We choose for our investigation a limit cycle from the wet friction case in the previous chapter. The closed loop design parameters of table 5.1 gives the PID parameters of table 5.2. A registration of an experimental limit cycle

ω_c [rad/s]	ζ_c	η_c
6	0.5	1

Table 5.1 Design parameters for PID regulator.

k'_p [Nm/rad]	k'_i [Nm/rads]	k'_d [Nms/rad]
72	216	5.2

Table 5.2 PID parameters used to give limit cycle.

is shown in figure 5.2. A reference step $r = 1$ rad is given at $t = 0$ s from zero initial conditions. We see that the limit cycle is symmetric in position amplitude, but asymmetric in control signal amplitude. How this can be interpreted is discussed in section 5.4. We also see the pre-sliding displacement in the position signal. In figure 5.3 the control signal is plotted together with the estimated non-linear friction. What we see here is the break-away, slip and the stick of a limit cycle half-period. Ideally we would like the friction to be constant, equal to the kinetic friction, during slip. Unfortunately position dependent disturbances in the setup spoil this, and instead the estimated friction decreases with time since this model mismatch is captured in the estimation. An interesting thing is the increase in friction that is clearly seen at the end of slip. Figure 5.4 shows the position signal in zoom, and there we clearly can see the presliding displacement.

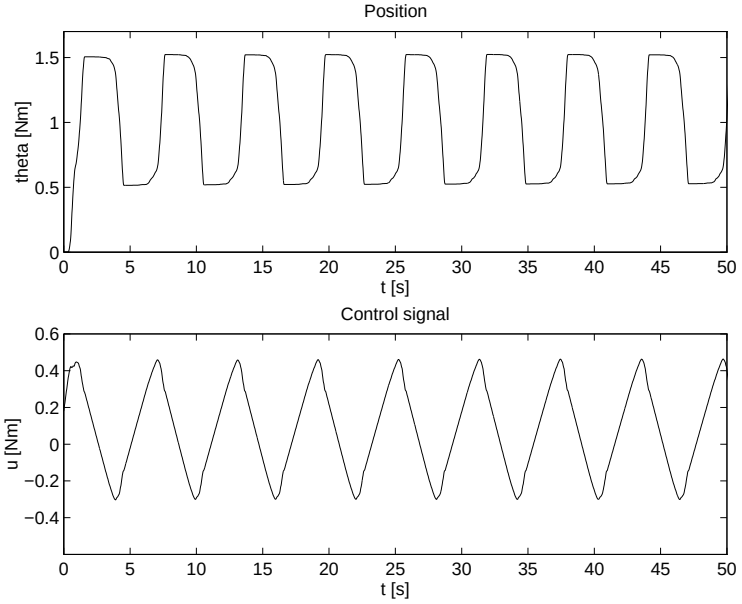

Figure 5.2 Limit cycle from experiments. Upper: Position versus time. Lower: Control signal versus time.

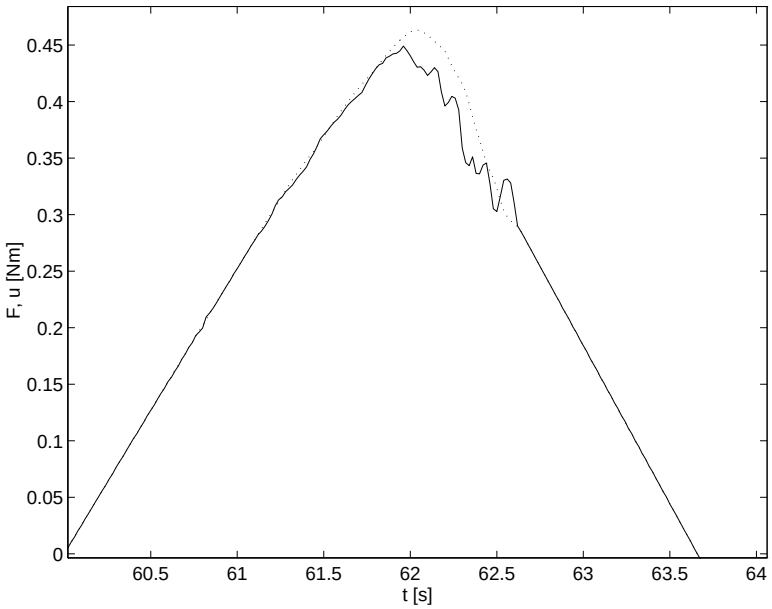

Figure 5.3 Half-period of limit cycle from experiments. Solid: Estimated non-linear friction term. Dotted: Control signal.

5.2 Simulation

Simulations are done on the model of the experimental setup shown in figure C.2. Since the experimental limit cycle above suggests an asymmetric friction we use asymmetric friction models for the simulations. Parameters are chosen to fit experiments. The Lugre and Bliman & Sorine model parameters are taken from the results in chapter 4 in the section on wet identification,

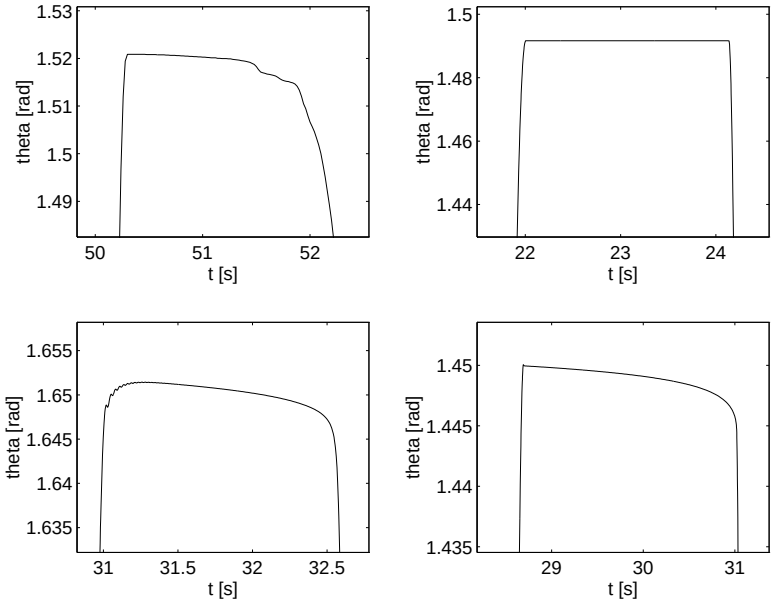

Figure 5.4 Pre-sliding displacement. From upper left: experimental, classical model, Bliman & Sorine model, Lugre model.

but are modified here to best fit observations. The PID regulator is the same as above, i.e. the parameters are given by table 5.2.

Classical friction model

First simulations is carried out for a classical friction model. A static model with stiction τ_s, kinetic friction τ_k and viscous friction α is used with parameters as given by table 5.3. Figure 5.5 shows the resulting limit cycle. We see

	τ_s [Nm]	τ_k [Nm]	α [Nms/rad]
$-$	0.30	0.14	0.017
$+$	0.46	0.30	0.017

Table 5.3 Static friction model parameters.

that just as for the experimental limit cycle we have symmetry in position, but asymmetry in control signal. The classical model does not model pre-sliding displacement, hence this is not present in the result. The transient is slightly different, but overall the limit cycle is well reproduced by a classical model. In figure 5.6 a half-period of the control signal and the non-linear friction torque of the limit cycle is shown in zoom. Figure 5.4 shows the position signal in zoom, and we see that there is no pre-sliding displacement for the classical model.

Bliman friction model

For the Bliman & Sorine model the identification parameters of table 5.4 is used, yielding the model parameters of table 5.5. Note that we have chosen a pre-sliding displacement $s_e \approx 5$ mrad, and therefore $s_p = 20$ mrad $> 3s_p$. Figure 5.7 shows the resulting limit cycle. We see that the limit cycle is

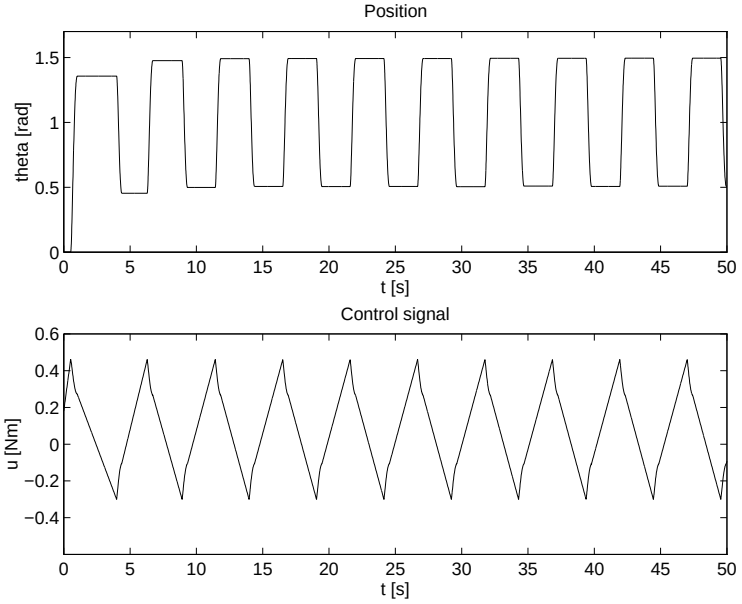

Figure 5.5 Limit cycle from simulation with classical friction model. Upper: Position versus time. Lower: Control signal versus time.

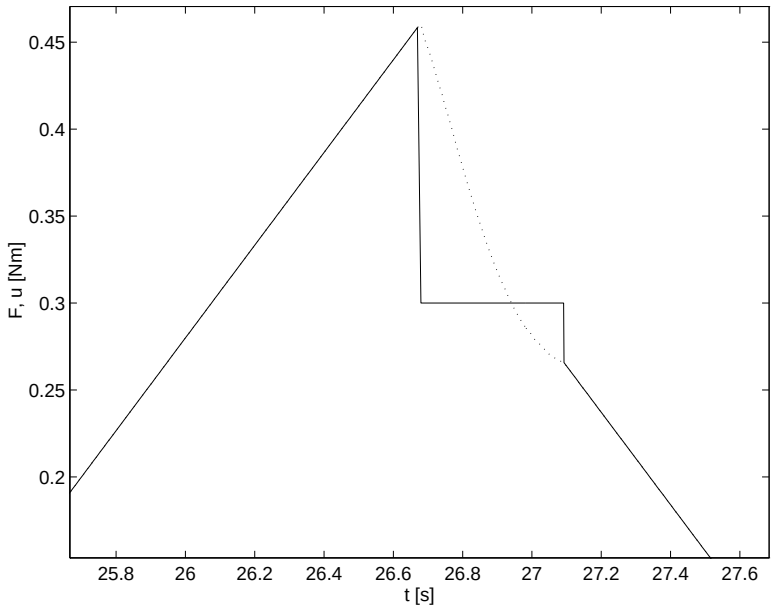

Figure 5.6 Half-period of limit cycle from simulation with classical friction model. Solid: Estimated non-linear friction term. Dotted: Control signal.

asymmetric in position and in control signal. The reason for this is that the model response does not agree with what is demanded by the identification parameters. We demand a stiction force of 0.46 Nm for $v < 0$, but obtain 0.47 Nm, 0.30 Nm for $v > 0$, but obtain 0.27 Nm. A condition for the limit cycle to be symmetric in position is that the difference of the static and kinetic friction is equal in both directions. This is fulfilled for the identification parameters, where the difference is 0.16 Nm. This is not fulfilled in the obtained model

	f_s [Nm]	f_k [Nm]	s_e [rad]	s_p [rad]
−	0.30	0.14	0.005	0.002
+	0.46	0.30	0.005	0.002

Table 5.4 Bliman & Sorine identification parameters.

	f_1 [Nm]	f_2 [Nm]	ε_f	η	α [Nms/rad]
−	0.39	0.25	0.0067	0.32	0.017
+	0.53	0.23	0.0067	0.25	0.017

Table 5.5 Bliman & Sorine model parameters.

response though. This problem, that the Bliman & Sorine model does not always give the response demanded by the identification parameters, is also discussed in section 2.8. Pre-sliding displacement is present in the simulated limit cycle, as expected. Note that the first break-away torque is lower than the succeeding. Figure 5.8, where a half-period of the control signal and the

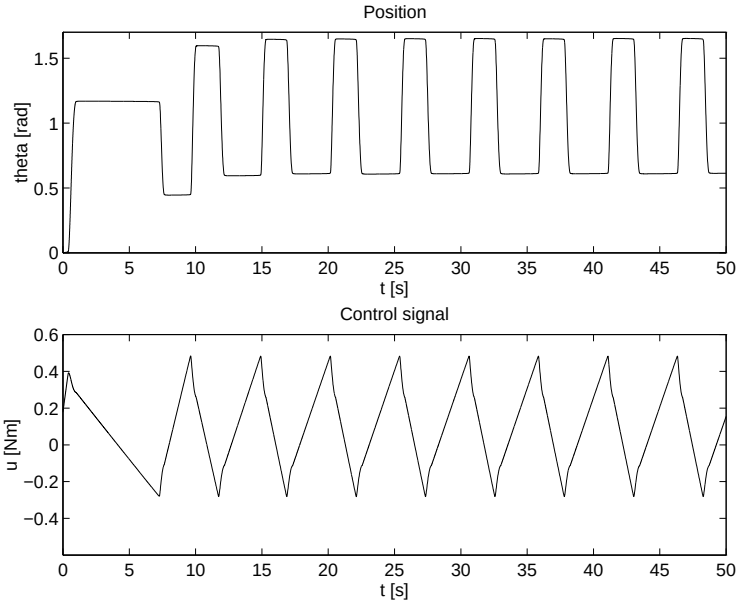

Figure 5.7 Limit cycle from simulation with Bliman & Sorine friction model. Upper: Position versus time. Lower: Control signal versus time.

non-linear friction is plotted, is essentially the same as figure 5.6, except for the oscillations. The reason for the oscillations is due to the linearized model equations, and is discussed in section 2.9. The oscillations give lower break-away force than expected from the identification parameters. The peak at the transition from slip to stick found experimentally in figure 5.3 is not captured by the Bliman & Sorine model. Figure 5.4 shows the position signal in zoom. It seems the transition from slip to stick is not as abrupt as for the experimental limit cycle. Also this is due to the oscillations in the friction torque. The pre-sliding displacement is nicely modeled though.

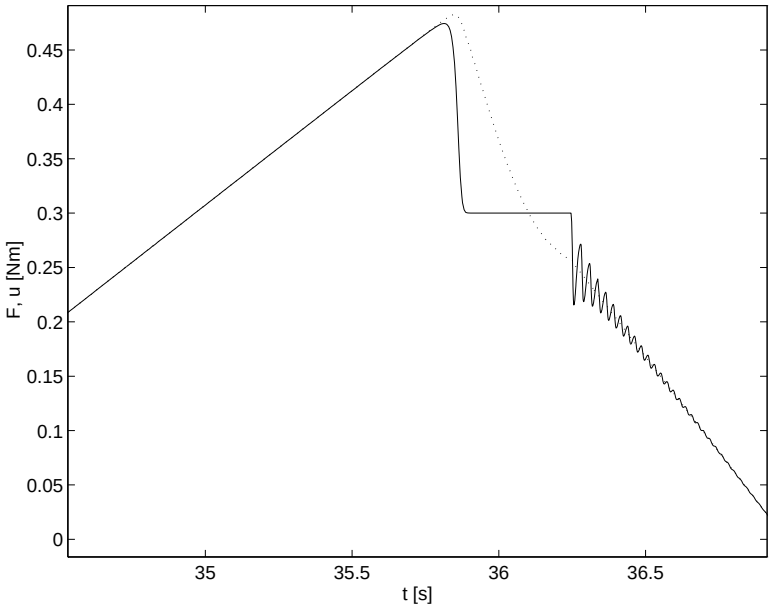

Figure 5.8 Half-period of limit cycle from simulation with Bliman & Sorine friction model. Solid: Estimated non-linear friction term. Dotted: Control signal.

Lugre friction model

The parameters of table 5.6 is used. In figure 5.9 we see the limit cycle. It is

	σ_0 [Nm/rad]	σ_1 [Nms/rad]	v_0 [rad/s]	α_0 [Nm]	α_1 [Nm]	α_2 [Nms/rad]
$-$	280	1	0.1	0.14	0.16	0.017
$+$	280	1	0.1	0.30	0.16	0.017

Table 5.6 Lugre model parameters.

symmetric in position and asymmetric in control signal, just as the experimental limit cycle. According to property 3.1 the pre-sliding displacement should be approximately 2 mrad and 4 mrad in the different directions. We have a pre-sliding displacement of the predicted magnitude (can be seen when zooming in the figure). Figure 5.10, that shows a half-period of the control signal and the non-linear friction torque, shows that we have the increase in friction force observed experimentally at the transition from slip to stick. Figure 5.4 shows the position signal in zoom. The Lugre model shows the best agreement with experimental results. The transition from slip to stick is abrupt as in the experimental case. Also the pre-sliding displacement is correctly modeled.

5.3 The describing function

The describing function analysis *DFA* applied here is that of a single sinusoid input describing function [3]. In this approach it is assumed that the system can be divided into one linear, $H(s)$, and one non-linear part, $\Psi(\cdot)$, and that the limit cycle found in the input signal to the non-linear element has a waveform close to a harmonic signal with zero mean. See figure 5.11.

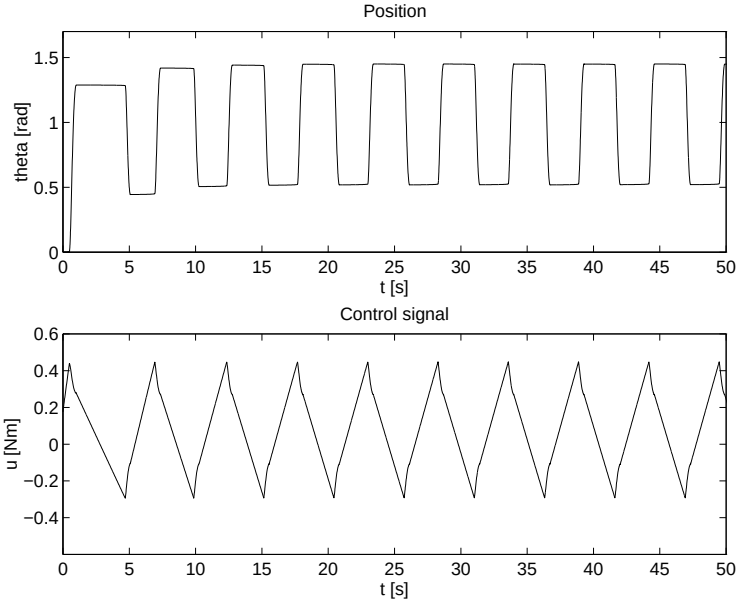

Figure 5.9 Limit cycle from simulation with Lugre friction model. Upper: Position versus time. Lower: Control signal versus time.

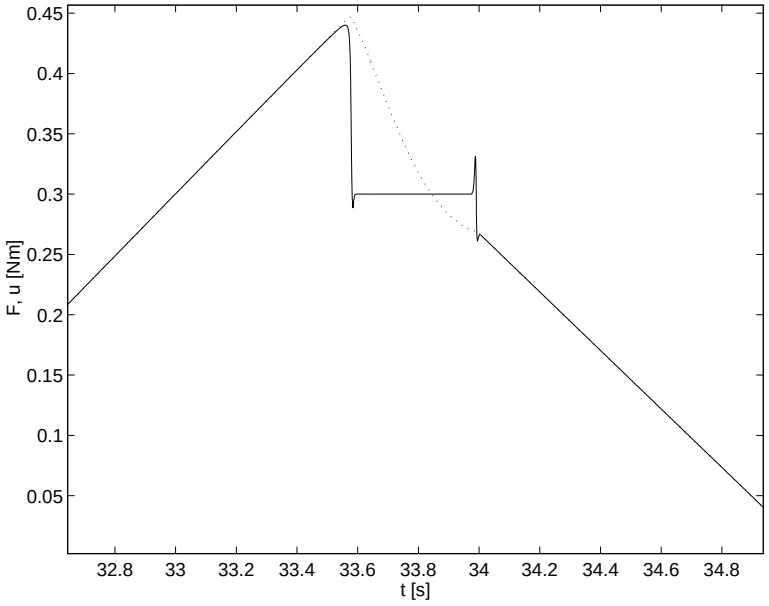

Figure 5.10 Half-period of limit cycle from simulation with Lugre friction model. Solid: Estimated non-linear friction term. Dotted: Control signal.

For the DF analysis set $r \equiv 0$. Assume $x(t) = a \sin\theta$, where we have introduced the variable $\theta = \omega t$. Note that y is a periodic signal in presence of a limit cycle, and therefor can be expanded in a Fourier series,

$$y(\theta) = \sum_{s=0}^{\infty} a_s \cos s\theta + b_s \sin s\theta, \tag{5.7}$$

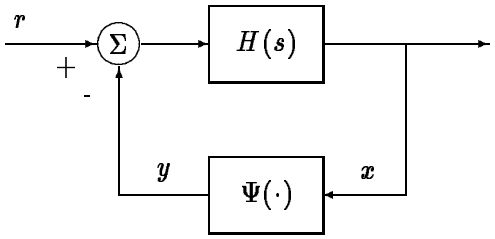

Figure 5.11 General system decomposition for describing function analysis.

with

$$\begin{cases} a_s &= \frac{\epsilon_s}{2\pi}\int_{-\pi}^{\pi} y(\theta)\cos s\theta d\theta, \\ b_s &= \frac{1}{\pi}\int_{-\pi}^{\pi} y(\theta)\sin s\theta d\theta. \end{cases} \tag{5.8}$$

$\epsilon_s = 0$ for $s = 0$,$\epsilon_s = 2$ for $s > 0$. The describing function $N(a,\omega)$ is defined as the complex ratio of the fundamental component of the output to the sinusoidal input. The fundamental output from the nonlinearity is $a_1\cos\theta + b_1\sin\theta$, which means the DF is given by

$$N(a,\omega) = \frac{b_1 + ja_1}{a}. \tag{5.9}$$

Self sustaining harmonic oscillations with frequency ω and amplitude a requires that

$$H(i\omega)N(a,\omega) = -1.$$

Thus by plotting $H(i\omega)$ against $-1/N(a,\omega)$ in a Nyquist diagram and look for intersections we can predict limit cycles. Remember though that the assuptions made are quite strong, that the nonlinearity output can be approximated by the first harmonic of it's Fourier series expansion, and that the input can be regarded as harmonic.

For the dynamic nonlinearity introduced by the Bliman & Sorine model (2.7) the Lugre model (3.4) the DF $N(a,\omega)$ becomes dependent of both amplitude a and frequency ω. Moreover the DF cannot be evaluated analytically because of the complexity of the model. Instead numerical integration of the model with sinusoidal input is carried out, which gives the fourier coefficients (5.8) of the output fundamental, which then are used in (5.9) to compute $N(a,\omega)$.

For a DF dependent only on A it is not so important to have very accurate values of $N(A)$ since one easily can see if there exist a intersection in the Nyquist diagram, and thus if there exist a limit cycle or not. For a DF on the form $N(A,\omega)$ the way of finding intersections depend on the directions of the curve set $\{N(a,\Omega)|a \in \mathbb{R}, \Omega \text{ fixed}\}$ with respect to Ω, and the direction of $H(i\omega)$. Attention has to be payed when interpreting the Nyquist plot. It is not always clear that a intersection really takes place.

Some different approaches to the DF analysis will be tried. Normally the system decomposition is done so that the nonlinearity is isolated as much as possible in one part, and the rest, being all linear, as the other. When doing analytical calculations of the DF this approach is natural, since no dynamics are wanted in the nonlinear part then. When computing the DF numerically we are not bounded by this. Other conciderations can be done though.

The DF analysis will be made for the classical friction model, the Bliman & Sorine model and the Lugre model used in the limit cycle simultions above. Since we use a single sinusoid input DF approach we assume a symmetric limit cycle in the analysis. Therefore we will use symmetric friction models. The parameters are given in tables 5.7, 5.8, 5.9 and 5.10. The parameters are chosen to give limit cycles with the same symmetric position amplitude as in the experimental case.

τ_s [Nm]	τ_k [Nm]	α [Nms/rad]
0.38	0.22	0.017

Table 5.7 Static friction model parameters.

f_s [Nm]	f_k [Nm]	s_e [rad]	s_p [rad]
0.38	0.22	0.005	0.002

Table 5.8 Bliman & Sorine identification parameters.

f_1 [Nm]	f_2 [Nm]	ε_f	η	α [Nms/rad]
0.45	0.23	0.0067	0.28	0.017

Table 5.9 Bliman & Sorine model parameters.

Simulations of these symmetric friction models and the model of figure 5.1 with the PID parameters of table 5.2 give limit cycles with properties shown in table 5.11.

First approach

First we look at the standard decomposition, see figure 5.12, and notice that the input signal to the nonlinearity becomes the velocity. The velocity signal in a stick-slip limit cycle has the form of an impulse train. Recall the assumption made in the DF analysis, that the input signal can be approximated by the first harmonic of it's Fourier series expansion. The Fourier coefficients b_n of the impulse train are not decreasing with n. The DF analysis does not look promising for this decomposition in other words. It will be carried out though, for comparison. The Nyquist plot of the linear part of this decomposition is shown in figure 5.13.

Classical model Since the classical model apart from the velocity also requires the externally applied torque as input, and thus cannot be regarded as a single input model, this approach is not possible to use.

Bliman & Sorine model In figure 5.14 we see the describing function for the Bliman & Sorine model. The accuracy is best for small amplitudes. The Bliman & Sorine model is rate independent and only depends on the absolute relative displacement s, and this might give the idea that also the DF should

σ_0 [Nm/rad]	σ_1 [Nms/rad]	v_0 [rad/s]	α_0 [Nm]	α_1 [Nm]	α_2 [Nms/rad]
280	1	0.1	0.22	0.17	0.017

Table 5.10 Lugre model parameters.

	T [s]	ω [rad/s]	a_θ [rad]	a_ω [rad/s]
Experimental	6.16	1.0	0.52	1.75/2.25
Classical	5.1	1.2	0.50	3.9
Bliman & Sorine	4.9	1.3	0.52	4.1
Lugre	5.1	1.2	0.49	3.9

Table 5.11 Limit cycle properties from experiment and simulations. T is period, ω angular frequency, a_θ position amplitude and a_ω velocity amplitude.

be rate independent. This is not the case however. Since the input $x = a \sin \omega t$ to the DF is the velocity, we have that the the displacement is $\int a \sin \omega t \, dt$, and the amplitude of this is a/ω, which is rate dependent. The true limit cycle from simulation of the system has the frequency $\omega = 1.3$ rad/s and $a_\omega = 4.1$ rad/s. From figure 5.15 we see that no intersection between the negative inverse of the describing function and the linear Nyquist plot is found.

Lugre model In figure 5.16 we see the describing function for the Lugre model. The true limit cycle from simulation of the system has the frequency $\omega = 1.2$ rad/s and $a_\omega = 3.9$ rad/s. From figure 5.17 we see that no intersection between the negative inverse of the describing function and the linear Nyquist plot is found.

Second approach

A possible modification of the above is to introduce a derivative block as in figure 5.18, and carry out the decomposition as indicated. This gives two advantages: the position becomes the input to the nonlinear block. The position signal is pretty much like a square wave, and therefor better fulfills the assumptions made for the DF analysis. The square wave has Fourier coefficients b_n which are proportional to $1/n$. The other advantage is that we get the error amplitude of the limit cycle from the DF analysis instead of the velocity amplitude, which is not that interesting. Another way of looking at this is to say that we just rotate the Nyquist curves $\pi/2$ rad, and there is no reason this should increase the quality of the analysis. What is the correct way of thinking? Even if the quality would not be better compared to the first approach we still have a more interesting signal as nonlinearity input. In computing the describing functions for the Bliman & Sorine and the Lugre model the results were the same as for approach one, except that the plots were rotated $\pi/2$ rad. Therefore the results are not presented here, and we carry on to the next approach.

Third approach

There exist another signal in the system which is even better suited as input signal to the nonlinearity of a DF analysis, the control signal. The decomposition we look at now is given in figure 5.19. The control signal looks like

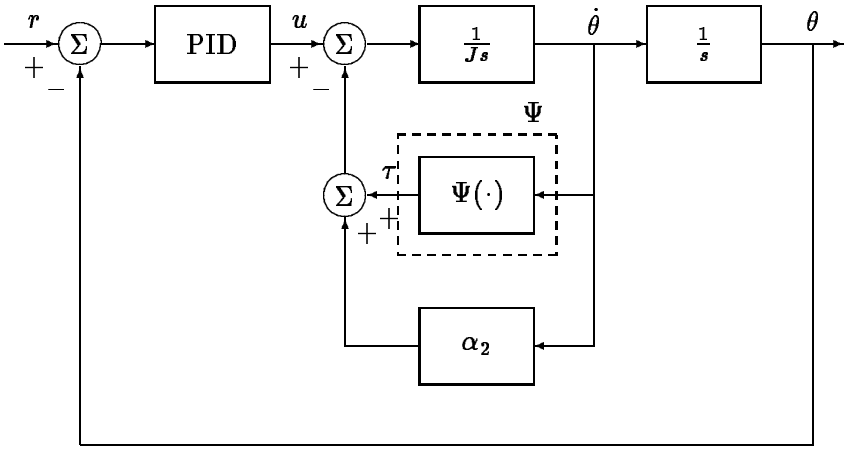

Figure 5.12 System decomposition for describing function analyasis, first approach.

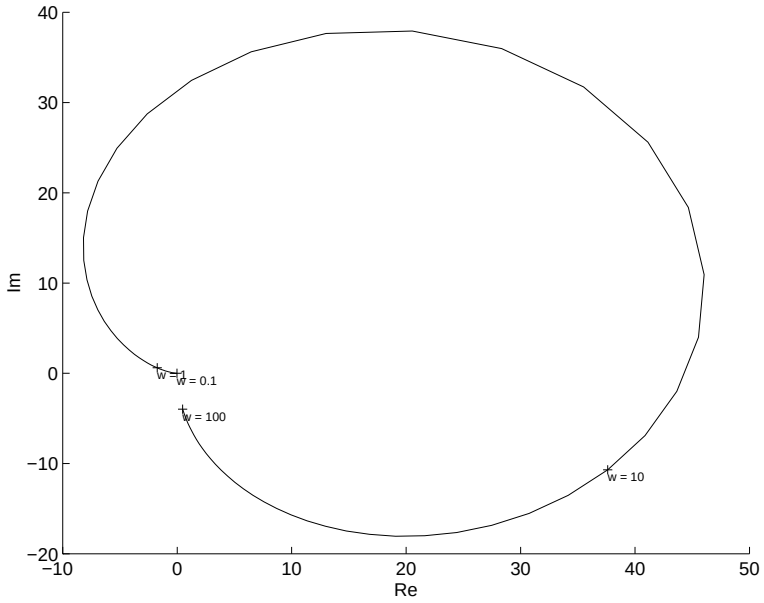

Figure 5.13 Nyquist plot of the linear part, first approach.

a triangle wave, which has Fourier coefficients b_n which are proportional to $1/n^2$.

The disadvantage of this decomposition is that the the amplitude of the control signal probably already is known since it is the break-away force. Moreover it is exactly the same for all limit cycles since the break-away force is constant, or at least almost exactly depending on if there exist a rate dependency in the break-away force, i.e. if the break-away varies with limit cycle frequency.

The Nyquist plot of the linear part of this decomposition is shown in figure 5.20. This approach was successfully used in [4] together with the Karnopp model.

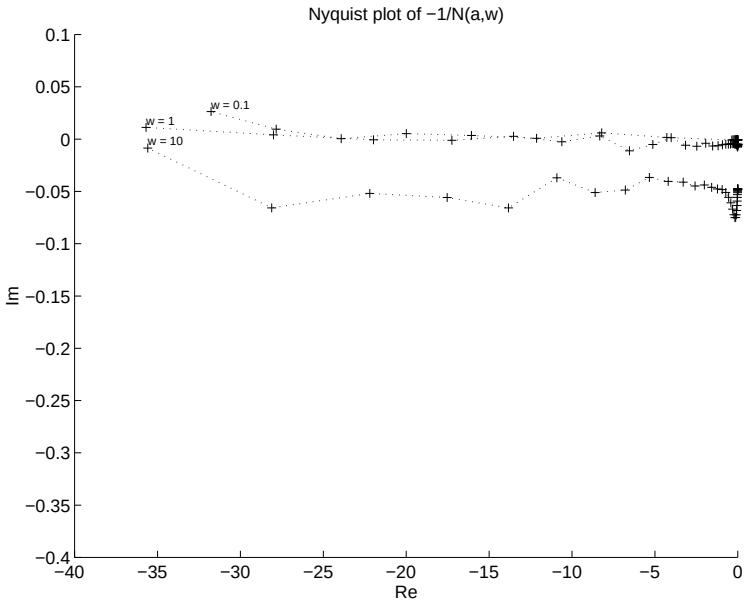

Figure 5.14 Negative inverse of the describing function for the Bliman & Sorine model, first approach. The DF $N(a,\omega)$ is evaluated for $\omega \in \{0.1,\ 1.0,\ 10\}$ rad/s and $\log(a) \in [-4,\ 1]$ rad/s. The amplitude a is increasing from right to left.

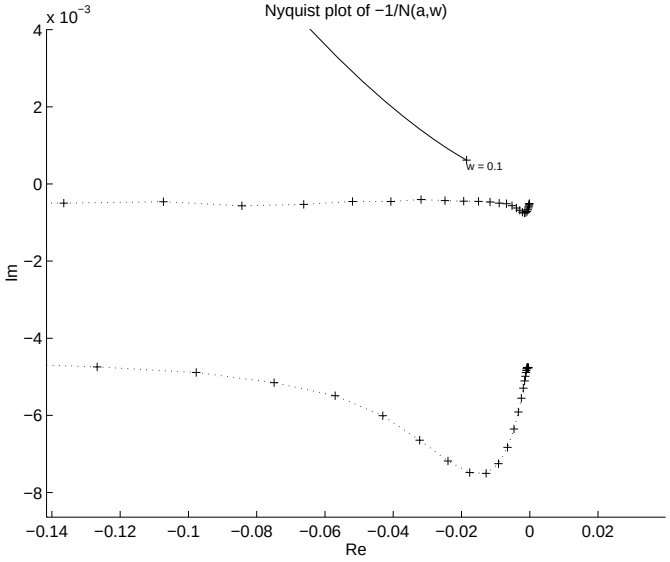

Figure 5.15 Nyquist plot of linear part and Bliman & Sorine describing function, first approach . No intersection.

Classical model In figure 5.21 we see the DF for the Classical model in the third decomposition, together with the linear part. The amplitude is increasing to the left. Since the classical model does not have any pre-sliding displacement for input torques the describing function $N(a,\omega)$ is zero for these inputs. That means the negative inverse is infinite. At break-away the system is discontinuous, and so the DF is discontinuous.

The DF is computed as near the discontinuity at break-away as possible

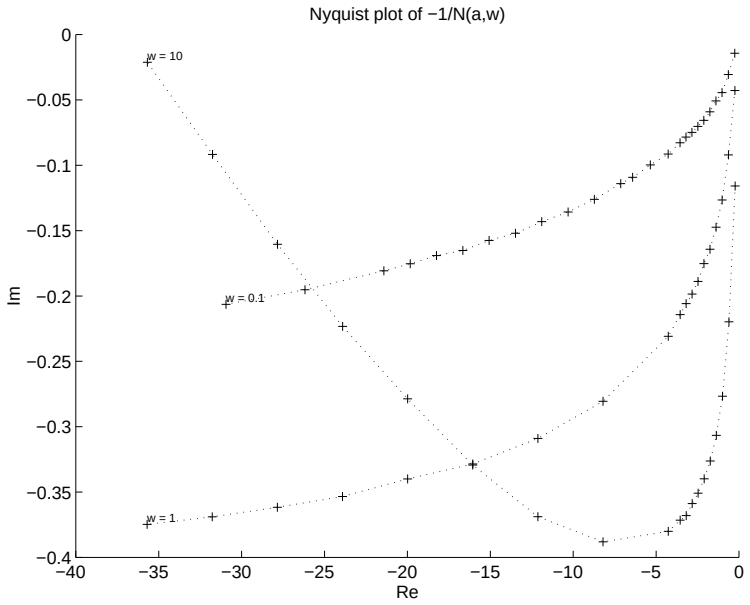

Figure 5.16 Negative inverse of the describing function for the Lugre model, first approach. The DF $N(a,\omega)$ is evaluated for $\omega \in \{0.1, 1.0, 10\}$ rad/s and $a \in [0.1, 10]$ rad/s. The amplitude a is increasing from right to left.

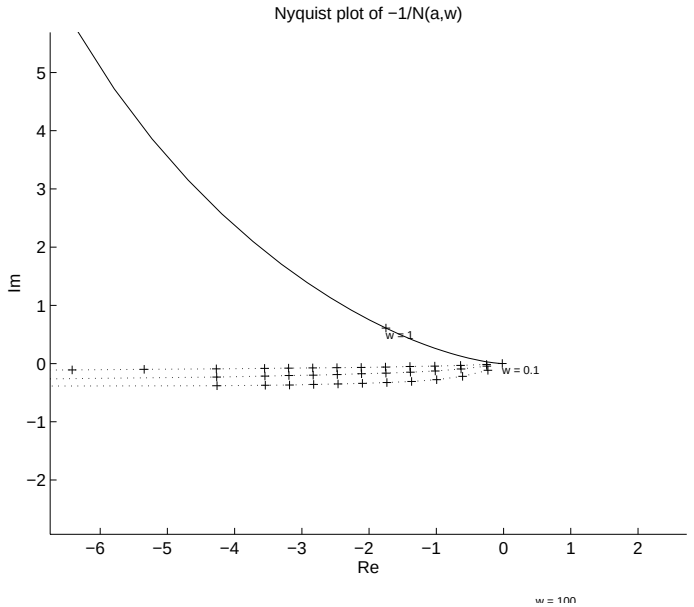

Figure 5.17 Nyquist plot of linear part and Lugre describing function, first approach. No intersection.

within the numerical limits of the integration routines. Still we can not get an intersection between $-1/N(a,\omega)$ and the linear part. If there was an intersection it would be at break-away, since the amplitude of the control signal in a limit cycle is the break-away force, and thus the discontinuity would be exactly at the intersection. Numerically it is difficult to compute $N(a,\omega)$ close to the discontinuity though. Other frequencies are also tried but an intersection is not found.

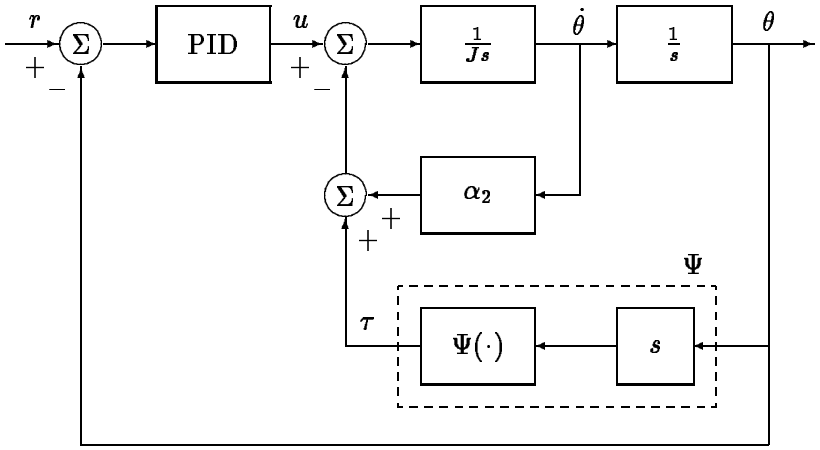

Figure 5.18 System decomposition for describing function analyasis, second approach.

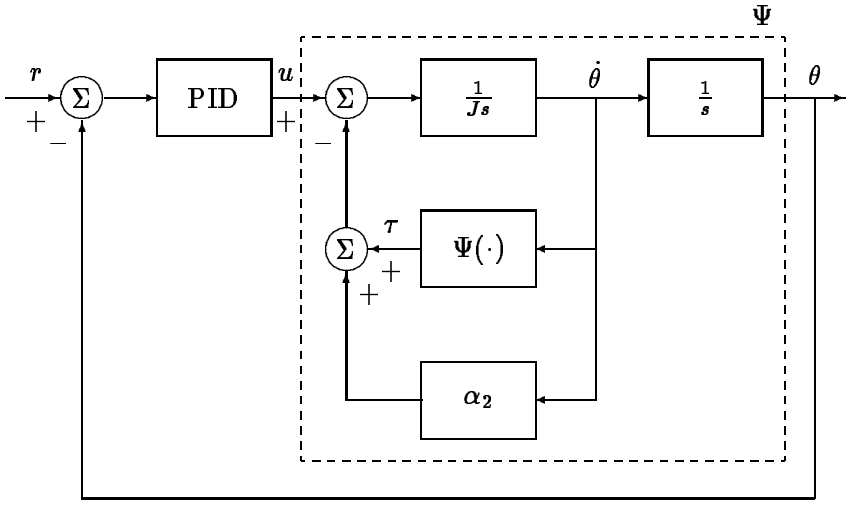

Figure 5.19 System decomposition for describing function analyasis, third approach.

Bliman & Sorine model In figure 5.22 we see the DF for the Bliman & Sorine model in the third decomposition. The amplitude is increasing from the left. We have gaps in which the DF is difficult to compute due to precision limits in the integration routines. The gaps correspond to break-away regions. While the model is not discontinuous at break-away, the describing function almost is, and it is required very high precision to resolve this region. The visible area in this plot corresponds to pre-sliding displacement. For the classical model this part of $-1/N(a,\omega)$ was found at infinity. The part of the curve $-1/N(a,\omega)$ corresponding to motion at, and after break-away is found in the upper right corner. While for the Lugre model there is one gap, or discontinuity, see below, for each curve $-1/N(a,\Omega)$, Ω fixed, for the Bliman & Sorine model there are two. This is due to the phenomenon described in section 2.9 where it is shown thet a symmetric torque input can give an asymmetric position output with break-away only in one direction. I.e. in the

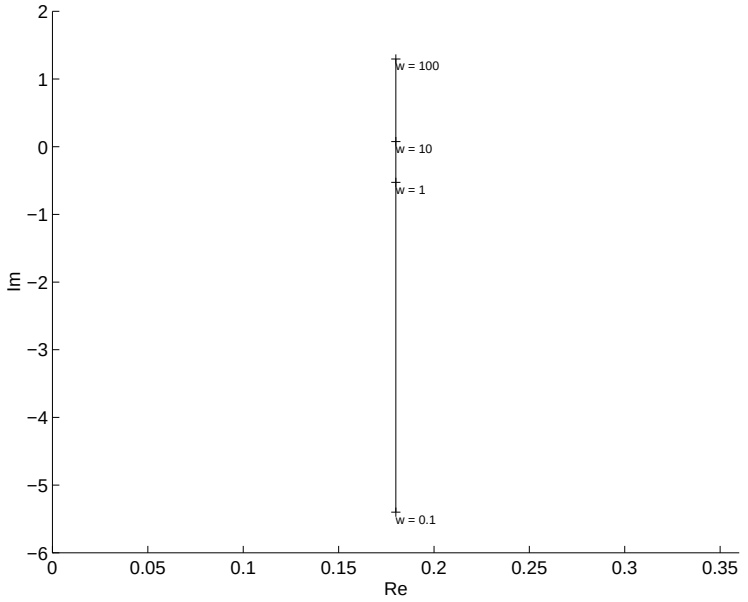

Figure 5.20 Nyquist plot of the linear part, third approach.

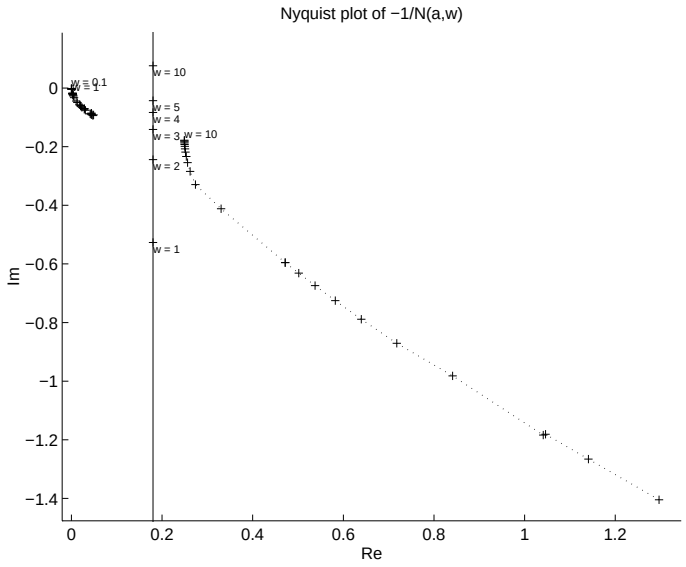

Figure 5.21 Negative inverse of the describing function for the Classical model, third approach. The DF $N(a,\omega)$ is evaluated for $\omega \in \{0.1, 1.0, 10\}$ rad/s and $\log(a) \in [-3, 1]$ rad/s. The amplitude a is increasing from left to right.

describing funtion in the third approach the Bliman & Sorine model exhibits two discontinuities. One for the first break-away only in one direction, and another when break-away is acheived in both directions. The amplitude region for which the motion exhibits break-away only in one direction is approximately 0.30 – 0.37 Nm. Not very large but still significant, and the region in $N(a,\omega)$ corresponding to this interval is quite large.

In the figure the end part of the DF is found in the upper right corner for

all frequencies. The amplitude difference in the gap region is less than 10^{-12} Nm, still the gap is fairly large. The DF is computed as far as possible within the numerical limits of the integration routines. In figure 5.23 the region after break-away is zoomed. The linear part of the system is also plotted. The second discontinuity for the curve $-1/N(a, 1.0)$ is seen. It is difficult to analyze intersections in this plot though. In search for an intersection we plot

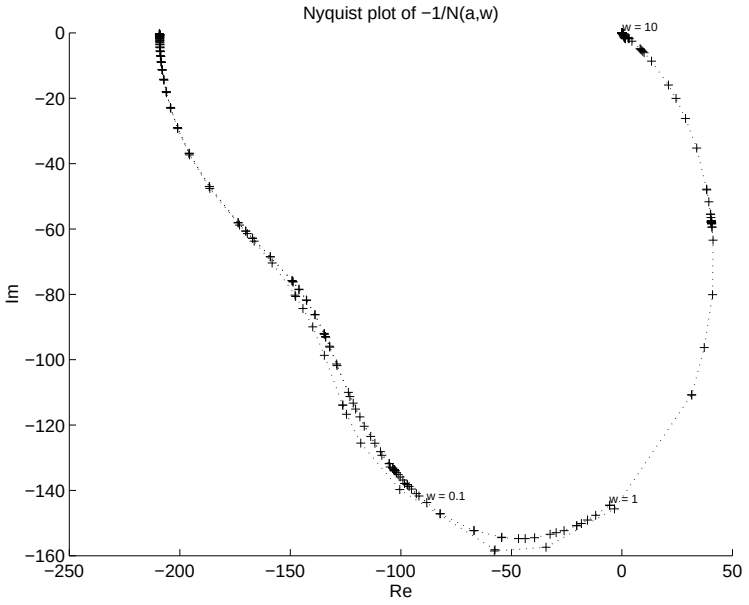

Figure 5.22 Negative inverse of the describing function for the Bliman & Sorine model, third approach. The DF $N(a, \omega)$ is evaluated for $\omega \in \{0.1, 1.0, 10\}$ rad/s and $\log(a) \in [-3, 1]$ rad/s. The amplitude a is increasing from left to right. There are gaps in which the DF could not be computed due to limits in precision.

$\omega \in \{1.8, 1.9, 2.0\}$ rad/s. In figure 5.24 we can see that an intersection exists at $\omega = 1.9$ rad/s. The corresponding amplitude is 0.36 Nm. Here the discontinuities at full break-away in both directions are clearly seen. The amplitude in the simulation is 0.38 Nm, and the frequency is 1.3 rad/s. Thus the DF fairly good predicts the amplitude, and fairly good predicts the frequency of the limit cycle.

Lugre model In figure 5.25 we see the DF for the Lugre model in this decomposition. The amplitude is increasing from the left. There are gaps in which the DF is difficult to compute due to precision limits in the integration routines. The gaps correspond to the regions near break-away, and there seem to be discontinuities at break-away as for the Bliman & Sorine model though the model is not discontinuous. Probably what seem to be discontinuities are just regions in which very high precision is required to resolve the describing function. In the figure the part of the DF corresponding to motion after and at break-away is found in the upper right corner for all frequencies. The amplitude difference in the gap region is less than 10^{-12} Nm, still the gap is fairly large. The DF is computed as far as possible within the numerical limits of the integration routines. In figure 5.26 the region after break-away is zoomed. The linear part of the system is also plotted. We see that the precision was not enough to compute the DF close to the linear Nyquist plot for the given frequencies. Since the frequency of the simulated system is $\omega = 1.2$

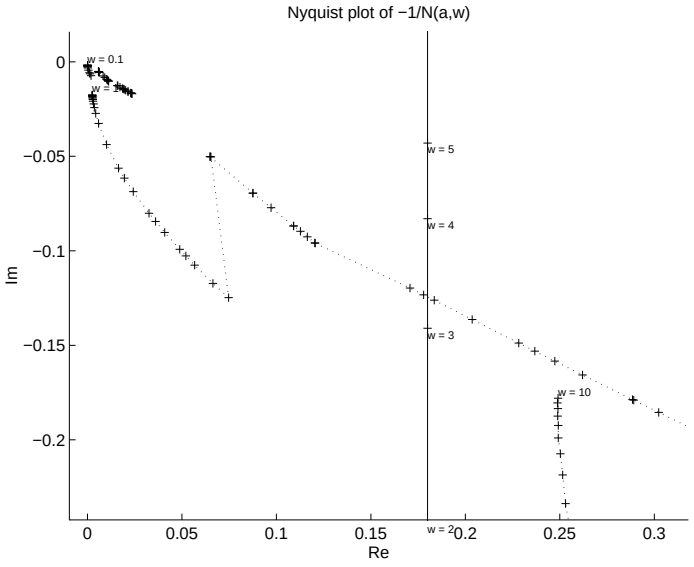

Figure 5.23 Zoom on the upper right part of figure 5.22. The linear part is also plotted to check for intersections.

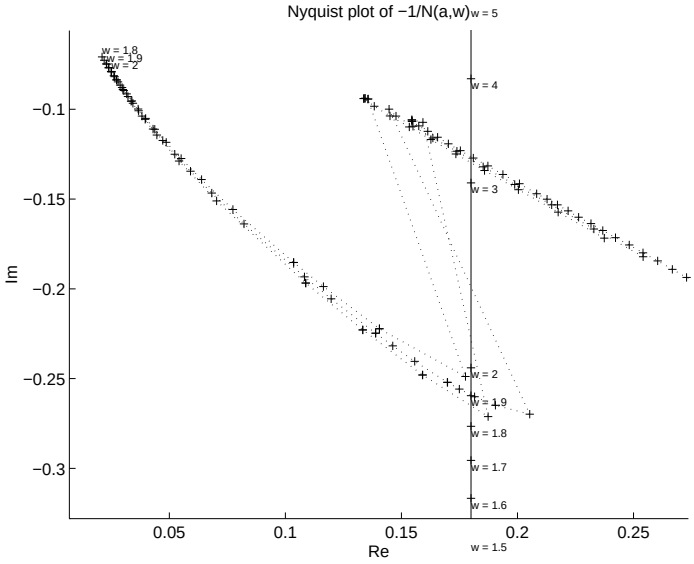

Figure 5.24 Negative inverse of the describing function for the Bliman & Sorine model, and the linear part, third approach. Zoom in the intersection area, like in figure 5.23. The DF $N(a,\omega)$ is evaluated for $\omega \in \{1.8, 1.9, 2.0\}$ rad/s and $a \approx 0.36$ rad/s. Intersections are found.

rad/s we try to compute the DF for $\omega = 1.5$ rad/s, to see if we now can get an intersection. The result is shown in figure 5.27, where we see that an intersection exists, however not at the correct frequency. The DF is computed for a second frequecy $\omega = 2.0$ rad/s which gives a second intersection, quite close in frequency. We have now captured a true intersection with correct frequency between these intersections. This is true since the intersection of

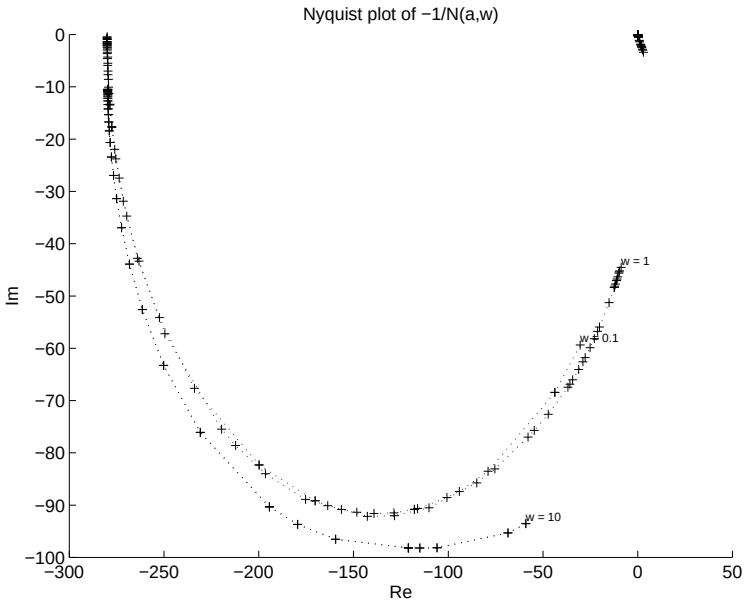

Figure 5.25 Negative inverse of the describing function for the Lugre model, third approach. The DF $N(a,\omega)$ is evaluated for $\omega \in \{0.1, 1.0, 10\}$ rad/s and $\log(a) \in [-3, 1]$ rad/s. The amplitude a is increasing from left to right. There are gaps in which the DF could not be computed due to limits in precision.

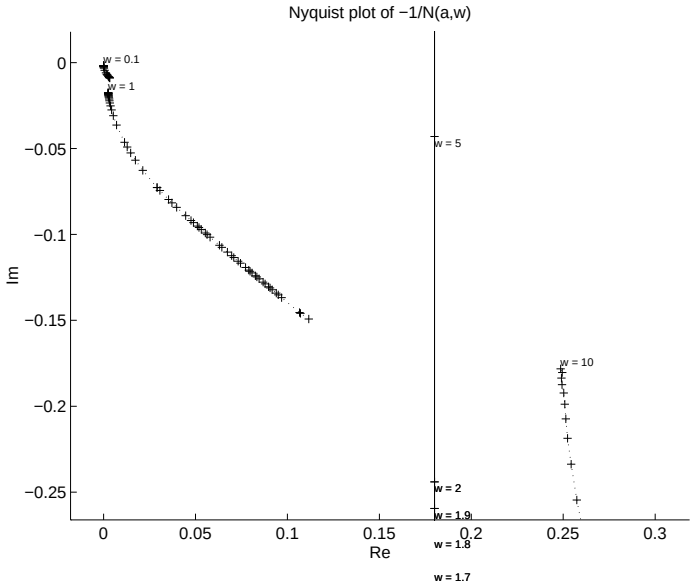

Figure 5.26 Zoom on the upper right part of figure 5.25. The linear part is also plotted to check for intersections.

$-1/N(a, 1.5)$ and $G(i\omega)$ above $G(i1.5)$, and the intersection of $-1/N(1, 2.0)$ lies below $G(i2.0)$. We can say then that there is an intersection with frequency $\omega \in [1.5, 2.0]$ rad/s, and amplitude $a \in [0.3809, 0,3831]$ Nm. The amplitude in the simulation is 0.38 Nm. Thus DF can correctly predict the amplitude, and fairly good predict the frequency of a limit cycle.

From the describing function of the Lugre model the rate dependency of

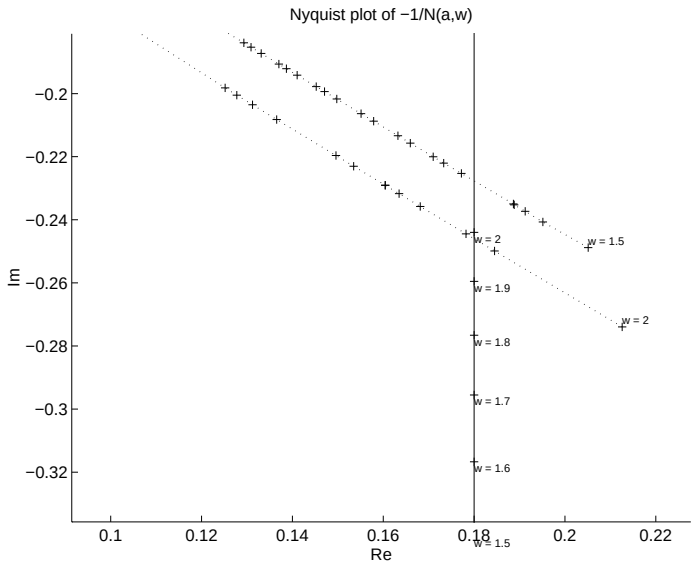

Figure 5.27 Negative inverse of the describing function for the Lugre model, and the linear part, third approach. Zoom in the intersection area, like in figure 5.26. The DF $N(a, \omega)$ is evaluated for $\omega \in \{1.5, 2.0\}$ rad/s and $a \approx 0.38$ rad/s. Intersections are found.

the break-away force is clearly seen in that the amplitude at the gap limits corresponding to break-away change with frequency. We have $a = 0.390$, Nm $a = 0.385$ Nm and $a = 0.349$ Nm, for $\omega = 0.1$ rad, $\omega = 1.0$ rad/s and $\omega = 10$ rad/s respectively.

5.4 Heuristic limit cycle prediction

In this section friction is approximated by a static friction model with static, kinetic and viscous friction. The impact of the pre-sliding displacement on existence of limit cycles is discussed. The pre-sliding displacement is a property of dynamic friction models, therefore we may expect that these models behave qualitatively different than the static models when limit cycles are present.

By some simple heuristic reasoning it is possible to predict error amplitude and period of limit cycles in the system of figure 5.1 with quite good accuracy. The limit cycles in this system are due to the stick-slip behaviour of the friction. While in stick an external torque of the magnitude of the stiction torque τ_s, is required to get a transition to slip. I.e. when the control signal reaches this torque τ_s the shaft will move until stick is reached again. Then it will stay in stick until the break-away force is reached again, and so on. It is clear that all friction induced limit cycles will have the same amplitude in control signal a_u, since the break-away force is constant for all choices of PID parameters. This is true if the limit cycle periods are of the same magnitude. If the period varies greatly, the phenomenon of rate dependent break-away torque may be significant.

The interesting properties of the limit cycles from a control point of view are the amplitude of the position error, a_e, and the period T. The dependency

of the PI parameters for these properties can be explained roughly as follows: The proportional part, $u_p = k_p e$, will bring down the position error to a certain level until $k_p e \lesssim \tau_s$, then the integral part will grow until $u_p + u_i > \tau_s$ and slip occurs. The derivative part k_d has influence only during the slip phase of the limit cycle.

In the following we will assume a symmetric friction model with stiction torque τ_s, which can be easily detected experimentally by finding one limit cycle and measure the amplitude of the control signal, and the kinetic friction τ_k. In figure 5.28 the signal forms of a steady state limit cycle are shown. The control signal u is composed of one proportional part u_p, one integral part u_i and the derivative part u_d. The action of these parts respectively in the different phases of a cycle can be seen from the picture.

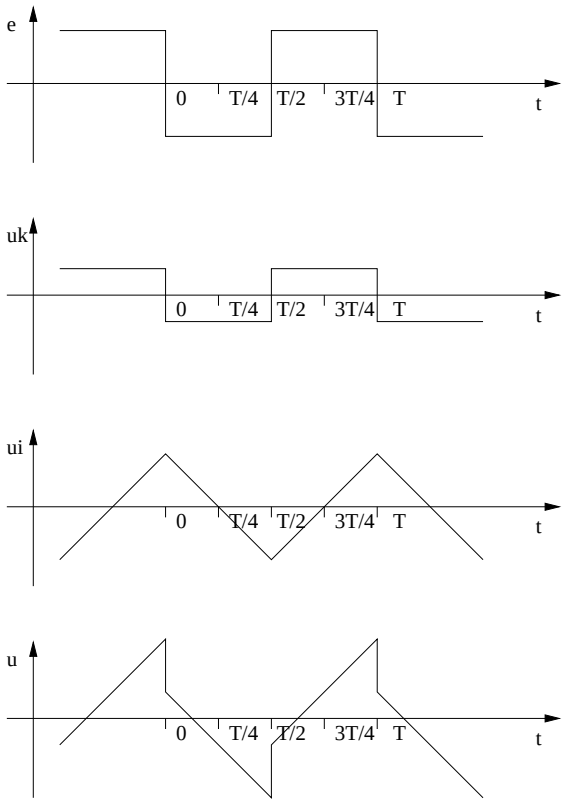

Figure 5.28 Signal forms in a friction induced limit cycle.

Symmetric static friction + PID control

We will in this section find an approximate expression for error amplitude a_e, and period T in a symmetric limit cycle around a zero setpoint.

With a PID regulator with parameters k_p and k_i a transition from stick to slip will occur when

$$u_p + u_i = \tau_s, \tag{5.10}$$

which gives the following equation

$$k_i \int_0^{T/2} a_e dt + 2k_p a_e = 2\tau_s.$$

Solving for T gives

$$T = \frac{4}{k_i a_e}\left(\tau_s - k_p a_e\right). \tag{5.11}$$

I.e. if we know the error amplitude a_e we can get the limit cycle period from (5.11). How can we find the error amplitude then? We start by regarding the force equation of the system. The forces acting on the system are those of the controller and the friction,

$$J\ddot{\theta} = u_p + u_i - \tau.$$

We make here the assumtion that the friction force during the slip period is equal to τ_k. Moreover we neglect the viscous friction term and the derivative action, see figure 5.29. The approximations may seem restrictive. How valid they are will be seen when comparisons with simulations are made later.

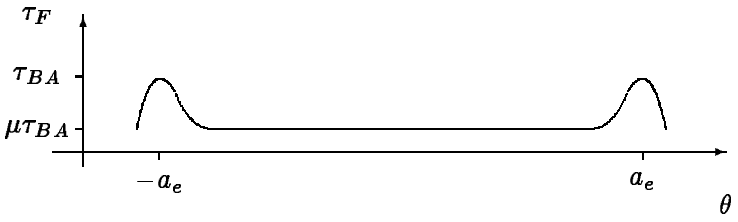

Figure 5.29 Assumption on friction force form during slip in a limit cycle.

The proportional part is $u_p = -k_p\theta$ in the slip phase. The transition from stick to stick is fast whereas the integral part can be regarded as constant under this movement (another approximation, which reduces the order of the equation by one). From (5.10) we have $u_i = \tau_s - u_p$ at break-away which gives $u_i = \tau_s - k_p a_e$ during slip. The equation of motion now is

$$J\ddot{\theta} + k_p\theta = \tau_s - \tau_k - k_p a_e.$$

Solving this differential equation with $\theta(0) = a_e$, $\dot{\theta}(0) = 0$ gives a harmonic oscillation of θ with amplitude a_e. The system comes to rest at $t = t_1$, with

$$\theta(t_1) = -\frac{\tau_s - \tau_k}{k_p} + a_e,$$

and remains in rest due to stiction. We also requires the limit cycle to be symmetric, that is $\theta(t_1) = -a_e$ and $\dot{\theta}(t_1) = 0$. This gives

$$a_e = \frac{\tau_s - \tau_k}{2k_p}. \tag{5.12}$$

Equation (5.12) can be inserted into (5.11) giving

$$T = \frac{4k_p}{k_i}\frac{\tau_s + \tau_k}{\tau_s - \tau_k}. \tag{5.13}$$

In (5.13) we see that $T \to \infty$ as $\tau_s \to \tau_k$. This is intuitive, since we expect the limit cycle to disappear when the stiction force force is equal to the kinetic friction. Also in (5.12) $a_e \to 0$ as $\tau_s \to \tau_k$.

Equations (5.12) and (5.13) together give expressions for determining the approximate error amplitude and frequency of any limit cycle in the system of figure 5.1, given the stiction torque τ_s and the kinetic torque τ_k.

PROPERTY 5.1
Limit cycles appearing in a system composed of a double integrator under influence of symmetric friction defined by stiction torque τ_s and kinetic friction τ_k and a PID regulator will have error amplitude a_e and period T approximately given by (5.12), (5.13). □

Remark 1. Having neglected derivative action and viscous friction and the small change of the integral action during slip we can expect to over-estimate the slip length and thus the the error amplitude, and thus under-estimate the period.

(5.12) and (5.13) can be written

$$\begin{bmatrix} 1 & -1 \\ 4k_p - Tk_i & 4k_p + Tk_i \end{bmatrix} \begin{bmatrix} \tau_s \\ \tau_k \end{bmatrix} = \begin{bmatrix} 2k_p a_e \\ 0 \end{bmatrix}. \tag{5.14}$$

The determinant of the equation matrix is non-zero for all choices of k_i, $k_p > 0$, T, a_e, why there is a one to one mapping between friction model paramters and limit cycle characteristics for a given PID regulator. The friction model parameters are given as the solution of (5.14):

$$\begin{bmatrix} \tau_s \\ \tau_k \end{bmatrix} = \begin{bmatrix} \left(\frac{k_i T}{4} + k_p\right) a_e \\ \left(\frac{k_i T}{4} - k_p\right) a_e \end{bmatrix}. \tag{5.15}$$

(5.15) can thus be used to estimate the friction model parameters from limit cycle amplitude and period.

Asymmetric static friction + PID control

In this section we extend the analysis of the previous section by introducing asymmetry in the friction model. We assume periodicity but not symmetry on the limit cycle. We will refer to the stiction torques as τ_s^+, τ_s^-, with upper index refering to sgn(e), and to the kinetic torques as τ_k^-, τ_k^+, with upper index being sgn(v). We characterize the limit cycle by the error amplitudes in respective direction as a_e^+, a_e^- with upper index denoting sgn(e), and by the period $T = T^+ + T^-$, with T^+ being the stick time in a_e^+ and T^- the stick time in a_e^-. See figure 5.30.

We search expressions for a_e^+, a_e^-, T^+, T^- using the PID parameters and the friction model parameters.

The symmetry condition give us $u_i(0) = u_i(T)$. This can be written as

$$\int_{T^+} a_e^+ dt - \int_{T^-} a_e^- dt = 0$$

giving

$$a_e^+ T^+ = a_e^- T^-. \tag{5.16}$$

Further on we have $u_p(0) + u_i(0) = -\tau_s^-$ for transition from stick to slip at $e = -a_e^-$, and $u_p(T^+) + u_i(T^+) = \tau_s^+$ for transition from stick to slip at $e = a_e^+$. This gives

$$\begin{cases} u_i(0) &= -\tau_s^- + k_p a_e^- \\ u_i(T^+) &= \tau_s^+ + k_p a_e^+ \end{cases} \tag{5.17}$$

From inspection of figure 5.30 we see that

$$\begin{cases} k_p\left(a_e^- + a_e^+\right) + k_i \int_{T^-} a_e^- &= \tau_s^+ + \tau_s^- \\ k_p\left(a_e^- + a_e^+\right) + k_i \int_{T^+} a_e^+ &= \tau_s^+ + \tau_s^- \end{cases}$$

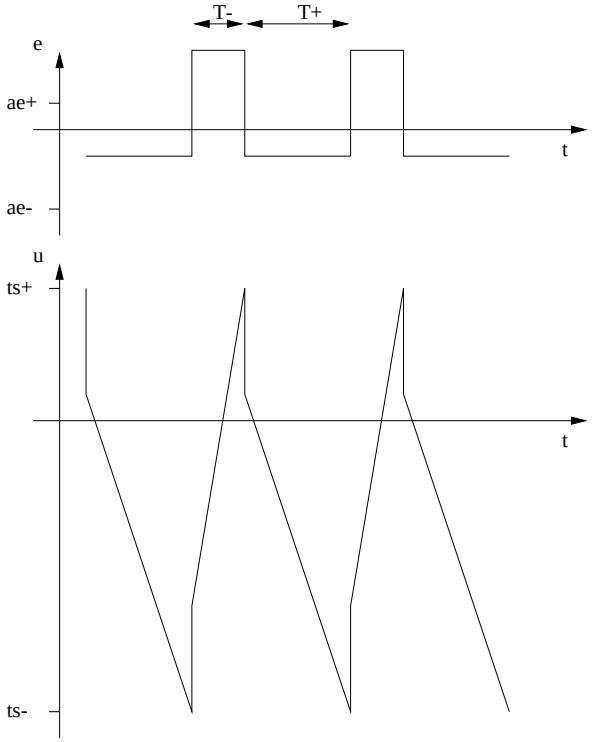

Figure 5.30 Signal forms in an asymmetric friction induced limit cycle.

giving

$$\begin{cases} T^- &= \frac{1}{k_i a_e^-}\left(\tau_s^+ + \tau_s^- - k_p\left(a_e^- + a_e^+\right)\right) \\ T^+ &= \frac{1}{k_i a_e^+}\left(\tau_s^+ + \tau_s^- - k_p\left(a_e^- + a_e^+\right)\right). \end{cases} \tag{5.18}$$

The equation of motion $J\ddot{\theta} = u - \tau$ during slip from $e = -a_e^-$ to $e = a_e^+$ will give us an expression for the slip amplitude. Assume as before that the friction force during slip is equal to the kinetic friction force, i.e. $\tau = -\tau_k^-$. Derivative action in the controller is neglected. Integral action is considered constant during slip, $u_i(t) = u_i(0)$ with $u_i(0)$ given by (5.17). The proportional action is $u_p = -k_p\theta$. Thus we have the following equation of motion

$$J\ddot{\theta} + k_p\theta = \tau_s^- + k_p a_e^- + \tau_k^- \tag{5.19}$$

with initial conditions $\theta(0) = a_e^-, \dot{\theta}(0) = 0$ and final conditions $\theta(t') = -a_e^+, \dot{\theta}(t') = 0$. Solving this gives

$$a_e^- + a_e^+ = \frac{\tau_s^- - \tau_k^-}{k_p}. \tag{5.20}$$

For slip in the other direction we get in the same way

$$a_e^- + a_e^+ = \frac{\tau_s^+ - \tau_k^+}{k_p}. \tag{5.21}$$

Equations (5.20) and (5.21) draw us to the sad conclusion that

$$\tau_s^- - \tau_k^- = \tau_s^+ - \tau_k^+. \tag{5.22}$$

I.e. the difference between stiction and kinetic friction has to be equal in both direction. The condition (5.22) is a necessary condition for a limit cycle of the assumed form to exist under the given premisses. This result is a little bit difficult to interpret. In applications and simulations asymmetric limit cycles of the assumed form has shown to appear without (5.22) to hold. Suggestions on what is going on here are welcome.

Introduce τ_d as

$$\tau_d \equiv \tau_s^- - \tau_k^- = \tau_s^+ - \tau_k^+.$$

Then we have

$$T^+ = T^- = \frac{2k_p}{k_i}\frac{\tau_k^+ + \tau_k^- + \tau_d}{\tau_d}, \tag{5.23}$$

and

$$a_e^+ = a_e^- = \frac{\tau_d}{2k_p}. \tag{5.24}$$

We get symmetric limit cycles as in the symmetric friction case. For $\tau_k^- = \tau_k^+$ (5.24) and (5.23) reduces to (5.12) and (5.13).

Set $T \equiv 2T^+ = 2T^-$, $a_e \equiv a_e^+ = a_e^-$. We then have

PROPERTY 5.2
Limit cycles appearing in a system composed of a double integrator under influence of asymmetric friction defined by kinetic friction τ_k+, τ_k^-, stiction $\tau_k^+ + \tau_d$, $\tau_k^- + \tau_d$ in positive and negative directions respectively, and a PID regulator, will result in a symmetric limit cycle with the error amplitude a_e and the period T approximately given by (5.23), (5.24). □

From (5.24) and (5.23) we then derive

$$\tau_d = 2k_p a_e, \tag{5.25}$$

$$\tau_k^+ + \tau_k^- = (k_i T - 2k_p)a_e. \tag{5.26}$$

In figure 5.9 a limit cycle for the Lugre model is plotted. The model parameters are those of table 5.6, and give $\tau_s^- = 0.30$ Nm, $\tau_k^- = 0.14$ Nm, $\tau_s^+ = 0.46$ Nm and $\tau_k^+ = 0.30$ Nm. Note that the difference $\tau_d = \tau_s - \tau_k = 0.16$ is the same in both directions for these parameters. The PID-parameters are given by table 5.2. Note that several things violate the approximations made in the analysis in this section. The friction model is not the classical model, but a dynamic model. We have viscous friction, and we have a derivative part in the regulator.

The characteristics from the limit cycle measured in the figure are $a_e^- = 0.48$ rad, $a_e^+ = 0.45$ rad, $T^- = 2.2$ s and $T^+ = 2.3$ s. The characteristics predicted by property 5.2 are $a_e^- = 0.44$ rad, $a_e^+ = 0.44rad$, $T^- = 2.5$ s and $T^+ = 2.5$ s The estimates are rather good.

Now we look at how a truly asymmetric friction model behaves. We use the model parameters from table 5.12, and the same PID-regulator as above. We then have $\tau_s^- = 0.35$ Nm, $\tau_k^- = 0.15$ Nm, $\tau_s^+ = 0.45$ Nm and $\tau_k^+ = 0.40$ Nm. The result is shown in figure 5.31. Characteristics of the limit cycle measured in the figure are $a_e^- = 0.70$ rad, $a_e^+ = 0.33$ rad, $T^- = 1.45$ s and $T^+ = 3.44$ s. In this case we get a limit cycle of the form assumed in the analysis above, even though the analysis did not result in expressions for these characteristics.

We can conclude that the properties 5.1, 5.2 could be used to find properties of limit cycles, and that the inverse relations could be used to find estimates of friction model parameters.

	σ_0 [Nm/rad]	σ_1 [Nms/rad]	v_0 [rad/s]	α_0 [Nm]	α_1 [Nm]	α_2 [Nms/rad]
$-$	280	1	0.1	0.15	0.20	0.017
$+$	280	1	0.1	0.30	0.15	0.017

Table 5.12 Asymmetric Lugre model parameters.

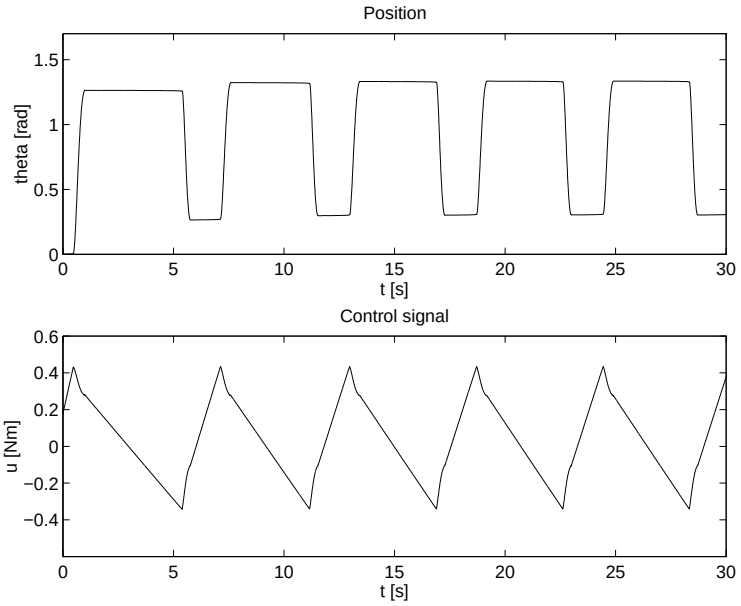

Figure 5.31 Limit cycle from simulation with Lugre friction model. Reference step 1 rad. Upper: Position versus time. Lower: Control signal versus time.

Generalized approach

Now we will generalize the above procedure by removing the approximations. A state space formulation will be used to analyze the same system. The plant is described by

$$\begin{cases} \dot{\boldsymbol{x}} &= A\boldsymbol{x} + B(\boldsymbol{u} - \boldsymbol{\tau}) \\ \boldsymbol{y} &= C\boldsymbol{x} \end{cases} \tag{5.27}$$

with

$$A = \begin{bmatrix} 0 & 1 \\ 0 & -\frac{\alpha}{J} \end{bmatrix}, B = \begin{bmatrix} 0 \\ \frac{1}{J} \end{bmatrix}, C = \begin{bmatrix} 1 & 0 \end{bmatrix}. \tag{5.28}$$

and the state vector $\boldsymbol{x} = \begin{bmatrix} \theta & \dot{\theta} \end{bmatrix}^T$. The PID controller can be implemented by state feedback $u = -L\hat{\boldsymbol{x}}$, introducing an extra state, with $L = \begin{bmatrix} -1 & \boldsymbol{k_p} & \boldsymbol{k_d} \end{bmatrix}$. We have chosen as the extra state the integral action of the controller, thus the new vector is $\hat{\boldsymbol{x}} = \begin{bmatrix} \boldsymbol{u_i} & \theta & \dot{\theta} \end{bmatrix}^T$. We drop the hat and refer in the following only to the third order closed loop system. The new system is (5.27) with

$$A = \begin{bmatrix} 0 & -\boldsymbol{k_i} & 0 \\ 0 & 0 & 1 \\ \frac{1}{J} & -\frac{\boldsymbol{k_p}}{J} & -\frac{\alpha+\boldsymbol{k_d}}{J} \end{bmatrix}, B = \begin{bmatrix} 0 \\ 0 \\ \frac{1}{J} \end{bmatrix}, C = \begin{bmatrix} 0 & 1 & 0 \end{bmatrix}. \tag{5.29}$$

During a slip motion the system trajectory is given by

$$x(t) = e^{At}x_0 + \int_0^t e^{A(t-s)}B\tau ds \tag{5.30}$$

with $x(0) = [\ \tau_s + k_p\theta(0) \quad \theta(0) \quad 0\ ]$, since $u_i(0) + u_p(0) = \tau_s$.

Denote by t_k the time at which a slip start, and with t'_k the time when the slip stops. Thus we have $x(t_k) = [\ \tau_s + k_p\theta(t_k) \quad \theta(t_k) \quad 0\ ]$. $\theta(t'_k)$ thus is found by solving

$$x(t'_k) = e^{At'_k}x(t_k) + \int_0^{t'_k} e^{A(t'_k-s)}ds\,B\tau_k \tag{5.31}$$

for the first solution such that $x(t'_k) = [\ \cdot \quad \cdot \quad 0\ ]$. Introducing

$$\Phi_k = e^{At'_k}, \Gamma_k = \int_0^{t'_k} e^{A(t'_k-s)}ds\,B \tag{5.32}$$

we have

$$x(t'_k) = \Phi_k x(t_k) + \Gamma_k\tau_k. \tag{5.33}$$

Without any motion during stick we have $\theta(t_{k+1}) = \theta(t'_k)$. During stick the integral term increases, but position remains the same, and velocity is zero. We have $x(t'_k) = [\ \cdot \quad \cdot \quad 0\ ]$ and know that $x(t_{k+1}) = [\ \tau_s + k_p\theta(t_{k+1}) \quad \theta(t_{k+1}) \quad 0\ ]$. This is acheived with the map

$$x(t_{k+1}) = \hat{\Phi}_k x(t'_k) + \hat{\Gamma}_k\tau_s \tag{5.34}$$

with

$$\hat{\Phi}_k = \begin{bmatrix} 0 & k_p & 0 \\ 0 & 1 & 0 \\ 0 & 0 & 0 \end{bmatrix}, \hat{\Gamma}_k = \begin{bmatrix} 1 \\ 0 \\ 0 \end{bmatrix}. \tag{5.35}$$

The complete map $x(t_k) \to x(t_{k+1})$ thus is given by

$$x(t_{k+1}) = \hat{\Phi}_k\left(\Phi_k x(t_k) + \Gamma_k\tau_k\right) + \hat{\Gamma}_k\tau_s \iff$$

$$x(t_{k+1}) = \hat{\Phi}_k\Phi_k x(t_k) + \Phi_k\Gamma_k\tau_s + \hat{\Gamma_k}. \tag{5.36}$$

The limit cycle can now be completely described by (5.31), (5.32), (5.35) and (5.36). No approximations have been made. This is a Poincaré map for which the asymptotic behaviour in the general case can show very complex beaviour. Simulation is a good tool to investigate such a map.

This map is general also in the sense that it can be used for investigating friction induced limit cycles also in other linear systems than that of a damped double integrator and a PID controller which is treated here.

This generalized approach gives dynamic maps which do not give immidiate expressions for error amplitudes or periods. By analyzing the equations in detail for solvability conditions etc. maybe this can be found, at least for some special cases. Otherwise the map may be used iteratively to find asymptotic behaviour of a system. As the map is based on integration of the system this becomes more or less equivalent to a pure numerical simulation of the system though. Without further analysis this approach does not seem very useful in other words. The idea is more thoroughly worked through in [22].

Real friction and existance of limit cycles

We here pose the question when a limit cycle can exist? For a certain system with friction there exists a pre-sliding distance ϵ, which defines within which displacement range the system can be expected to exhibit a spring like behaviour. I.e. ϵ defines how much the system can move when in stick, without going into slip. For a given initial error e such that $e < \epsilon$ no limit cycle will occur, since the error can be eliminated without taking the system to slip. Other initial errors $e > \epsilon$ might very well gives limit cycles, but not necessarily. Assume a friction without pre-sliding displacement. In this case a limit cycle will be present for the reason given in the paragraph above. Assume also that we can predict the error amplitude e_a of this limit cycle. Now introduce the pre-sliding displacement ϵ. If $e_a < \epsilon$ no limit cycle will remain asymptotically, since this error is asymptotically eliminated without going into slip, and the slip being the reason for the limit cycle.

In short we have

PROPERTY 5.3—TRANSIENT EXISTENCE
For a limit cycle to occur the initial error $e(0)$ must be larger than the pre-sliding displacement ϵ

$$e(0) > \epsilon. \tag{5.37}$$

□

and

PROPERTY 5.4—ASYMPTOTICAL EXISTENCE
For a symmetric limit cycle to exist asymptotically the following condition must be fulfilled:

$$a_e > \epsilon \tag{5.38}$$

where the error amplitude a_e is the error amplitude of the corresponding limit cycle in a system without pre-sliding displacement, and ϵ is the pre-sliding displacement. □

Remark 1. The approximate expression (5.12) may be used to find e_a in property 5.4.

Remark 2. It is not only pre-sliding that have the property of eliminating limit cycles. If there is any possibility for the system to move without leaving stiction, the conditions defined by properties 5.4 and 5.3 must be fullfilled for the limit cycle to appear.

To verify this we look at figure 5.32 where experimental responses to position reference steps for the dry friction case in chapter 4 is plotted. Two different PID regulators are used. Their parameters are given in table 5.13. According to the earlier identification we have $\tau_s = 0.70$ Nm, $\tau_k = 0.48$ Nm, and ϵ =25 mrad. Property 5.1 then suggests limit cycles with $a = 0.46$ rad, $T = 8.2$ s and $a = 0.12$ rad, $T = 4.1$ s for PID 1 and PID 2 respectively. Note that in this system we have a pre-sliding displacement of about 25 mrad, but also a backlash of about 70 mrad. This means that limit cycles with a predicted amplitude less than about 100 mrad asymptotically are "absorbed". Limit cycles with larger amplitudes may also very well be aborbed in the same way if the error in stick suddenly happen to be less than 100 mrad. We can see that variations of about 100 mrad in limit cycle amplitude can be seen in the limit cycles of this system. Thus the limit cycles of PID 1 have a big chance to survive asymptotically due to their large amplitude, if they get a chance to

start. This we see in the upper plot. According to property 5.3 no limit cycle will exist if the initial step is small enough. This is illustrated by the middle plot, where the system with PID 1 is given an initial step of 25 mrad. No limit cycle occurs, but the system moves within pre-sliding displacement to adjust the position error. (The backlash was in contact before the step was put on.) In the lower plot the system with PID 2 is given a input step of 1 rad, resulting in two slips, and then approaching zero error, according to property 5.4.

k_p' [Nm/rad]	k_i' [Nm/rads]	k_d' [Nms/rad]
95	250	17
380	2000	34

Table 5.13 PID parameters used in experimental limit cycling system. Upper: PID 1, giving limit cycles. Lower: PID 2, no limit cycles.

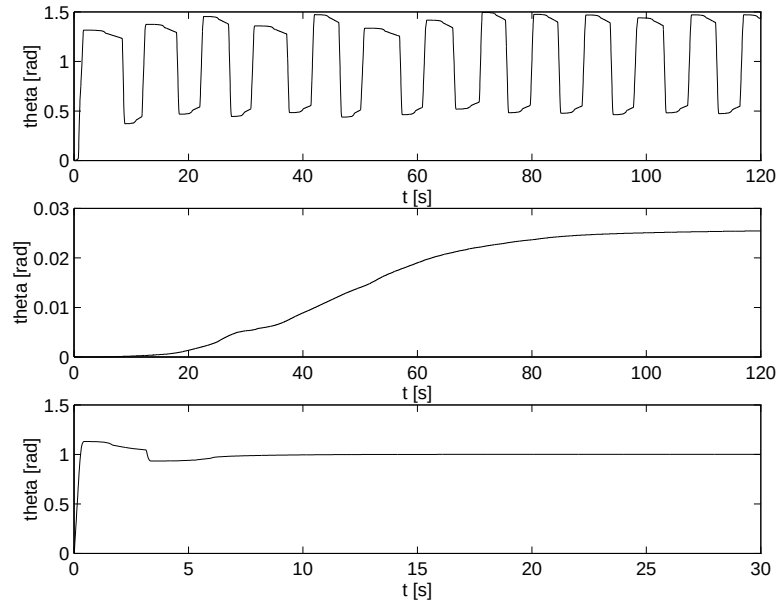

Figure 5.32 Responses to reference steps r from experiments with dry friction and position PID-control. Illustration of properties 5.4, 5.3. Upper: PID 1, designed for $\omega_c = 3.5$ rad/s, $\zeta = 0.58$, $r = 1$ rad. Middle: PID 1, $r = 25$ mrad. Lower: PID 2, designed for $\omega_c = 8.0$ rad/s, $\zeta = 0.63$, $r = 1$ rad.

Now we show that the Lugre model reproduces this behaviour, while a classical model does not. The Lugre model is used with the parameters of table 5.10. As for the experimental case two different PID regulators are used. Parameters are given in table 5.14. In figure 5.33 we see the results. In the upper plot PID 1 and a large reference step of 1 rad is used, and a limit cycle is induced. Limit cycle characteristics according to property 5.1 are $T = 5$ s and $a_e = 0.44$ rad. In the middle plot the same system with a small reference step of 1 mrad does not give a limit cycle. According to property 3.1 the pre-sliding displacement of the system with the given parameters is about 1.4 mrad. The small step together with a quite small integral action makes it take quite some time for the system to go to zero error. The phenomenon is still

illustrated anyway. In the lower plot PID 2 does not give a limit cycle when the reference step 1 rad is applied. Property 5.1 predicts $T = 1.5$ s and $a_e = 0.012$ rad. No limit cycle occurs. With a static classical friction model with stiction

k_p' [Nm/rad]	k_i' [Nm/rads]	k_d' [Nms/rad]
72	216	5.2
2700	27000	83

Table 5.14 PID parameters used in simulated limit cycling system with Lugre friction. Upper: PID 1, designed for $\omega_c = 6$ rad/s, $\zeta = 0.5$, giving limit cycles. Lower: PID 2, designed for $\omega_c = 30$ rad/s, $\zeta = 1$ no limit cycles.

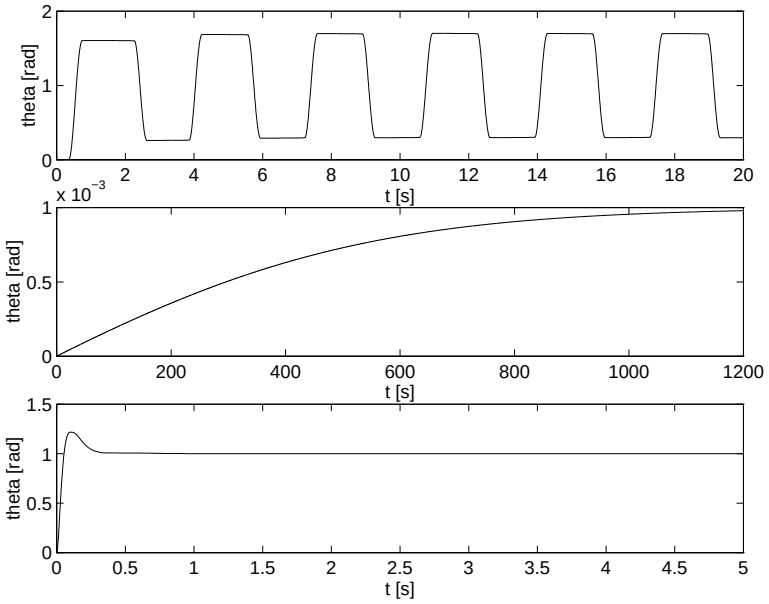

Figure 5.33 Responses to reference steps r from simulations with Lugre friction and position PID-control. Illustration of properties 5.4, 5.3. Upper: PID 1, $r = 1$ rad. Middle: PID 1, $r = 1$ mrad. Lower: PID 2, $r = 1$ rad.

and kinetic friction with $\tau_s = 0.38$ Nm and $\tau_k = 0.22$ Nm the responses are as in figure 5.34. The regulators are the same as in the Lugre case. In the upper plot we get the limit cycle as before. In the middle plot we do also get a limit cycle now. The position of the system is exactly zero while the regulator integrates the error. When the control signal reaches the break-away torque the system goes into slip and enters a limit cycle. In the lower plot we see that no limit cycle is present. The reason for this can not be phenomenon described by property 5.4, since there is no possibility for the system to move without going into slip. See [22] for a deeper analysis of the case with limit cycles in linear systems with classical friction.

In [15] similar results are shown without explicit explanation. Simulations of classical models without pre-sliding displacements are there shown to give limit cycles in a case with small reference steps, while dynamic models with pre-sliding displacement do not.

The conclusion of the above is that one important property from a limit cycle point of view that is introduced by dynamic friction models is the pre-

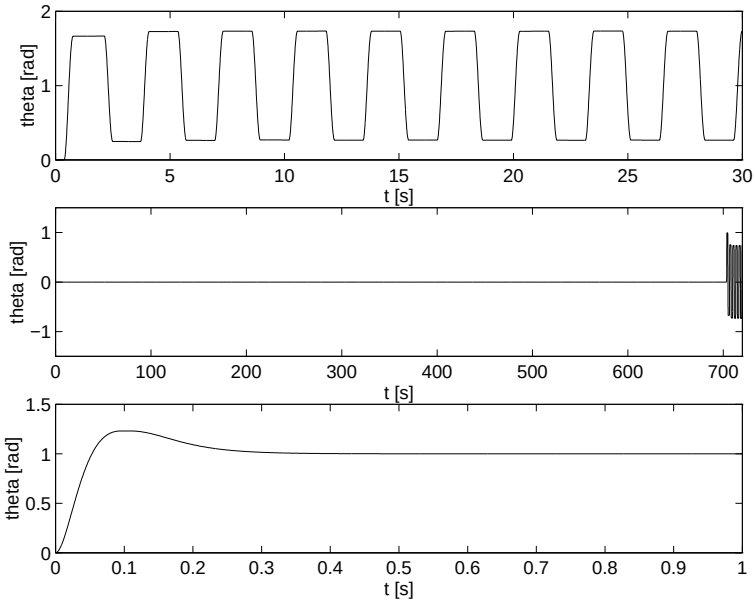

Figure 5.34 Responses to reference steps r from simulations with classical static friction and position PID-control. Illustration of properties 5.4, 5.3. Upper: PID 1, $r = 1$ rad. Middle: PID 1, $r = 1$ mrad. Lower: PID 2, $r = 1$ rad.

sliding displacement. It gives conditions on existence of limit cycles, both transientely and asymptotically, as formulated by properties 5.4 and 5.3.

6. Conclusions

Two dynamic friction models have been investigated in this report, the model of Bliman & Sorine and the Lugre model.

In chapter 2 and chapter 3 the models are presented. Both models are extensions of the Dahl model to include more friction phenomena. The Dahl model is a first order linear space invariant system where the friction force depends only upon the displacement relative the last sign change of velocity. In time domain the model is non-linear time invariant.

The Bliman & Sorine model is roughly speaken two Dahl models in parallell. The model thus is a non-linear second order model in time domain. Stiction is modeled by letting total friction be the sum of two Dahl models with different signs and different space constants. This means the Bliman & Sorine model inherits some properties of the Dahl model. As for the Dahl model the model response only depends upon the absolute relative displacement, and does not include any rate dependency. Thus it can not reproduce any rate dependent beahaviour such as rate dependent break-away force. The model response is transient. After a finite displacement the model states have reached stationary values and the response is constant until a sign change of velocity occurs. This makes it impossible to reproduce for example frictional lag which is a phenomenon in uni-directional motion.

The Bliman & Sorine model is parametrized by five parameters including viscous friction. The identification procedure suggested by the authors of the model is simple. Four of the parameters are defined by two points in a friction force versus time plot for saturated hysteretic motion. These points define stiction force, pre-sliding displacement and kinetic friction. It is not clear how to introduce optimization in this identification. After having identified the points there is a map from the points to the model parameters. The map does not have solutions for all choices of points though. This gives a limitation in which physical systems the model can model. This also can give problems in an automatized identification scheme based on these points. It is clear that the model response only exhibits the given stiction force and pre-sliding displacement under a saturated hysteretic motion. Under other motions the responses are different.

Some interesting properties of the Bliman & Sorine model connected to a simple mass system have been found. By linearizing the equations it is discovered that the damping of this system critically depends on viscous friction. This means that the system can show oscillatory behaviour near zero velocity. Damping is increased by increasing viscous friction, but this means changing a high velocity property of the system that not necessarily can be changed arbitrarily. The oscillations also makes it impossible for the system to follow the saturated hysteretic motion defining the stiction force and the pre-sliding displacement. This means that connecting the friction model to a mass system one does not get the model response defined by the identified points. The oscillations bring down simulation efficiency. The Bliman & Sorine model needs significantly more computation power to simulate a certain system than the Lugre model.

The Lugre model is obtained by letting the space constant in a Dahl model vary in a velocity dependent way. Also a damping term is added. Stiction is modeled by the velocity dependent space constant. The model thus is a non-

linear first order model in time. It is not linear space invariant as the Dahl model and the Bliman & Sorine model. This slightly complicates the mathematical analysis. The velocity dependency and the damping term makes it possible for the model to reproduce rate dependent and non-transient behaviour such as rate dependent break-away force and frictional lag.

The Lugre model is parametrized by six parameters including viscous friction. Identification of these is non-trivial, but can be done by means of a multiple step scheme giving in some sense optimal parameter values.

Linearizing of the Lugre model connected to a mass system gives equations where the damping can be tuned almost separately from other model properties. This thanks to the damping term included in the model. This means that the problems with damping encountered in the Bliman & Sorine model are not found for the Lugre model.

The damping term gives some mathematical difficulties though. The presented model is not dissipative, but can under certain conditions produce energy. The non-dissipativeness of the model does not imply problems with stability, but still is an annaoying property of a friction model. There exists several modifications of the model which makes the model dissipative. These are based on the idea of making the damping term dependent on velocity. A drawback with this is that this may add another parameter to the model. It is not entirely clear if a modification is necessary in practice though.

For both models it is straightforward to introduce asymmetries in the friction.

In chapter 4 experiments were carried out. Two situations were investigated, mixed dry and wet friction and wet friction. In both cases parameter identification for both models were carried out. We found that the restrictions of the map used in the Bliman & Sorine model identifiaction is of practical significance. In the dry case no solution existed for the identified points. There were no great differences between the dry case and the wet case otherwise. The friction force peak at break-away was sharper in the dry case. No additional viscous friction was introduced by the dry friction. Stiction force and kinetic friction increased with additional dry friction. Nothing unexpected. There were some difficulties to separate friction phenomena from unmodeled dynamics in the experimental setup.

When comparing simulated model responses to those of a real system with friction it is clear that both models give good accordance in terms of stiction and pre-sliding displacement. The Lugre model exhibits rate dependent break-away torque found experimentally, while the Bliman & Sorine model does not. Also the Lugre model shows an increase in friction force found experimentally at low velocities, that is not captured by the Bliman & Sorine model. Experimentally small displacement motion have other qualitative properties than what is shown by both models. If these discrepancies are due to unmodeled dynamics or bad friction model properties can be discussed.

In chapter 5 friction induced limit cycles are investigated. Limit cycles in PID position control from the experiments are compared to simulated limit cycles using a classical friction model, the Bliman & Sorine model and the Lugre model. It is found that the properties of the limit cycles do to a great extend depend only on stiction force and kinetic and viscous friction. Since all three models includes these phenomena they all give similar limit cycling. Looking closer at the signal forms in the limit cycles it is seen that the pre-sliding displacement makes the dynamic models better reproduce the experiments. The oscillations of the Bliman & Sorine model makes it difficult to accurately

model asymmetric limit cycles.

A single input describing function analysis of symmetric friction is also done. Describing functions for the Bliman & Sorine model and the Lugre model are computed numerically. From the describing functions of the friction models only it is not possible to predict the limit cycles observed in simulations. In this analysis velocity becomes the non-linearity input. This signal does not agree with the presumptions of the analysis. When more system dynamics are included in the non-linear part of the analysis the Bliman & Sorine and the Lugre model describing functions can correctly predict limit cycles. In this case the control signal is the non-linearity input, and this signal better fulfills the presumptions. The classical model fails under these circumstances though.

An heuristic approach to limit cycle prediction was then taken. Simple reasoning lead to simple static relations giving limit cycle error amplitude and period as a function of stiction and kinetic friction, both for symmetric and asymmetric friction. The relations were shown to fairly good predict the amplitude and the period of the limit cycle, taking into account the large approximations done. The inverse formulas can be used to quickly acheive estimates of friction parameters by looking at a limit cycle. An interesting difference between the symmetric and the asymmetric case is that there is a one to one relation between limit cycles and friction parameters in the symmetric case, but a one to many relation in the asymmetric case. Different friction parameters thus can give the same limit cycles for asymmetric friction.

Removing the approximations and generalizing the class of linear systems in the above analysis results in dynamic maps describing the limit cycles. These are more difficult to interpret, and nothing more than a presentation of the idea is done.

Maybe the most important property of dynamic friction models that differ them from classical static ones is the pre-sliding displacement. Finally we discussed what impact this property has on limit cycles. Two properties were presented relating pre-sliding displacement to existence of limit cycles transiently and asymptotically.

In this report two friction models have been investigated and discussed. Certain properties have been highlighted, but several properties remain to investigate. To the question of which class of systems best are suited for which model no clear answers are given in this report. Of course if there are significant rate dependent friction phenomena in the real system the best model would be the Lugre model since this is the only one handling this kind of phenomena. Also in terms of simulation efficiency the Lugre model seems to be prefered. A model based friction compensation requires some kind of observer. Maybe the Lugre model is then prefered because of the lower order, there is only one state to observe. No references to model based friction compensation using the Bliman & Sorine model have been found. The best way to compare two friction models would be to design friction compensation based on the different models and apply them on a real system. This would be the ultimate test to determine which model is best suited to a certain system.

A. Passivity definitions

Passivity of a system is a mathematical property which can be used for stability analysis of coupled systems. But passivity also has an important physical interpretation in the case when the product of input and output of a system has the dimension of effect, as it then roughly means that the system consumes energy, or at least does not produce energy by itself. Therefore we often want a model that represents a physical process without unmodeled energy supply to be passive. This does not imply though that a non-passive model necessarily is useless for modeling a physical process. Below some definitions related to passivity are given together with som comments and interpretation. For a complete and rigorous treatment of the subject see [25, 9].

Given a nonlinear mapping $\Phi : U \mapsto Y$ with state space X, we introduce th *supply rate* $w = w(u(t), y(t))$, $u \in U, y \in Y$ with $\int_{t_0}^{t_1} |w(t)|dt < \infty$.

DEFINITION A.1—DISSIPATIVE SYSTEM
A nonlinear dynamical system is said to be *dissipative* with respect to the supply rate w if there exist a non-negative function $V : X \mapsto \mathbb{R}^+$ such that for all $t_0, t_1 \in \mathbb{R}, x_0 \in X$,

$$\int_{t_0}^{t_1} w(t)dt \geq V(x_1) - V(x_0) \tag{A.1}$$

The function $V(x)$ is then called a *storage function* for the system. □

By restricting the supply rate to a certain function of input and output we get the following definition:

DEFINITION A.2—PASSIVE SYSTEM
A system is said to be *passive* if it is dissipative with supply rate $w =< u, y >$, and the storage function V satisfies $V(0) = 0$. □

In other words, a system is passive if there exists a non-negative function $V : X \mapsto \mathbb{R}$, wich satisfies $V(0) = 0$ such that

$$\int_0^t y^T(\tau)u(\tau)d\tau \geq V(x) - V(x_0) \tag{A.2}$$

Note that setting $u \equiv 0$ in the above shows that V is decreasing in any unforced trajectory. It follows then that passive systems with positive definite storage functions are Lyapunov stable.

Some particularizations of the passivity definition can be made:

DEFINITION A.3—LOSSLESS PASSIVE SYSTEM
When equality always holds in the passivity definition the system is said to be *lossless passive*

$$\int_0^t y^T(\tau)u(\tau)d\tau = V(x) - V(x_0) \tag{A.3}$$

□

DEFINITION A.4—STRICTLY PASSIVE SYSTEM
When inequality always holds in the passivity definition the system is said to be *strictly passive*

$$\int_0^t y^T(\tau)u(\tau)d\tau = V(x) - V(x_0) + \int_0^t S(x(\tau))d\tau \tag{A.4}$$

□

Note that the storage function V for a system is not uniquely defined from the definitions. But if we consider systems where the supply rate $w =< u, y >$ has the dimension effect, and where the systems have physical equivalents there exist a storage functions corresponding to the energy potential functions. Of course dissipativity and passivity might be shown for these systems with other choices of storage functions, but the choice of energy potential functions is very natural in this case.

The physical interpretation of passivity then is the following: A physical system "consumes" energy that is given by the input. The "consumption" can be divided into two parts, one that represents energy that is *stored* in the system, (e.g. for a mass-spring system energy might be stored as kinetic energy for the mass or potential energy in the spring), and one part that represents energy *dissipated* by the system (e.g. if a damper is present in the system). Physically no energy is lost of course. What this means is that the energy given by the input, divides into two parts: one part that increases the energy potential of the system, and is regained in the output, and one part that not affects the energy potential, but is transfered elsewhere.

This is described by the following equality, in which the left hand side represents the total change of energy during the time interval $[t_0, t_1]$, and the right hand side shows the division of this energy into stored energy and dissipated energy.

$$\int_{t_0}^{t_1} w(t)dt = V(t_1) - V(t_0) + \int_{t_0}^{t_1} d(t)dt \tag{A.5}$$

The function $d(t)$ represents the *dissipation rate* of the system. For (A.1) to hold it is clear that $d(t) > 0$, $\forall t$. Note that the change of stored energy $V(t_1) - V(t_0)$ might be positive or negative depending on which trajectory the system has followed.

B. Stability definitions and theorems

For full explanations of definitions and theorems referred to below see [19].

DEFINITION B.1—INPUT-OUTPUT STABILITY
A mapping $H : \mathcal{L}_e^p \mapsto \mathcal{L}_e^p$ is $\mathcal{L}$-stable if there exist finite nonnegative constants γ and β such that

$$\|H(u)_\tau\| \leq \gamma \|u_\tau\| + \beta \tag{B.1}$$

for all $u \in \mathcal{L}_e^p$ and $\tau \in [0, \infty)$ □

With $\mathcal{L}$ beeing $\mathcal{L}_\infty$ the definition of input-output stability becomes the notation of bounded input–bounded output stability

DEFINITION B.2—BOUNDED INPUT–BOUNDED OUTPUT (BIBO) STABILITY
A system is $\mathcal{L}_\infty$-stable if for every bounded input $u(t)$, the output $Hu(t)$ is bounded. □

A useful theorem for determining BIBO-stability is the following (given in a shortened and simlified form).

THEOREM B.1—SMALL GAIN
The feedback connection of two $\mathcal{L}$-stable systems $H_1 : \mathcal{L}_e^p \mapsto \mathcal{L}_e^p$ and $H_2 : \mathcal{L}_e^p \mapsto \mathcal{L}_e^p$ with finite gains γ_1 and γ_2 from (B.1) is $\mathcal{L}$-stable if

$$\gamma_1 \gamma_2 < 1. \tag{B.2}$$

□

DEFINITION B.3—STABILITY
The equilibrium point $\boldsymbol{x} = 0$ of the autonomous system $\dot{\boldsymbol{x}} = \boldsymbol{f}(\boldsymbol{x})$ is *stable* if for each $\epsilon > 0$, there exist a $\delta > 0$ such that

$$\|\boldsymbol{x}(0)\| < \delta \Rightarrow \|\boldsymbol{x}(t)\| < \epsilon, \forall t \geq 0. \tag{B.3}$$

□

DEFINITION B.4—ASYMPTOTIMATHCAL STABILITY
The equilibrium point $\boldsymbol{x} = 0$ of the autonomous system $\dot{\boldsymbol{x}} = \boldsymbol{f}(\boldsymbol{x})$ is *asymptotimathcally stable* if it is stable and δ can be chosen such that

$$\|\boldsymbol{x}(0)\| < \delta \Rightarrow \lim_{t \to \infty} \|\boldsymbol{x}(t)\| = 0 \tag{B.4}$$

□

THEOREM B.2—LYAPUNOV STABILITY
Let $\boldsymbol{x} = 0$ be an equilibrium point of $\dot{\boldsymbol{x}} = \boldsymbol{f}(\boldsymbol{x})$. Let $V : D \mapsto \mathbb{R}$ be a continuosly differentiable function on a neighbourhood D of $\boldsymbol{x} = 0$, such that

$$\begin{aligned} V(0) &= 0 \\ V(\boldsymbol{x}) &> 0, \boldsymbol{x} \in D - \{0\} \\ \dot{V}(\boldsymbol{x}) &\leq 0, \boldsymbol{x} \in D \end{aligned}$$

then $\boldsymbol{x} = 0$ is stable. Moreover, if

$$\dot{V}(\boldsymbol{x}) < 0, \boldsymbol{x} \in D - \{0\} \tag{B.5}$$

then $\boldsymbol{x} = 0$ is asymptotimathcally stable. □

C. Experimental setup

C.1 Description

The experimental setup on which all experiments have been carried out is a DC-servo, see figure C.1. The servo is connected to a gearbox which has significant friction. Moreover it is equipped with a load element for applying additional friction. Control algorithms are implemented in C and are run in a dSPACE real-time computer system based on a digital signal processor and AD/DA converters. This is connected to an analog high gain current controller which controls the DC motor.

DC motor

We have the following general model for the DC motor

$$\begin{aligned} J\frac{d\omega(t)}{dt} &= k_c I(t) - F(t) \\ RI(t) &= U(t) - k_b\omega(t) \end{aligned}$$

with

J	:	total motor an load inertia [kg/m^2]
R	:	losses in the magnetic circuit [Ω]
k_c	:	motor current constant, identified to 0.352 [Nm/A]
k_b	:	EFM constant
$\omega(t)$	:	angular velocity [rad/s]
$F(t)$	:	Load torque (e.g. friction) [Nm]
$U(t)$	:	input voltage [V]
$I(t)$	:	corresponding current [A]

Since the DC motor is current controlled by means of a high gain loop the above model can be simplified to

$$\begin{aligned} J\frac{d\omega(t)}{dt} &= k_c I(t) - F(t) \\ I(t) &= k_{U/I} U(t) \end{aligned}$$

where $k_{U/I} = 3$ A/V is the gain of the voltage/current converter. The assumption is made on $k_{U/I}$ to be linear.

The current signal fed to the DC motor is pulse width modulated with a frequency of 20 kHz.

With $k_{D/A}$,$k_{U/I}$ and k_c known, we can get a total gain from dimensionless control signal to torque $k = 10.59\text{Nm}^{-1}$. Knowing this we can use a control signal of dimension torque in the control algoritm, and then multiply the signal with k^{-1} before putting it on the D/A converter.

Gearbox

The motor is linked to an inertial load by means of a gearbox with ratio $n = 15.5$. The inertial load is a metallic homogenous cylindric mass $m = 12$ kg with a radius $r = 5$ cm, with inertia J_l given by

$$J_l = \frac{1}{2}mr^2.$$

The motor inertia is $J_m = 0.00223$ kg/m^2, and the total inertia on the motor side is then

$$J = J_m + \frac{J_l}{n^2}$$

giving $J = 0.0023$ kg/m^2. Identification experiments have verified this figure.

The weels in the gearbox gives a position dependent variation of the system dynamics clearly visible in the high resolution measurements adopted. These variations are often of higher frequencies than the phenomena examined and will therefore be filtered out when possible.

Position measurements

Position measurements are given as angular position of the motor axis. An optical encoder giving up/down pulses with a resolution of 30000 divisions/turn is connected to an incremental 24-bit encoder board with an internal mechanism increasing the resolution by a factor 4. Thus the angular resolution is $\Delta\Phi = 0.52\,\mu$rad. 24-bit two-complement form means that the output from the encoder board has to be denormed by a factor $\frac{2\pi 2^{23}}{4 \cdot 30000}$ to give true position in radians.

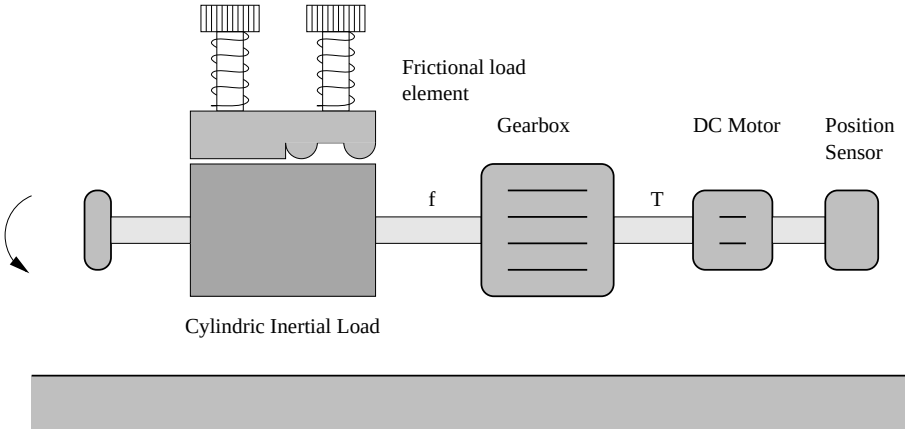

Figure C.1 Schematic diagram of the experimental setup.

dSPACE real-time computer

The sampling time T is 1 ms. No pre-sampling filter is used, which means that an alias frequency of the PWM frequency appears in the sampled signal. See section The control signal with dimension voltage is put on the DA converter, which has a voltage gain $k_{D/A} = 10$ V.

Excentricity

In the measured position a position dependent variation with period $\pi/4$ rad is present. This is assumed to originate from an excentricity of the firt wheel in the gearbox. See discussion in the section on model validation.

Backlash

From experiments it seems as a backlash of magnitude 70 mrad is present in the setup. Presumably in the gearbox.

Friction

The friction in the system is located in different parts. There is friction in the gearbox, in the motor, in bearrings and of course in the frictional load element. The friction present in the gearbox may be classified as wet friction because of the lubrication, whereas the externally applied friction is dry in this sense since the contact surface between the frictional load element and the inertial load is not lubricated.

Thus with no externally applied friction all friction in the system is wet. By applying a relatively large friction with the load element, this friction comes to dominate the total friction, and the system friction will then be dry.

The load element is composed of both area- and line-contacts representing a realistic mix often present in applications. The profile of the load element is shown in figure C.1.

C.2 Digital implementation

The digital implementations of the analog designs of control algorithms carried out in this work are not taken into account in the analysis. The discrete time approximations have been shown to be good within the bandwidth of the (linear) system for the identified parameter values and the sampling time of 1 ms.

C.3 Model approximation

Figure C.2 shows the model of the setup being used throughout this report. The inertia J will be assumed to known as $J = 0.0025$ kg/m^2. The friction in the system is divided into one linear viscous friction $\alpha_2\dot{\theta}$, and one non-linear part $\psi(\cdot)$. Some different choices of $\psi(\cdot)$ are discussed in the report. In reality the viscous friction is not linear, but the coefficient α_2 is decreases with increasing velocities $|\dot{\theta}|$. For small velocities the linear approximation is good though.

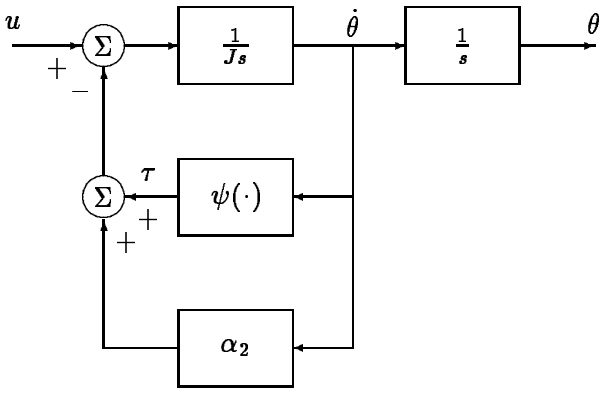

Figure C.2 Block diagram of the continuous part model of the experimental setup.

For more information on the setup see [26].

D. Bibliography

[1] B. Armstrong-Hélouvry, P. Dupont, and C. Canudas de Wit. A survey of models, analysis tools and compensation methods for the control of machines with friction. *Automatica*, 30(7):1083–1138, 1994.

[2] K. Åström and B. Wittenmark. *Adaptive control.* Addison Wesley, 1989.

[3] D. P. Atherton. *Nonlinear Control Engineering.* Van Nostrand Reinhold, student edition, 1992.

[4] C. B. Baril. *Control of Mechanical Systems Affected by Friction and other Nondifferentiable Nonlinearities* Submitted in partial fulfillment of the requirements for the degree of doctor of science, Technion, Israel Institute of Technology, 1993.

[5] P.-A. Bliman and M. Sorine. Friction modelling by hysteresis operators. application to dahl, sticktion and stribeck effects. In *Proc. Conf. Models of Hysteresis*, Trento, Italy, 1991.

[6] P.-A. Bliman and M. Sorine. A system-theoretic approach of systems with hysteresis. application to friction modelling and compensation. In *ECC 93*, 1993.

[7] P.-A. Bliman and M. Sorine. Easy-to-use realistic dry friction models for automatic control. In *Proceedings of 3rd European Control Conference*, Rome, Italy, Sept. 1995.

[8] P.-A. J. Bliman. Mathematical study of the dahl's friction model. *Eur. J. Mech., A/Solids*, 11(6):835–848, 1992.

[9] C. I. Byrnes, A. Isidori, and J. C. Willems. Passivity, feedback equivalence, and the global stabilization of minimum phase nonlinear systems. *IEEE Transactions on Automatic Control*, 36(11):1228–1240, Nov. 1991.

[10] C. Canudas de Wit and P. Lischinsky. Adaptive friction compensation with partially known dynamic friction model. Accepted in the Int. Journal of Adaptive Control and Signal Processing, Special Issue on Adaptive Systems with Nonsmooth Nonlinearities, 1996.

[11] C. Canudas de Wit, H. Olsson, K. Åström, and P. Lischinsky. A new model for control of systems with friction. *IEEE Transactions on Automatic Control*, 40(3), Mar. 1995.

[12] P. E. Dupont and E. P. Dunlap. Friction modeling and control in boundary lubrication. In *Proceedings 1993 American Control Conference*, San Francisco, CA, June 1993.

[13] N. E. Ehrich. An investigation of control strategies for friction compensation. Master's thesis, University of Maryland, 1991.

[14] P. Foreby. *Att skriva rapporter med LaTeX.* Lund Institute of Technology, University of Lund, 5 edition, Dec. 1994.

[15] D. A. Haessig, Jr. and B. Friedland. On the modeling and simulation of friction. *Journal of Dynamic Systems, Measurement and Control*, 113:354–362, Sept. 1991.

[16] A. Harnoy and B. Friedland. Dynamic friction model of lubricated surfaces for precise motion control. In *STLE/ASME Tribology Conference*, New Orleans, Louisiana, Oct. 1993.

[17] D. P. Hess and A. Soom. Friction at a lubricated line contact operating at oscillating sliding velocities. *Journal of Tribology*, 112:147–152, 1990.

[18] R. Johansson. *System modeling & identification*. Prentice Hall Information and System Sciences Series, 1993.

[19] H. K. Khalil. *Nonlinear Systems*. Macmillan Publishing Company, 1992.

[20] H. Kopka and P. W. Daly. *A Guide to LaTeX*. Addison-Wesley Publishing Company, Inc., 1993.

[21] L. Lamport. *LaTeX: A Document Preparation System*. Addison-Wesley Publishing Company, Inc., 1986.

[22] H. Olsson. *Control Systems with Friction*. PhD thesis, Lund Institute of Technology, University of Lund, 1996.

[23] E. Pärt-Enander, B. Melin, P. Isaksson, and A. Sjöberg. *Användarhandledning för* Matlab 4.2. Uppsala Universitet, Mar. 1995.

[24] SSPA Maritime Consulting AB, simnon@sspa.se. *Simnon for Windows, Version 2.0*, May 1995.

[25] J. C. Willems. Disspipative dynamical systems. part i: General theory. *Arch. Rational Mech. Anal.*, 45:321–351, 1972.

[26] J. Wurster. Identification and adaptive control of systems with dynamic friction. Master's thesis, Laboratoire d'Automatique de Grenoble (CNRS-INPG-UJF), 1995.